FLOW THROUGH, 2D/3D NANOPLATELET SUPPORTS FOR PACKED BEDS AND COLUMNS.

XUEWEI MENG

A thesis submitted in partial fulfillment of the requirements for the

Master's in Applied Science degree in Chemical Engineering

Department of Chemical and Biological Engineering

Faculty of Engineering

University of Ottawa

Statement of Contributions and Collaborators

I hereby declare that I am the sole author of this thesis. Editorial comments and changes were made by Dr. André Y. Tremblay. All the experiments and data analysis were performed by me under the supervision and guidance of Dr. André Y. Tremblay.

Abstract

High performance catalyst supports and packing materials are playing an increasing role in many reactions and separations. The dispersion in packed bed reactors and separation columns can be reduced by the development of new packing structures having open and connected pore geometries. The application of new materials in High Performance Liquid Chromatography (HPLC) with sub 5 micron particle sizes are growing. These small particles offer better performance and improved bed and column efficiencies. Recently developed, twinned Alumina Nanosheets (TAN) are 2D/3D nanomaterials that offer promising open geometries for use as column packings and catalysts supports. They have a small particle size (4 μm in length, 1 μmin width and 0.1 μm in thickness) and excellent flow-through capabilities. TANs have recently been used to successfully produce high throughput dynamic membranes.

However, their resistance to compaction is unknown and thought to be limited. A technique was developed to reinforce the TAN nanomaterial. Two binder materials were tested as reinforcing agents; SiO_2 and $AlH_6O_{12}P_3$. The binder-reinforced TANs were then packed into columns. Eleven columns having a 4 cm initial packing length were assembled. Tracer injection studies were performed to investigate the flow behavior and dispersion in these columns. SEM images were also taken to characterize the particles before and after compaction. The best results were obtained using a binding solution containing 7.5 (wt%) SiO_2. The binder SiO_2 offered a better resistance to compaction than the $AlH_6O_{12}P_3$. The Peclet (Pe) number for the columns ranged from 22 to 648. When the content of SiO_2 increased from 0 to 7.5 (wt%), the columns showed an increase in the Pe number. When SiO_2 increased from 7.5 to 20 (wt%), the columns showed a

decrease in the Pe number. However, $AlH_6O_{12}P_3$ did not present any relation between the binder content and the Pe number.

The results of this work demonstrate that reinforced TANs, are a new type of material that offers a packing with an open pore structure and improved channel connectivity. The new reinforced material offers considerable potential in many applications such as catalysis and separations over conventional materials. If they are used as packing materials in HPLC columns or packed bed reactors, they can contribute to a higher separation efficiency or an enhanced conversion rate or productivity, bringing more advantages and benefits than ordinary packing materials.

Résume

Les supports de catalyseur et les garnitures jouent un rôle croissant dans de nombreuses réactions et séparations. La dispersion dans les réacteurs à lit garni et les colonnes de séparation peut être réduite par le développement de nouvelles structures de garnissage ayant des géométries de pores ouvertes et connectées. L'application de nouveaux matériaux dans la chromatographie liquide à haute performance (HPLC) avec des tailles de particules inférieures à 5 microns est en développement. Ces petites particules offrent de meilleures performances et améliorent l'efficacité des lits et des colonnes. Les nanoparticules d'alumine (TAN) jumelées récemment développées sont des nanomatériaux 2D / 3D offrant des géométries ouvertes prometteuses pouvant être utilisées comme garnitures de colonne et supports de catalyseurs. Ils ont une petite taille de particule (longueur de 4 µm, largeur de 1 µm et épaisseur de 0,1 µm) et d'excellentes capacités d'écoulement. Des TAN ont récemment été utilisés pour produire avec succès des membranes dynamiques à haut débit.

Cependant, leur résistance à la compaction est inconnue et considérée comme limitée. Une technique a été développée pour renforcer le nanomatériau TAN. Deux matériaux liants ont été testés en tant qu'agents de renforcement; SiO_2 et $AlH_6O_{12}P_3$. Les TAN renforcés de liant ont ensuite été placés dans des colonnes. Onze colonnes ayant une longueur initiale de 4 cm ont été assemblées. Des études d'injection de traceurs ont été effectuées pour étudier le comportement et la dispersion de l'écoulement dans ces colonnes. Des images SEM ont également été prises pour caractériser les particules avant et après compactage. Les meilleurs résultats ont été obtenus en utilisant une solution de liaison contenant 7,5% en poids de SiO_2. Le liant SiO_2 offre une meilleure résistance à la compaction et à un coefficient de dispersion plus faible que le

$AlH_6O_{12}P_3$. Le nombre de Peclet (Pe) pour les colonnes allait de 22 à 648. Lorsque la teneur en SiO_2 augmentait de 0 à 7,5 (% en poids), les colonnes présentaient une augmentation du nombre de Pe. Lorsque SiO_2 augmentait de 7,5 à 20% en poids, les colonnes présentaient une diminution du nombre de Pe. Cependant, $AlH_6O_{12}P_3$ ne présentait aucune relation entre la teneur en liant et la dispersion axiale.

Les résultats de ces travaux démontrent que les TAN renforcés constituent un nouveau type de matériau offrant une garniture avec une structure à pore ouvert et une connectivité améliorée des canaux. Le nouveau matériau renforcé offre un potentiel considérable dans de nombreuses applications tels que la catalyse et la séparation par rapport aux matériaux conventionnels.

Acknowledgements

I would like to express my great gratitude to Dr. Andre Y. Tremblay for his continuous guidance, advice and support throughout my research.

I would also like to thank Franco Ziroldo, Gerald Nina and James Macdermid for technical assistance during the experiments.

I am grateful to Katrina Roebuck, Jiarong Zhou and all my colleagues in the faculty for their support and encouragement.

Table of Contents

Statement of Contributions and Collaborators ..... **ii**

Abstract ..... **iii**

Acknowledgements ..... **vii**

Nomenclature ..... **xiv**

1. Introduction and literature review **1**

1.1 Introduction and objectives **1**

1.2 Packing and supports for reaction and chromatography **3**

1.2.1 Catalyst supports 4

1.2.2 Packed bed reactors and adsorption columns 6

1.2.3 Chromatography columns 8

1.2.4 Effect of particle shape 12

1.3 Alumina and its applications **14**

1.3.1 Interest in morphology control of alumina 15

1.3.2 Application of non-porous alumina 16

1.3.3 Application of porous alumina 17

1.4 Twinned Alumina Nanosheets (TAN) **19**

1.5 Binders for ceramic materials **20**

1.5.1 Applications of binder materials in enhancing strength of ceramics 21

1.5.2 Selection of binders 22

1.5.3 Inorganic binders 23

1.5.4 Silica binder 24

1.6 Characterization of packed beds **26**

2. Experimental **32**

2.1 Materials **32**

2.2 Methods **33**

2.2.1 2D/3D nanosheet (TAN) synthesis 33

2.2.2 Binder solubility analysis 33

2.2.3 Binding of TAN 34

2.2.4 Column packing 35
2.2.5 Measure the pressure drop of the packed columns 35
2.2.6 Tracer injection 38

3. Results – binding agent 41
3.1 Binder solubility in ethanol 41
3.1.1 The binder SiO_2 41
3.1.2 The binder $AlH_6O_{12}P_3$ 42
3.2 Preliminary studies: Binding of TAN without ethanol 46
3.2.1 Use of SiO_2 as a binder 46
3.2.2 Use of $AlH_6O_{12}P_3$ as a binder 49
3.3 Binding with TAN with solutions of ethanol 53
3.3.1 Binding with SiO_2 with solutions of ethanol 53
3.3.2 Binding with $AlH_6O_{12}P_3$ 56
3.4 Flow studies: Packed column pressure drop 58

4. Results – Residence Time Distribution 63
4.1 Correlation of concentration and voltage 63
4.2 Transforming the output curve to an RTD function 64
4.2.1 Columns with SiO_2 binder 64
4.2.2 Columns with $AlH_6O_{12}P_3$ 68
4.3 Applying the dispersion model to the E-curves 69
4.3.1 Columns with SiO_2 73
4.3.2 Columns with $AlH_6O_{12}P_3$ 79
4.4 Peclet number 80
4.4.1 Columns with SiO_2 80
4.4.2 Columns with $AlH_6O_{12}P_3$ 83
4.5 Porosity test 85
4.6 SEM characterization of post-experiment particles 86
4.6.1 Columns with SiO_2 86
4.6.2 Columns with $AlH_6O_{12}P_3$ 90
4.7 Effect of column compaction 93

5. Conclusions and recommendations.....97

5.1 Conclusions 97

5.2 Recommendations.....99

6. References.....100

7. Appendix.....109

7.1 Transforming the raw data to obtain the RTD function.....109

7.2 Convolution.....114

List of Tables

Table 1–1: Commonly used binders.....26
Table 2–1: The packed columns with the concentration of binder material used in a 10 wt% ethanol solution used to reinforce the TAN material. 38
Table 3–1: Precipitates of the SiO_2 binder (higher concentration) in different content of ethanol 41
Table 3–2: Precipitates of the SiO_2 binder (lower concentration) in different content of ethanol 41
Table 3–3: Precipitates of the $AlH_6O_{12}P_3$ binder (higher concentration) in different content of ethanol 42
Table 3–4: Precipitates of the $AlH_6O_{12}P_3$ binder (lower concentration) in different content of ethanol 43
Table 3–5: The contents of binder solution 46
Table 3–6: The contents of binder solution 49
Table 3–7: The contents of SiO_2 solution containing different amount of ethanol.....54
Table 3–8: The contents of $AlH_6O_{12}P_3$ solution containing different amount of ethanol.....56
Table 4–1: Numeric determination of the output signal using discrete convolution. 72
Table 4–2: Pe and t_m calculated by convolution based on no column and empty column.....94
Table 7–1: data points of the original concentration curve 111
Table 7–2: C(t) and E(t).....112
Table 7–3: Calculating t·E(t).....113

List of Figures

Figure 1–1: The measurement illustration of Residence Time Distribution 28
Figure 2–1: The test system for tracer injection 38
Figure 2–2: Chemical structure of Sulforhodamine B 39
Figure 3–1: Precipitates of $AlH_6O_{12}P_3$ in ethanol at higher and lower concentration. Labels on data points are the weight of precipitates. 44
Figure 3–2: Precipitates of $AlH_6O_{12}P_3$ at different mole of water/ethanol. Labels on data points are the ratio of the (mole of water)/(mole of ethanol) in the mixture. 45
Figure 3–3: SEM images showing particle structure at 10 μm of TAN binding with 0, 2.5, 5, 7.5, 10,15, 20 and 25 wt% SiO_2. 47
Figure 3–4: SEM images showing particle structure at 10 μm of TAN binding with 0, 2.5, 5, 7.5, 10, 15, 20, 30 40 and 50 wt% $AlH_6O_{12}P_3$. 50
Figure 3–5: SEM images showing particle structure at 10 μm of TAN binding with 5, 10 and 15 wt% SiO_2 at the presence of 0, 10 and 20 wt% ethanol. 55
Figure 3–6: SEM images showing particle structure at 10 μm of TAN binding with 15, 20 and 25 wt% $AlH_6O_{12}P_3$ at the presence of 0, 10 and 20 wt% ethanol. 57
Figure 3–7: Pressure drop in the columns of TAN reinforced by different amount of SiO_2 60
Figure 3–8: Pressure drop in the columns of TAN reinforced by different amount of $AlH_6O_{12}P_3$ 60
Figure 3–9: Hydraulic permeability of TAN reinforced by SiO_2 61
Figure 3–10: Hydraulic permeability of TAN reinforced by $AlH_6O_{12}P_3$ 61
Figure 4–1:Experimental RTD data of columns with lower SiO_2 content. 65
Figure 4–2: The length of packing before and after the test 66
Figure 4–3: Experimental RTD data of columns with higher SiO_2 content 66
Figure 4–4:Two flow patterns in a packed column. (a): flow in the column with packing materials of isoporous structure; (b): flow in a column with aggregates of particles. 67
Figure 4–5: Experimental RTD data of columns with $AlH_6O_{12}P_3$ 68
Figure 4–6: Steps to fit the model to RTD data and considering the signal distortion of the system 71
Figure 4–7: Results of E(θ) at different level of dispersion 74

Figure 4–8: E(θ) function of columns reinforced by a lower amount of SiO_2. .Using the "no column" data in the convolution model. 75
Figure 4–9: Empty Column in convection model and axial dispersion model. Using the "no column" data in the convolution model. 76
Figure 4–10: E(θ) function of columns reinforced by a higher amount of SiO_2. Using the "no column" data in the convolution model. 77
Figure 4–11: E(θ) function of all columns reinforced by SiO_2. Using the "no column" data in the convolution model. 78
Figure 4–12: E(θ) function of all columns reinforced by $AlH_6O_{12}P_3$. Using the "no column" data in the convolution model. 79
Figure 4–13: The relation of SiO_2 content and Pe. Using the "no column" data in the convolution model. 81
Figure 4–14: The relation of SiO_2 content and t_m. Using the "no column" data in the convolution model. 83
Figure 4–15: The relation of $AlH_6O_{12}P_3$ content and Pe. Using the "no column" data in the convolution model. 84
Figure 4–16: The relation of $AlH_6O_{12}P_3$ content and t_m. Using the "no column" data in the convolution model. 84
Figure 4–17: The porosity of TAN reinforced by different amount of binder 86
Figure 4–18: SEM images of particles reinforced by SiO_2 after flow tests 88
Figure 4–19: SEM images of particles reinforced by $AlH_6O_{12}P_3$ after flow tests 91
Figure 7–1: The original data (microvolts) versus time 109
Figure 7–2: The concentration curve (C curve) of the raw data 110
Figure 7–3: E(t) function 112
Figure 7–4: E(θ) function. 114
Figure 7–5 : The input signal C_{in} (in every 5 seconds) 115
Figure 7–6: Sample calculation in Excel using the "no column" data in the convolution model. 116
Figure 7–7 : E(θ) of the column with 2.5 wt% SiO_2 using the "no column" data in the convolution model. 117

Nomenclature

Abbreviation

PBR	Packed Bed Reactor
CSTR	Continuous Stirred-Tank Reactor
HPLC	High-Performance Liquid Chromatography
UHPLC	Ultra-High Pressure Liquid Chromatography
UHPSFC	Ultra-High Performance Supercritical Fluid Chromatography
SPP	Superficially Porous (Core-Shell) Particle
SEM	Scanning Electron Microscope
RTD	Residence Time Distribution
TAN	Twinned Alumina Nanoplates
CTAB	Cetyl Trimethyl Ammonium Bromide
SRB	Sulforhodamine B
SSE	Sum of Squared Errors

Symbols

C	Concentration (g/L)
C_{in}	Concentration in the detection system without column(g/L)
C_{out}	Concentration in the detection system with the column(g/L)
d_p	particle diameter (m)
E(t)	Distribution function for residence time (s^{-1})
E(θ)	Distribution function for dimensionless residence time (-)
E_{in}	Distribution function in the detection system (s^{-1})
E_{out}	Distribution function in the tested column (s^{-1})
E_{exp}	Distribution function obtained from experiments (s^{-1})
E_{conv}	Distribution function obtained from convolution (s^{-1})
F(t)	Cumulative distribution function (-)
κ	intrinsic permeability (mD)
L	Total length of the bed (m)
N_0	Total amount of tracer (-)

Pe	Peclet number based on Equation 14.
Re	Reynolds Number (-)
t, t'	time (s)
t_m	mean residence time (s)
v	velocity (m/s)
v_s	superficial velocity (m/s)

Greek Symbols

θ	dimensionless time (-)
θ_0	breakthrough time for laminar flow (-)
τ	expected residence time (s)
μ	dynamic viscosity (Pa·s)
ρ	density (kg/m^3)
ϕ_s	sphericity of the particles in the packed bed (-)
ε	porosity of the bed (-)

1. Introduction and literature review

1.1 Introduction and objectives

New packing materials and catalyst supports with high performance are gaining increased interest in the chemical and pharmaceutical industries. Packed bed reactors have high conversion rates, efficiency and productivity that are of crucial importance in many industries. There is also a need for better packing materials for chromatography to improve separation and throughput in the bioprocessing and analytical industries. Thus, the design and optimization of packing materials and catalyst supports as well as the selection, modification and the studies of the performance of these materials is very important. Good packing materials should meet the following requirements: a) provide a large surface area for separation or reaction to occur; b) not adsorb or react with the components in the flow; and c) have a strong mechanical structure to retain their integrity under compaction.

However, in both chromatography and packed beds, packings are still limited to spheres and non-isoporous materials. There has been a trend in studying particles with smaller sizes, but the potential of nanoplatelets has not been studied. Such phenomenon has brought our interest in studying new packings with new geometries. Therefore, to address this issue, this work has focused on nanoplatelets with isoporous properties.

In the field of new materials nanoscale particles, measuring between 1 and 100 nm, have enhanced properties compared to those at the single-molecule scale or the bulk scale.

Interest has also increased on the modification of catalytic materials and supports to intensify their existing advantages or cultivate the potential for other superior characteristics. Generally, the packing materials should meet two principal requirements: provide a large surface area for good contact and an open structure with good permeability for gas or liquid flow. Packing materials are usually of the structured or random type. Structured packings have an ordered array of particles while random packing does not have a fixed particle shape or size and particles are arranged randomly [1].

The most commonly seen and applied packing material in packed bed reactors or chromatography columns are ceramics, with alumina and silica being widely used due to their hardness, corrosion and heat resistance and high surface area. These properties make porous ceramics ideal packing materials in packed beds. However, modifications are needed to improve the performance of these ceramics to create a larger area for better radial mixing, and to establish a more open structure with better permeability.

The modification of the structure of porous ceramics or the synthesis of ceramic particles with controlled morphology at the microscale can be found in many research studies. Furthermore, non-uniform packing with random arrangement of particles are also drawing much attention [2]. Motivated by the current trend of research, new twinned alumina nanosheets (TAN) with a 2D/3D network with isotropic permeability were selected as the primary packing material to be further investigated in this work, as this 2D/3D network shows potential in providing better mixing, permeability and lower dispersion coefficients. The individual nano-platelet of TAN has

a very small size, which is 4 μm in length, 1 μm in width and 100 nm in thickness. Very fine nanoparticles have not been explored in chromatography columns or packed beds. Apart from the very small size, the irregular placement of alumina platelet presents various contact angles, thus creating iso-permeability when being used in a packed bed. This iso-permeability can provide numerous sites or paths in various directions for the components in the flow to contact and mix at the micro-level, which can be beneficial for improving mixing in packed beds.

The objectives of this work are to explore the potential of nanosized 2D/3D particles in packed beds or chromatography columns and study the performance of the column with the synthesized materials and determine the dispersion in the 2D/3D network of small particles.

1.2 Packing and supports for reaction and chromatography

Reactors are at the center of chemical processes. They are unquestionably the most vital part of many industries as they transform raw materials into valuable chemicals. Various essential and important products that modern society largely depends on are generated in such reactors. Chemical engineers are faced with the challenge of ensuring profitability in a rapidly growing and evolving market. Packed beds are one of the most common reactors used in the chemical industry due to their high conversion rate per catalyst weight compared to other catalytic reactors. Catalyst supports that offer open access to reactants and permit the release of products away from the catalyst surface are important elements of an efficient reaction. The design of efficient packing materials that offer high mass transfer and better mixing in the bed are key to higher productivity, better efficiency and a greener and safer operation [3].

1.2.1 Catalyst supports

The geometry and the material of the support plays an important role in the design and optimization of reactors. Bodke et al (1998) studied the performance of foam monolith catalyst supports impregnated with different catalysts for the oxidation of methane. They found that the effect of changing the type of support material was small but changing the catalyst had a larger effect on the results. The catalyst geometry contributed by the support also considerably affects the results. In some cases, the catalyst support may actually enhance catalytic activity [4]. Maestri et al (2005) examined three types of catalyst supports: foam monolith, honeycomb monolith and spheres (all wash-coated and having same catalyst volume fraction of 8.4%) for the partial oxidation of CH_4 and found out that foam shows the highest value of conversion. Thus, the choice of catalyst support can result in greatly different reactor performances [5].

Heck et al (2001) investigated the performance of single extruded monolithic supports for gas phase catalytic reactions and pointed out the major advantage of a monolith compared to a packed bed is a large open frontal area that can lead to a low pressure drop. Packed beds typically have a larger pressure drop which means larger resistance to flow and therefore a larger energy loss. There are still disadvantages that limit the application of monoliths. The monolith is essentially an adiabatic reactor limiting the control of temperature and it may not provide sufficient sites for catalysts to achieve a desired efficiency [6].

The morphology and pore size of the selected support materials have great influence on the stability and performance of the catalyst. Bagheri et al (2014) used titanium dioxide as a catalyst

support for Au nanoparticles and they pointed out that the size of Au nanoparticles is one of the most common factors affecting the catalyst activity. In order to achieve higher Au performance, the cluster size has to be less than 5nm [7].

Li et al (2015) synthesized 3D structured graphene as a high-performance catalyst support and deposited platinum on the support for methanol electro-oxidation. Their 3D support exhibits a foam-like structure with random pore sizes and the distribution of Pt particles was good with only a few aggregations observed [8].

Open supports also favor catalytic deposition. Activated carbon is very commonly used as the support for catalysts. Baroutian et al (2011) used palm shell-based carbon as the support and pure potassium hydroxide as a catalyst to produce methyl esters biodiesel. Activated carbon has an inert carbon skeleton and good physical or thermal stability with a large surface area, which makes it an ideal choice of catalyst support. In their work, potassium hydroxide presents a good dispersion supported on activated carbon (KOH/AC). Activated carbon retains the structure and the catalyst fills into the pores of the catalyst support. The catalytic activity remained high at 89.3% when they were employed for the third time. They pointed out that the decrease in catalytic activity is due to the leaching of the active sites to the reaction media [9].

Cheng et al (2015) studied the pore size of mesoporous silica supports on the catalyst performance. Iron catalysts were supported by mesoporous silica in a high temperature Fischer-Tropsch synthesis. They stated that smaller pores in silica resulted in higher iron dispersion with low extent of carbidization during catalyst activation. However, larger pore sizes lead to larger

iron particles and exhibit a higher extent of carbidization [10]. Xu et al (2016) prepared large pore volume γ-alumina and used it as a catalyst support for Fe based catalyst in phenol hydroxylation reaction. The pore size regulates the distribution of Fe across the support thus high pore volume is important for the internal diffusion of macromolecules. Their results show that the γ-alumina support with a larger pore volume had the greatest efficiency indicating the importance of the support in facilitating accessibility to catalytic sites [11].

Lobato et al (2016) assessed composite titanium silicon carbide (SiCTiC) as a catalyst support for proton-exchange membrane fuel cells. They deposited Pt nanoparticles on the support and found that the catalyst support has a substantial influence on the initial mean size of the catalyst particles. A higher Brunauer–Emmett–Teller surface area lead to a lower mean particle size thus a more efficient distribution of Pt nanoparticles [12].

1.2.2 Packed bed reactors and adsorption columns

Packed beds also have various applications as reactors for catalytic processes. They have many advantages, such as high conversion rate per weight of catalyst, more contact between reactant and catalyst and low cost of construction and operation. Mishra et al (2016) produced ethanol in a packed bed reactor filled with immobilized co-fermenting *Saccharomyces cerevisiae* GSE1618. *S. cerevisiae* GSE1618 was immobilized on Ca-alginate (2%) beads that have 3 different sizes (3,4 and 5 mm). They also investigated the reaction performance of different alginic acid concentration, bead size, glucose concentration, temperature and hardening time. Results proved that *S. cerevisiae* strain immobilized on 4 mm sized Ca-alginate bead show

significantly higher productivity and recyclability and they can be used up to 40 repeated fermentation batches [13].

Piskun et al (2016) reported their experiments on the catalytic hydrogenation of levulinic acid with Ru catalysts on various supports (Al_2O_3, TiO_2, and C) with particle sizes in the millimeter range in a continuous packed-bed reactor. These millimeter sized catalyst particles greatly enhanced mass transfer. Ru with Al_2O_3 support was found to be less active due to the high reactivity of Al_2O_3.The highest conversion was obtained with Ru catalysts on C support in the packed bed reactor [14].

Butterworth et al (2016) investigated the effect of particle size (180 μm to 2000 μm) of two packing materials (Al_2O_3 and $BaTiO_3$) on the conversion of CO_2 to CO and discharge characteristics in packed bed plasma reactors. Their results show that reactors with smaller particles (180 μm to 300 μm) can significantly increase CO_2 conversion by up to 70%. However, reactor breakdown voltage also increases when particle size decreases [15].

Ngoh and Lim (2016) studied the effects of particle size on heat transfer in gas fluidized beds using computational fluid dynamics. They conducted simulations with different particle sizes and gas superficial velocities. Their results show that the overall temperature difference between the gas and solid phases decreases with a decreasing particle size, which also results in an increase in conductive and convective heat transfer between the two phases [16].

Rifai et al (2016) studied the hydrodynamics of a three-phase micro-packed bed reactor with Au-Pd/TiO_2 catalyst and its effect on benzyl alcohol oxidation with pure oxygen. The catalyst in the packed bed has an average diameter of 65 μm. A selectivity of 93% to benzaldehyde was obtained due to the smaller particle size. [17].

Faridkhou and Larachi (2014) studied the effect of particle size and bed geometry on the flow hydrodynamics in micro-packed beds. It was found that using smaller particle sizes caused an earlier inception of the high interaction regime. However, they also pointed out that larger particle sizes and square bed geometry possess shorter transient times as compared to smaller particle sized and circular bed geometry [18].

Mishra et al (2016) used packed beds of Fenton modified *Hydrilla verticillata* dried biomass to adsorb chromium (VI) and nickle (II). They also investigated the effects of bed height, flow rate, concentration and particle size. Particles in 0.25 mm to 2 mm were examined. Results show that particles with smaller size (0.25 mm to 0.5 mm) exhibit best adsorption capacity. The large particle range leads to slower pore diffusion rate, as the diffusion path along the pores is larger and the resistance to diffusion is higher [19].

1.2.3 Chromatography columns

Packed columns are also widely used in chromatography. Packed column chromatography is a versatile separation method. In analytical chemistry, and separation science in particular, the quest for methods with low consumption of solvents, or environmentally friendly solvents is of

great significance [20]. Remarkable developments have taken place in the area of supports for chromatography in the past decade since sub-2-μm superficially porous particles became available. Small particle (less than 1.5 μm) columns have only been introduced recently and have not penetrated the market, however, the interest in developing new materials with small particle sizes is growing. These packings increase the speed of analysis while maintaining separation efficiency, which is a very important asset when analyzing large numbers of samples. However, small particle columns also present many other disadvantages, such as higher pressure limit (as high as 1200 bar) compared to conventional columns (400 bar) [21].

Superficially Porous (Core-Shell) Particle Packed Columns have been popular since the beginning of HPLC. The initial 5-μm SPP was designed for fast separation of macromolecules. The biggest advantage SPP columns have is low pressure drop compared to sub-2-μm columns. Monolith columns also exhibit potential but have been unable to replace traditional SPP. Monolith's small-sized skeletons and wide-through-pores can offer much higher efficiency compared to particle-packed columns. First generation silica monolith column achieved the same efficiency of a 4-μm silica column but with only 40%-50% pressure drop. However, the disadvantage is that the longest commercial silica monolith column is 100 mm, several of these have to be connected in series to achieve higher plate numbers [22].

Using small sized particles for chromatography columns is gaining interest in many research and studies. Sun et al (2016) packed a gas chromatography (GC) column with Porapak Q powder. The micro-fabricated packed column was able to completely separate 8 components with

separation efficiencies of 5800 plates/m. They also reduced the packing diameter down to 5–10 μm [23].

Treadway et al (2015) packed superficially porous particles around 1.5 μm in diameter into capillary columns for use in ultrahigh pressure liquid chromatography (UHPLC). The most efficient column of their experiments generated 520,000 plates/m. They also pointed out that serial column packing is an effective method which allows faster creation of multiple columns than by packing only one column per slurry [24].

Catani et al (2016) packed 2 columns with particles having a size of 1.9 μm (Titan C18), one with an average pore size of 80Å and another one with an average pore size of 120 Å. They investigated the influence of particle size distribution on the efficiency of the columns. Their results reveal that the columns show extremely small eddy dispersion (particularly particles with a pore size of 120 Å) and high efficiency (300,000 paltes/m) [25].

Gonzalez-Ruiz et al (2015) reviewed the performance of a column packed with small core-shell particles for use in liquid chromatography. The particles were highly homogeneous with a diameter of 1.3-5 μm with a solid silica core and a porous surface which shows superior performance compared to fully porous particles. They pointed out that small sized core-shell particles packed into small columns can deliver a level of performance that exceeds the capabilities of current columns [26].

Cabooter et al (2010) examined several commercially available fully porous and superficially porous HPLC columns and investigated the relation between particle size distribution and chromatography performance. The 7 columns they examined had particle diameters in the range of 2.6-3.5 μm. They observed a strong nearly linear correlation between the width of the particle size distribution and the parameters that can reflect the quality of the packing such as the minimum reduced plate height and the minimum reduced separation impedance. They pointed out that the performance of the current generation of fully porous particle columns can be significantly improved if the particle size distribution can be reduced [27].

Perrenoud et al (2012) compared the performance of ultra-high performance liquid chromatography (UHPLC) and ultra-high performance supercritical fluid chromatography (UHPSFC) using columns packed with sub-2- μm particles. They evaluated the influence of reducing particle size and found that optimal linear velocity and mass transfer were significantly enhanced for both UHPLC and UHPSFC when the particle size was reduced. The improvement brought by the deduction of particle size is greater in UHPSFC [28].

Aggarwal et al (2012) also studied the effects of particle size and through-pore size on chromatography performance in their review of chromatography techniques. They pointed out that small particles can lead to more uniform bed structure. However, the disadvantage of high backpressure for using small particles limits their applicability as column packings. They also pointed out that apart from small particle size, narrow particle size distribution is also an important factor for improving column homogeneity and performance [29].

1.2.4 Effect of particle shape

The study of fluid dispersion in packed beds started fifty years ago and there have been various research studying on the measurement and correlation of axial dispersion. The influence of the size and the shape of the packing materials on dispersion in packed beds has been studied. Packed beds with particles in the shape of spheres, cubes, Raschig rings, granular and other materials were investigated by several researchers.

Very early studies, by Ebach and White (1958) compared the axial mixing in packed beds of glass spheres, Raschig rings, Berl saddles and Intalox saddles. The glass spheres have a diameter of 1, 3 and 6 mm while the Raschig rings, Berl saddles and Intalox saddles each has a nominal size of 0.25 in. The plot of Peclet number, $d_p v/D_L$, and Reynolds number, $d_p v/\mu$ was generated and the shape as well as the size of packing materials were studied. The Peclet number varied from 0.3 to 1 for the range of Renolds number from 0.01 to 150. They found that the axial mixing is dependent on the size of particles but not the shape [30].

Carberry and Bretton (1958) measured the axial dispersion coefficient in packed beds of particles in ½, 1, 3, and 5 mm spheres and 2 and 6 mm in the shape of rings. The length of the packed beds varied from 6 to 36 in. Their results show the dispersion coefficient increases linearly with the Reynolds number (on a log-log scale) in the range of Re = 0.5 to 100 and the value of Pe is in the range of 1 to 100. They also found that the data for smaller particles (½, 1 and 3 mm) are uniquely correlated as a function of the Reynolds number [31].

More recently, Carvalho and Delgado (2003) studied the effect of liquid properties on axial dispersion in packed beds. The length of bed, particle size and particle shape were also investigated. Two materials, sand and ballotini were compared. Their results show that longitudinal dispersion coefficient is insensitive to the length of the bed and is also insensitive to particle size. However, particle shape has a significant influence on longitudinal dispersion. In the packed beds of sand, a lower Pe is observed, which indicates a higher dispersion compared to ballotini [32].

Delgado (2006) pointed out that the particle shape is a very important parameter in studying the dispersion in packed beds. A higher longitudinal dispersion a lower Pe can be observed in beds packed with sand and Raschig rings compared to those packed with spherical particles. Increased particle sphericity correlates with decreased dispersion. The term “sphericity” is defined as the surface area of a particle divided by the surface area of a sphere volume equal to the particle [33].

Han et al (1985) showed that when particles with a size distribution of maximum over minimum diameter equal to 7.3, the longitudinal dispersion coefficient are 2 to 3 times higher than uniform-size particles [34].

Moulijn and Swaaij (1976) pointed out in their work that packed beds with fine particles (diameter < 0.5 mm) have a lower Peclet number than those with large particles. At low Reynolds numbers, the axial dispersion is mainly caused by molecular diffusion. In their work, they summarized the literature data of axial dispersion of gases in packed beds with particles

sizes of 100 to 200 μm. These packed beds show a low range of Peclet number from 0.01 to 10. They stated that the reason for the higher dispersion (lower Peclet number) may be the occurrence of channeling due to a non-uniform distribution of fine particles. The non-uniform distribution results in high-density areas (agglomerates) inside the column which leads to the channeling in the packed bed. This phenomenon occurs to a greater extent in beds with small particles than in those with larger particles [35].

As presented in the above works, some researchers found that small particles exhibit lower dispersion and better performance in packed beds and columns; while some pointed out the performance of a packed column was irrelevant to particle size. Ceramic particles are commonly seen in their studies as packing materials. Therefore, alumina in particular, was studied for their potential.

1.3 Alumina and its applications

According to statistics, in 2015, the size of global high purity alumina industry was above 20 kilo tons. The demand for alumina in industries boosts the production and development of these materials. In addition, the demand for materials with heat resistance in the coating industry is also growing [36].

1.3.1 Interest in morphology control of alumina

Research on synthesizing alumina with enhanced properties, especially the control of physicochemical properties, has been popular for a variety of applications. The synthesis and production of alumina with tailored shape, controlled morphology, large pore volumes and narrow size distribution for improved performance is a key topic of ongoing research. Li et al (2017) synthesized super-microporous alumina with a pore size of 1 to 2 nm which was built on a nonionic surfactant template. The particles have a surface area of more than 650 m^2/g and possess a disordered "wormhole-like" structure with poly-crystalline walls, which can be used in separation, catalysis and gas adsorption fields. A readily available and inexpensive AEO-7 was the template and it was removed at 400 °C [37]. Isiguro et al (2005) fabricated porous alumina tubes with a homogenous structure by a centrifugal molding technology.

Polymethylmethacrylate (PMMA) was used as the pore foaming agent. An increasing PMMA amount shows increased porosity and a decreased fracture strength. Higher porosity exhibited a narrower scatter in fracture strength [38]. Chang et al (2017) produced well-dispersed α-Al_2O_3 plates with diameters ranging from 1 μm to 20 μm by molten salt synthesis. The Al_2O_3 generated from the decomposition of $K_3Al(SO_4)_3$ liquid phase which formed from the reaction of K_2SO_4 salt with $Al_2(SO_4)_3$ precursor. These platelet powders are widely used as reinforcements in metals, ceramics and polymers [39]. Lillo and Losic (2009) fabricated anodic alumina oxide with through-hole pore morphology using wet chemical etching and studied the experimental results at different anodization and etching conditions. They also developed an electrochemical detection method to monitor the pore opening process and achieve controllable and reproducible pore-opening [40]. Suchanek and Garcesb (2010) synthesized α-Al_2O_3 nanosheets and

nanoneedles using a low temperature hydrothermal method in the presence of SiO_2 and H_3BO_3 morphology modifiers. The nano sized α-Al_2O_3 particles showed strong crystallographic c- or a-faceting with high BET surface areas up to 40 m^2 g^{-1} and also exhibited high thermal stability [41]. Jiao et al (2012) investigated the morphology and structural properties of the transition alumina derived from aluminum hydroxides. They synthesized aluminum hydroxides through the acidification of sodium aluminate solution using single organic di-ester or di-acid as pH adjustor and aluminum chelating agent. These alumina hydrates show diverse morphologies and the alumina they transformed also have different structural and textural properties [42].

1.3.2 Application of non-porous alumina

Alumina has been widely used in ceramics applications and various grades and purities in both porous and non-porous varieties can be found in many studies. Non-porous alumina based ceramics can be found in the applications of structural material. Ruckenstein and Malhotra (1976) used non-porous alumina films as supports and deposited platinum crystallites on them by a sputtering technique [43]. Yukhimchuk et al (2015) used non-porous alumina as the structural material for devices handling tritium at elevated temperatures. The key problem in designing devices for handling tritium at elevated temperatures is the leakage of tritium through structural materials. The application of non-porous alumina can offer a solution to the problem, as the ceramic shell allows direct inductive heating without noticeable temperature increase of both impermeable and protective vessels [44]. Amin et al (2012) also used non-porous alumina as nickel supports to catalyze methane cracking and compared the performance to porous alumina supports. Catalyst supports play an important role in methane cracking, as they should provide good catalyst distribution that does not interact with the catalyst. Their results show that non-

porous alumina supports performed better in terms of cracking during the first cycle. However, after full regeneration, the performance of porous alumina becomes considerably better. Therefore, the type of the support has an important effect on the catalyst performance [45]. Swecker and Datye (1990) studied the reactivity of non-porous alumina and compared to that of γ-alumina for the decomposition of ethanol, 1-proponal and t-butanol. They found that the product distribution on both aluminas were similar but the non-porous alumina was more active and the activation energy for the reaction was lower on non-porous alumina [46].

1.3.3 Application of porous alumina

Porous alumina has a wide application as a material to make ceramic membranes. Masuda and Hasegwa (1997) investigated in the self-ordering of cell arrangement of anodic porous alumina formed as a porous film with an ideal hexagonal honeycomb structure, which can be applied in micro- and ultrafiltration [47]. Cachero et al (2017) fabricated metal-organic framework (MOF) films on porous alumina tubes which were employed as supports. This MOF with porous alumina supports has both good permeability and selectivity for membrane applications [48]. Ahn et al (2017) also prepared a macroporous alumina as supports for a hydrogen selective silica-zirconia composite membrane and it showed good permeation properties and hydrothermal stability [49]. In the preparation of membranes, the multi-layer structure is one of the properties that various experiments are focusing on. These asymmetric membranes were typically composed of a support layer, a structure fitting layer and a top layer. The top layer performs the separation and the other layers act as the support of the thin layer. Many methods can be applied to form a multi-layer membrane. The sol-gel method is a preferable method for tailoring the top

layer with desired characteristics [50]. Other methods for the synthesis of ceramic membranes include extrusion, tape casting, pressing, dip coating, electroless plating, slipcasting, chemical vapor deposition (CVD), anodic oxidation and freeze-casting [51].

Porous alumina is also widely used as a template for the fabrication of nanostructures. Masuda and Satoh (1996) fabricated a highly ordered gold nanodot array using anodic porous alumina as an evaporation mask, which can form uniformly sized and site-controlled gold dots. Anodic porous alumina had an ordered honeycomb structure therefore using it as a mask lead to good uniformity in diameter and spacing of the holes. The dot arrays in nanometer scale can be applied in electronic and optoelectronic devices [52]. Martin et al (2014) employed a 3D anodic porous alumina as the template to fabricate a 3D and ordered nanostructure of Bi_2Te_3 and polystyrene. Template-based synthesis method is applied mostly for the fabrication of 3D nanostructures [53]. Attar and Hassani (2015) fabricated TiO_2 nanowire arrays by liquid-phase deposition using porous alumina as templates. Their results show that the nanowire arrays of TiO_2 have an average width of about 50-80 nm and length in microns with a smooth and uniform geometry [54].

Porous alumina can find applications in coating, adsorption, biomaterials and other areas. Banerjee et al (2015) designed a prototype counter-flow heat exchanger comprising alumina tubes filled with alumina reticulated porous ceramic foam (RPC), as porous alumina provides high surface area and low pressure drop. Their results show that RPC provides a 9-fold increase in heat transfer compared to bare tubes [55]. Li et al (2015) deposited porous alumina coatings on high-efficiency gas turbines and the porous coating exhibited negligible wear weight loss.

Flamed-sprayed alumina coatings with high porosity have potential for use as abrade coatings in gas turbines operating at high temperatures [56]. Qin et al (2016) applied porous alumina in a fluidized bed combustor and conducted combustion of polypropylene. They found that the combustion in porous alumina bed resulted in enhanced efficiency and reduced pollutant emission [57]. Anodic porous alumina has also attracted interest in biomedical field. Toccafondi et al (2014) investigated the feasibility of anodic porous alumina as a surface for the development of analytical biosensors and their measurements demonstrated possible application of anodic porous alumina as biosensor and drug carrying device [58].

1.4 Twinned Alumina Nanosheets (TAN)

TANs were first reported by Roebuck and Tremblay (2016). They are formed by the self-assembly of twinned nanosheets into porous 3D structures due to the presence of surfactant monomer in ethanol-water mixtures. The shape, thickness and twinning of nanosheets are controlled by varying the concentration of ethanol and surfactant in the synthesis. Particles synthesized with a critical micelle concentration of cationic surfactant cetyl trimethylammoniumbromide (CTAB) in 50% ethanol-water mixtures presented the most permeability, the thinnest size and a twinned 2D/3D structure [59].

The particles synthesized had a length of 4 μm, width of 1 μm and thickness of 0.1 μm. Apart from the small size, these particles also present a very high porosity of 88% with 5.7 m^2/g in macroscopic surface area. The hydraulic permeability was very high at 714 mD for a 0.2 μm pore size dynamic membrane. This high porosity and permeability make them ideal for

membrane applications. Furthermore, the unique 2D/3D structure makes the permeability anisotropic, which is more advantageous because anisotropic permeability enables the flow to pass through in various directions thus reducing the possibility of membrane fouling. This advantage makes TAN promising for use as dynamic membranes (DM) [59].

In another work of Roebuck and Tremblay (2016), they deposited the aggregates of TAN on a substrate and produced densely packed dynamic membranes. The flux decline profile was established to investigate the performance of TAN as dynamic membranes. The DM of TAN began at the fluxes in the range of 7000-11,000 l/(m^2h) and still maintained in the same range over the course of the 3L filtration run, while other tested DMs declined to the range of 400-1000 l/(m^2h) . No foulant was observed on the DM of TAN during the test. Their DM also performed better than the majority of DMs obtained in the literature based on turbidity removal [60].

Due to its high anisotropic permeability and small size, TAN is also promising in packed beds or columns as packing materials and catalyst supports. However, whether these nanosheets have enough resistance to the compaction brought by the flow in order to be applied as packing materials or catalyst supports in the column is unknown. Therefore, their resistance to compaction must be tested. They should also be reinforced if they do not have the desired strength or hardness.

1.5 Binders for ceramic materials

Surface modification of alumina also presents in many research in which the surface of alumina is coated. For example, to reduce the fouling of the membrane which is a significant obstacle for separation processes, SiO_2 is deposited on alumina by a sol-gel process to form a uniform

inorganic coating layer, as SiO_2 has low isoelectric points and can generate electrostatic repulsion forces when the membrane is separating humic acid. The negatively charged SiO_2-coated membrane can prevent adsorption of similarly charged humic acid, therefore reducing the fouling of the membrane [61].

1.5.1 Applications of binder materials in enhancing strength of ceramics

Mechanical strength is a key parameter in ceramic membrane synthesis. Binders play an important role in improving the strength. Coating the ceramics with another material also presents interest in the field of metal-matrix composites and the production of multi-layer ceramic materials, in which case binders are often utilized to achieve such goal in the preparation of ceramic membranes. Coarse and inexpensive raw materials (natural zeolites, kaolin, clay, diatomite, etc.) can be used as the substrates for the deposition of membrane layers. Then a micro-filtration layer is deposited with the involvement of a binder to stabilize the membrane structure. This is a very promising method to fabricate ceramic membranes with a desired selectivity that costs less than commercially available membranes. Ivanets and Agabekovb (2017) deposited a layer of fine silica on natural quartz sands in an aqueous solution of an aluminosilicate binder. They were able to synthesize the membrane with a heat treatment at 600°C while traditional process requires high calcination temperature (above 1400°C) [62]. Geng et al (2016) worked on binding hollow alumina spheres with closed-cell alumina using a high-temperature binder. The micro-structure and mechanical properties were controlled by adjusting the content of alumina spheres and the binder. The compressive strength of the resulting membrane was enhanced [63]. Bukhari et al (2017) used the clay kaolin as the binder for silicon-carbide particles and fabricated clay-bonded SiC flat tubular porous layers with a high

open porosity and high strength [64]. Zaitsev et al (2016) studied the influence of artificial ceramic binders on silica carbide and high-alumina fireclay. A thin film of mullite was formed at the surface that leads to improvement of the material properties [65]. Yuan et al (2017) studied the properties of mullite-bonded fibrous ceramics. Al_2O_3 and SiC were used as the binder and a gel-casting method was utilized for the fabrication of the ceramics, which showed a bird nest structure. The new formed materials have an increased strength [66].

1.5.2 Selection of binders

The selection of binder directly affects the material properties and the structure of the ceramic and the amount of the binder also plays a crucial role in the performance of the synthesized materials. Hence, it is necessary to choose the binder and optimize the content that affects the morphology and strength [67]. Organic and inorganic binders both have various applications in the fabrication of ceramics. Organic binders are used in the molding process and are lost in calcination. They are important in minimizing defects during calcination. Among different types of organic binders, Polyvinyl alcohol (PVA) and polyvinyl butyral (PVB) are the most commonly used ones. Das and Maiti (1998) used PVB as the binder and polyethylene glycol (PEG) as plasticisers for alumina powders by a tape casting process [68]. Lambert and Gonzalez (1999) synthesized γ- Al_2O_3 membrane with the PVA and PEG as the binder using a sol-gel method. The process also involved dilute HCl as a peptization agent. The resulted membranes had an increased surface area, pore volume and pore diameter [69]. In the work of Vlasea et al (2013), PVA was also used as the binder for the fabrication of calcium polyphosphate bio-ceramic with micro-sized channels for bone and osteochondral tissue regeneration [70]. Shimamura et al (2017) fabricated porous alumina with a surface layer composed of alumina

platelets by means of direct foaming. The alumina platelets were prepared with novolac-HexaMethyleneTetramine (HMT) as the binder as well as a blowing agent. The platelets were aligned parallel in the surface and resulted a 94% increase in bending strength compared to porous alumina without this surface layer [71]. Sarkar (2014) prepared multichannel tubes with alumina and clay using methocel as the binder, which resulted in a crack-free straight and mechanically strong porous clay-alumina ceramics with a low average pore size of 1 μm and porosity of 39%. This type of multichannel tubes can find applications in ultrafiltration and nanofiltration [72]. Methocel was also used as the binder in the synthesis of clay-alumina capillary tubes [73]. Duman et al (2012) fabricated a ceramic composite constituting 78 wt% WC, 16 wt% TiC and 6 wt% Co using a powder metallurgy process with stearic acid as the binding agent. The addition of stearic acid resulted in high porosity and low relative density [74].

1.5.3 Inorganic binders

Though organic binders provide many choices due to their low cost and easy application, inorganic binders exhibit increasing focus in recent research and studies. Chen et al (2017) studied the efficiency of bonding networks with different binders. Their experiments showed that SiO_2 and α-Al_2O_3 micropowders can enhance the strength of castables at low temperature, but excessive amount negatively affected the workability of the castables [75]. Fernando and Chung (2001) prepared alumina fiber based membranes with acid phosphate, colloidal alumina, monoaluminum phosphate and three types of colloidal silica binders at different binder contents. They studied the performance of different binders and membranes they produced with 5 wt% to 10 wt% acid phosphate binder exhibited the highest flexural strength and compressive strength [76]. Chiou and Chung (1993) studied the influence of P/Al atom ratio (ranging from 1 to 23) of

the acid phosphate binder and aluminum-matrix on the compressive strength. A P/Al atom ratio of 23 showed the lowest pressure drop and the best bonding structure [77]. Birchall et al (1987) explained the effect of $AlPO_4$ binder on the mechanical properties of powder compacts and illustrated the potential of phosphate-bonded refractories [78]. Toy and Whittemore (1989) studied the performance of several calcined aluminas with orthophosphoric acid at fairly low curing temperatures. The orthophosphoric acid binder and the alumina formed crystalline $Al(PO_3)_3$ phase which is the effective bonding phase. The formation of $AlPO_4$ should be avoided as it causes lower strength [79]. Sodium aluminosilicate was also used as binder in the preparation of a tubular macroporous ceramic substrate containing quartz sand in the main component. It showed positive effects on the structure and the properties of the resulting materials [80]. Boehmite sol having a pH of 3.6 was used as a binder with alumina powders in a recent work of Ray et al (2015). They prepared a macroporous pure alumina capillary membrane and the addition of binder resulted in an acceptable mechanical strength at a relatively low temperature and low fouling characteristics compared to ceramics synthesized with organic binder [81]. Szafran et al (2003) carried out experiments using NaH_2PO_4 as a binding agent for ceramic kaolin samples. NiO and CoO additives were used as tempering agents. Kaolin sintered with NaH_2PO_4 showed 3 to 4 times higher bending strength. The effect of the binder NaH_2PO_4 additive relied on the formation of NaPO3 which reacted with kaolin and created a series of compounds leading to compact ceramic material of advantageous properties [82].

1.5.4 Silica binder

Silica as the inorganic binder can be found in various research and studies. Koohestani et al (2016) investigated the influence of nano-silica on the compressive strength of cemented paste backfill and their study showed that with the addition of nano-silica, the micro-structure and the

compressive strength were enhanced [83]. Liu et al (2014) investigated the adhesion and catalytic activity of 3 colloidal silica binders, acidic, neutral and basic colloidal silica. Their studies show that zeolite coating using basic colloidal silica exhibits the smoothest surface with higher homogeneity and adherence strength. Basic colloidal silica also shows the highest and most stable catalytic activity compared to other binders [84]. Hu et al (2016) fabricated alumina fiber-based porous ceramics with silica sol as the binding agent. The materials with optimal properties were obtained with 5 wt% silica sol and 5 wt% PVA which acted as the dispersion agent [85]. In a study of Yu et al (2014), nano-silica was applied as a binding agent on ultra-high-performance concrete (UHPC) and its effect on the hydration and microstructure was investigated. It was reported that the highest mechanical properties were obtained with only 3.74% by the mass of the binder. Moreover, the addition of silica significantly compensates the retardation effect caused by the high amount of superplasticizer which was utilized to produce UHPC in their study [86]. Sun et al (2014) considered 10% silica binder optimal in their research where fibrous zirconia ceramic with ultra-high porosity (72-89%) were synthesized using silica as the binder. The microstructure of the materials they synthesized showed successful bonding at fiber junctions and an optimal thermal and mechanical properties were also obtained [87].

In summary, the commonly seen binders in industry can be found in Table 1-1.

Table 1–1: Commonly used binders

Binder	
Organic polymer	Polyvinyl alcohol
	Polyvinyl butyral
	Polyethylene
	Polyacetal
	Acrylic resins
	Wax emulsion
	Polyethylene glycol
	Organosilicon polymer
	Alcohol + Wax
	Thermoplastic resin + N_2
Silica binders	Silica
	Silica + Latex
Silicate binders	Alkali metal silicate
	Water glass (sodium silicate)
	Aluminosilicate
	Sodium aluminosilicate
	Sodium phosphate monobasic
Phosphate binders	H_3PO_4
	$Al_2O_3 + H_3PO_4$
	$AlPO_4$
	$AlPO_4 + (NH_4)_3PO_4 + Na_3PO_4$
	$H_3PO_4 + C + SiC$
	$Al(H_2PO_4)_3$
	NaH_2PO_4
Compound binders	Clay
	Bohemite

1.6 Characterization of packed beds

The objectives of this work are to reinforce the structure of TAN by binders, use the reinforced TAN as packing materials in packed beds and study the dispersion in the packed beds in order to validate if the reinforced TAN can be applied as packing materials or catalyst supports. Thus, it is important to characterize the packed beds or columns.

The Residence Time Distribution (RTD) is commonly used to characterize flow behavior and mixing performance in a non-ideal mixing or reaction system. The RTD describes the probability distribution function versus time that an element stays inside one or more unit operations in a continuous flow system. Various chemical processes, such as polymers, pharmaceutical, food, plastics and catalysts productions use RTD to characterize reaction systems [88]. The idea of using RTD to analyze the performance of reactors was first proposed in a pioneering paper by MacMullin and Weber [90].

The RTD can be used to compare the behavior of real reactors to their ideal models and troubleshoot existing reactors. The theory of residence time distributions generally begins with three assumptions:

1. The reactor is at steady-state.
2. Transports at the inlet and the outlet takes place only by advection.
3. The fluid is incompressible.

In an ideal plug-flow reactor, all the atoms of material spend exactly the same amount of time inside the reactor. Similarly, in an ideal batch reactor, all the atoms of a material have spent an identical length of time in the reactor. The time the atoms have spent in the reactor is called the residence time of the atoms in the reactor [91].

The RTD is determined experimentally by injecting an inert chemical, molecule, or atom, called a tracer, into the reactor and then measuring the tracer concentration, C, in the effluent stream as a function of time [91]. Tracer injection is the most commonly used method for characterizing

RTD of a reactor. It can be defined as injecting one or more tracers—usually chemical compounds—in order to estimate its flow and other properties [92]. The tracer should have physical properties similar to those of the reacting mixture and be completely soluble in the mixture. It also should not adsorb on the walls or other surfaces in the reactor. The latter requirements are needed so that the tracer's behavior will honestly reflect that of the material flowing through the reactor. Colored and radioactive materials along with inert gases are the most common types of tracers [91]. Fig 1-1 illustrates the measurement of the RTD.

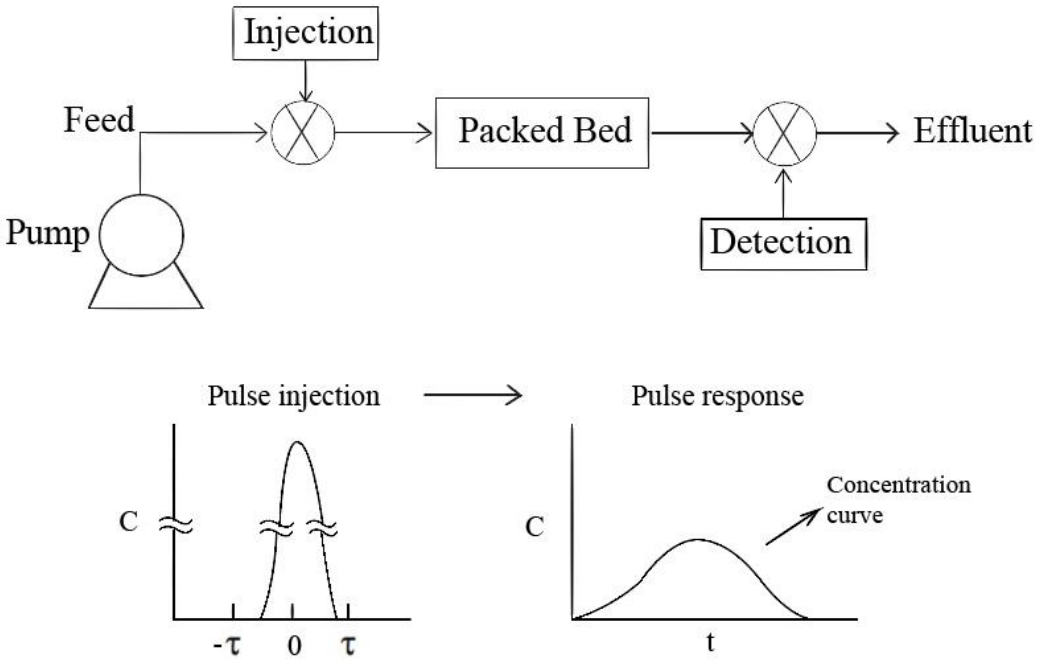

Figure 1–1: The measurement illustration of Residence Time Distribution

Tracer injection requires the introduction of a very small volume of concentrated tracer at the inlet of the reactor, such that it approaches the Dirac delta function. Although an infinitely short injection cannot be produced, it can be made much smaller than the mean residence time of the vessel. If a mass of tracer, M, is introduced into a vessel of volume V and an expected residence

time of τ , the resulting curve of concentration C(t) can be transformed into a dimensionless residence time distribution curve by the following relation:

$$E(t) = \frac{vC(t)}{N_0} \ , \tag{1}$$

$$dN = vC(t)dt; \ \ N_0 = \int_0^\infty vC(t)dt \ , \tag{2}$$

where N_0, v, C(t) indicate the total amount of tracer, volumetric flow rate, and concentration of tracer measured at outlet with residing time = t.

$$E(t) = \frac{C(t)}{\int_0^\infty C(t)dt} \quad . \tag{3}$$

The distribution of residence times is represented by an external residence time distribution or an exit age distribution, E(t). The function E(t) has the units of time^{-1} and is defined such that:

$$\int_0^\infty E(t)dt = 1 \ . \tag{4}$$

The fraction of the fluid that spends a given duration, t inside the reactor is given by the value of E(t)dt. The fraction of the fluid that leaves the reactor with a residence time less that t_1 is:

$$F(t_1) = \int_0^{t_1} E(t)dt \ , \tag{5}$$

where F(t) is called 'cumulative distribution'.

Thus, the fraction of the fluid that leaves the reactor with an age greater that t_1 is:

$$1 - F(t_1) = 1 - \int_0^{t_1} E(t)dt = \int_{t_1}^{\infty} E(t)dt \ .$$

(6)

The average residence time is given by the first moment of the age distribution:

$$t_m = \frac{\int_0^{\infty} tE(t)}{\int_0^{\infty} E(t)dt} = \int_0^{\infty} tE(t)dt \ .$$

(7)

If there are no dead, or stagnant, zones within the reactor, then t_m will be equal to τ, the residence time calculated from the total reactor volume and the volumetric flow rate of the fluid:

$$\tau = V / v = t_m.$$

(8)

Frequently, a normalized RTD is used instead of the function E(t). If the parameter θ is defined as:

$$\theta = \frac{t}{t_m} \ ,$$

(9)

a dimensionless function $E(\theta)$ can be defined as :

$$E(\theta) = t_m E(t) \ ,$$

(10)

and plotted as a function of θ. The quantity represents the number of reactor volumes of fluid based on entrance conditions that have flowed through the reactor in time t.

The purpose of creating this normalized distribution function is that the flow performance inside reactors of different sizes can be compared directly. For example, if the normalized function $E(\theta)$

is used, all perfectly mixed continuous stirred-tank reactors (CSTRs) have numerically the same RTD. If the simple function E(t) is used, numerical values of E(t) can differ substantially for different CSTRs.

Models can be applied to characterize a packed bed and study deviations from the ideal behavior. For example, the tank-in-series model can be used for stirred tanks; the plug flow model can be used for packed bed reactors and a convection model can be used in open tube flow [93].

2. Experimental

2.1 Materials

Aluminum dihydrogen phosphate (50% w/w solution) was purchased from Fisher Scientific and colloidal silica (40% w/w solution) was purchased from Sigma-Aldrich Canada. Sodium hydroxide pellets, cetyl trimethylammonium bromide (CTAB), anhydrous ethanol and the tracing dye Sulforhodamine B (powder) were purchased from Sigma-Aldrich Canada. Aluminum chloride hexahydrate (99%, nitrogen flushed) was purchased from Acros Organics. Cellulose filter paper (Whatman #4) and Whatman glass microfiber filter paper were purchased from Fisher Scientific. Teflon tubes (1/8 in.), stainless steel fittings and connections were purchased from Swagelok Canada.

The oven used for calcination was a Thermo FB1315 Benchtop Muffle Furnace (Thermo Scientific, Massachusetts). The autoclave used for particle synthesis was a Teflon-lined stainless steel autoclave (Parr Instrument Company, Illinois). Scanning electron microscope (Phenom Pro Desktop SEM (Nanoscience Instruments, Virginia) at 5kV and 10kV) was used to characterize the synthesized particles. Particles were mounted on aluminum stubs (Ted Pella, Redding, California) as samples for SEM.

The pump used to test the pressure drop and flow behavior was a Waters 600E Multisolvent Delivery System (Waters Limited). The auto sampler used for the injection of dyes was a Waters

717 Auto Sampler (Waters Limited). The spectrometer used was a Spectronic 20D+ (Thermo Scientific, Massachusetts) with a QS 1.000 flow cell.

2.2 Methods

2.2.1 2D/3D nanosheet (TAN) synthesis

The 2D/3D Twinned Alumina Nanosheet structures (TAN) were synthesized according to previous work performed in our laboratory on the self-assembly of twinned boehmite nanosheets into porous 3D structures [59]. 2D/3D TAN structures were produced as follows: 1.45 g aluminum chloride hexahydrate was dissolved in deionized water under vigorous mixing. Sodium hydroxide pellets were added to the suspension of aluminum chloride hexahydrate to raise the pH to 14. The surfactant CTAB was dissolved in anhydrous ethanol and then added to the precursor solution followed by continuous mixing for 24 hours at room temperature to enable a complete reaction. After the reaction, the mixture was poured into a Teflon-lined stainless-steel autoclave (Parr Instrument Company, Illinois), sealed and heated to 165 °C for 12 hours under autogenous pressure. The precipitates formed at the bottom of the autoclave were collected, lightly covered and placed in a fume hood to dry in open air. The precipitates were then calcined at 600 °C for 4 hours. After calcination, the particles were stored for later experiments and analysis.

2.2.2 Binder solubility analysis

In this work, we wish to bind the nanosheets at their respective contact points to form a strong structure that can resist compaction. The solution containing the binder must have a low surface tension in order to leave the pores open on evaporation. The best candidate liquids to perform

this operation are lower alcohols such as methanol, ethanol, isopropanol or butanol. Methanol is toxic and is limited in its ability to suppress the surface tension of water. The solubility of salts in isopropanol and butanol is less than in ethanol. Given the desirable characteristics of lower surface tension at comparable concentrations and an appreciable salt solubility, ethanol was selected as a compatibilizing solvent in the deposition of the binder material.

Before binding the TAN structures, the binder solution was diluted with water or ethanol solution. High concentrations of binder will most likely clog the original 3D isoporous structure of the TAN, so it is important to avoid such accumulation. The involvement of ethanol can bring a homogeneous dispersion. Thus, the solubility of the binder in ethanol needs to be figured out to achieve this goal and to avoid any precipitates. Solutions of binder material containing 10, 20, 30, 40 and 50 wt% ethanol were prepared and shaken vigorously. The mixture was allowed to settle overnight, centrifuged and precipitates weighed.

2.2.3 Binding of TAN

In order to study the binding performance of the two binders on TAN, experiments were carried out using both SiO_2 and $AlH_6O_{12}P_3$ binders. A given amount of TAN (0.1 g) was added to 60 mls of water and shaken vigorously. The solution was vacuum filtered on a Whatman #4 cellulose filter paper then washed by 200 mL deionized water. The TAN formed a uniform coating on the filter. Two hundred grams of binder solution containing ethanol were slowly poured over the TAN filter cake while vacuum was maintained. After the solution passed through the filter, the filter was placed in the fume hood to dry naturally. It was then calcined for 4-hours at 600 °C for particles reinforced with $AlH_6O_{12}P_3$, or at 1000 °C for particles reinforced with the SiO_2 binder.

The temperature of 600 °C for $AlH_6O_{12}P_3$ was selected to avoid the formation of undesirable phase transformation that occur above 800 °C.

To study the influence of the concentration of ethanol on the dispersion of particles, a comparative experiment where particles made with different amounts of ethanol was also conducted.

2.2.4 Column packing

After synthesis and characterization by SEM, the particles were packed in a 2-inch long Cole-Parmer PTFE tubing (1/8 in. OD x 1/16 in. ID) for testing. Two pieces of 1/8 in. disks of Whatman glass microfiber filter were cut out and placed at the end of each column. The empty column was connected to a vacuum pump. The particles were placed in a weighing dish and drawn by vacuum into the column. They gradually accumulated at the end with the glass filter. A preweighed amount (0.01 g) of particles was packed in each column. All columns had approximately the same length after packing (4 cm). After drawing the particles in the column, 0.024 g of glass wool was inserted and slightly pushed towards the end of the particles to make sure the particles remain in the packed bed.

2.2.5 Measure the pressure drop of the packed columns

The primary objective of this work is to improve the resistance to compaction of the TAN particles in a packed bed. Traditional methods for measuring the mechanical strength or hardness of materials are mostly carried out by indentation tests which use an indenter of specific geometry to compresses the surface of the tested specimen with a known applied force. This test

is difficult to use on powders and would provide limited information on the performance of the particles in a packed bed. The best method to determine the suitability of the packing material for use in this application is to determine the resistance of the particles to compaction by subjecting them to fluid flow. The change in the pressure drop across a column on increasing fluid flow can be used to validate the improvement in the strength or hardness of a packing material.

The pressure drop for a fluid flowing through a packed bed of mostly spherical particles can be represented by the Carmen-Kozeny equation as shown in Eq 11 [94].

$$\frac{\Delta P}{L} = -\frac{180\mu}{{\phi_s}^2 {d_p}^2}\frac{(1-\varepsilon)^2}{\varepsilon^3} v_S \quad , \tag{11}$$

where ΔP is the pressure drop, L is height of the bed, μ is the viscosity of the fluid, $\phi_s$is the sphericity of the particles in the packed bed, $d_p$is the diameter of the particle, ε is the porosity of the bed, v_s is the superficial velocity. Darcy's law can also be used to characterize the bed as follows:

$$v_s = -\frac{k}{\mu}\frac{\Delta P}{L} \quad , \tag{12}$$

where k is the absolute permeability of the bed. According to Darcy's law, if the bed remains unchanged, an increase in the velocity of the fluid will lead to an increase in the pressure drop across the bed. Networks of particles with greater integrity will maintain their structure and void volume. Plots of pressure drop vs fluid velocity should be linear in this case. In this work, the objective is to validate the involvement of binder strengthens the structure of TAN. Hence, linear

pressure drop vs flow curves attest to the integrity of the packed bed and can be used to verify the improvement in the strength of the particle network.

A solution of 10 wt% isopropanol in DI water was used as a mobile phase in all tests. When water was used as a mobile phase, over time, small air pockets could be observed in the packed bed. The use of 10% isopropanol in DI water reduced the surface tension of the mobile phase and eliminated the formation of air pockets. The packed column was connected to an HPLC pump to determine the pressure drop across the column. The pressure was read from a pressure gauge temporarily located at the entrance of the column and the outlet of the column was open to atmosphere. This pressure gauge was removed when the RTD tests were later performed. The isopropanol solution was pumped by the HPLC pump into the column then collected in an effluent container and weighed. The flowrate setting on the pump was verified by weighing the column effluent for a given time. The values of the flow rate shown on the pump had an accuracy of 95% (flow rate on screen: 0.2 mL/min, flow rate measured: 0.19 mL/min). For all experiments the flow rate was set by the pump. The pressure changed on increasing flowrate and was recorded for analysis. A total of 11 columns were packed with TAN and a given amount of binder. The column identification and concentration of binder material used in the 10 wt% ethanol solution to reinforce the TAN material can be found in Table 2-1.

Table 2–1: The packed columns with the concentration of binder material used in a 10 wt% ethanol solution used to reinforce the TAN material.

Columns	Materials
1	TAN
2	TAN + 2.5 wt% SiO_2
3	TAN + 5 wt% SiO_2
4	TAN + 7.5 wt% SiO_2
5	TAN + 10 wt% SiO_2
6	TAN + 15 wt% SiO_2
7	TAN + 20 wt% SiO_2
8	TAN + 5 wt% $AlH_6O_{12}P_3$
9	TAN + 10 wt% $AlH_6O_{12}P_3$
10	TAN + 15 wt% $AlH_6O_{12}P_3$
11	TAN + 20 wt% $AlH_6O_{12}P_3$

2.2.6 Tracer injection

Figure 2-1 shows the system used for tracer injection. An auto injector (Waters 717 Auto Sampler) was used in the system and connected with the HPLC pump (Waters 600E Multisolvent Delivery System) and the tested column. A spectrometer (Spectronic 20D+, Thermo Scientific) was used as a detector.

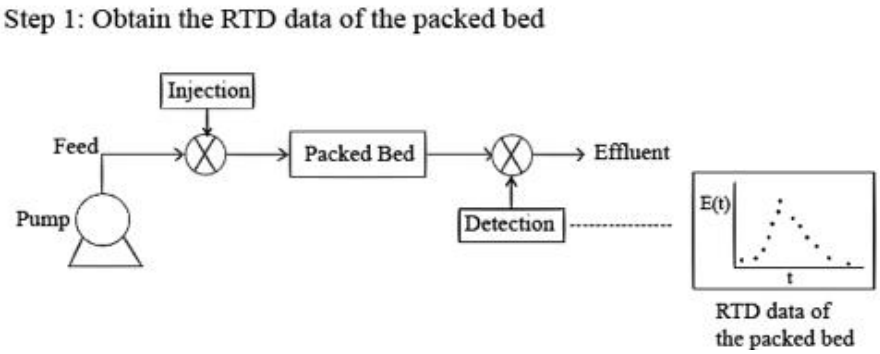

Figure 2–1: The test system for tracer injection

Deionized water was pumped into the column at a constant flow rate controlled by the HPLC pump. A dye Sulforhodamine B (SRB) was used as the indicator and injected into the deionized water stream, as it is one of the most widely used tracing dyes in hydrology to determine flow velocities of the surface and ground water systems. It is important that the tracer does not react with or adsorb the packing materials in the column so that it can fully reflect the flow behavior of the column. SRB (structure in Fig 2-2) shows little if any adsorption on both alumina and SiO_2 compared to other fluorescent dyes [95]. The amount of dye solution injected into the stream can be controlled by the auto injector. After injection, the dye in the stream flowed through the column and into the flow through cell, which recorded and sent the raw data of absorbance to the computer. The absorbance was recorded every 0.2 second by the software Peak Simple (SRI Inc.).

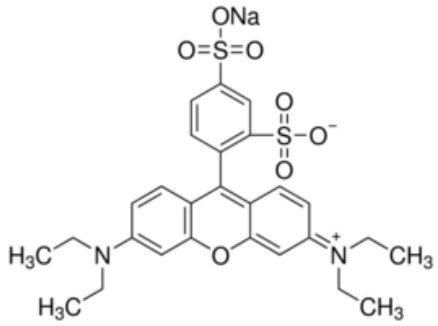

Figure 2–2: Chemical structure of Sulforhodamine B

A calibration curve was established by injecting solutions of known concentration directly into the detector cell and measuring their absorbance. The 11 packed columns in Table 2-1 and an empty column were tested at a flow rate of 0.2 mL/min with a run time of 20 minutes. A volume of 10 microlitres of a solution containing 125 mg/L SRB was injected by the autosampler and the

absorbance read over time. The detector's response was converted into a concentration C(t) curve and then into a distribution function E(t) using equation 3. Three repeat injections were done per column and the results further analyzed in section 4 of this work.

3. Results – binding agent

3.1 Binder solubility in ethanol

3.1.1 The binder SiO_2

The solubility of SiO_2 in different amounts of ethanol was determined and the results shown in Tables 3-1 and 3-2. No precipitates were observed for the all the SiO_2 concentrations studied. SiO_2 was found to be completely soluble in all ethanol solutions.

Table 3–1: Precipitates of the SiO_2 binder (higher concentration) in different content of ethanol

Sample	1	2	3	4	5
SiO_2 binder 40% w/w (g)	9				
Ethanol (g)	1	2.25	3.86	6	9
Ethanol Content (wt%)	10%	20%	30%	40%	50%
Binder Content (wt%)	36%	32%	27.99%	24%	20%
Precipitates (g)	0	0	0	0	0

Table 3–2: Precipitates of the SiO_2 binder (lower concentration) in different content of ethanol

Sample	1	2	3	4	5
SiO_2 40% w/w (g)	4				
Deionized water (g)	5				
Ethanol (g)	1	2.25	3.86	6	9
Ethanol Content (wt%)	10%	20%	30%	40%	50%
Binder Content (wt%)	16%	14.22%	12.44%	10.67%	8.89%
Precipitates (g)	0	0	0	0	0

3.1.2 The binder $AlH_6O_{12}P_3$

Two sets of experiments were performed to determine the solubility of $AlH_6O_{12}P_3$ in ethanol at low and high binder concentrations. Table 3-3 shows the content of each compound in the solution where the binder concentration is relatively high (from 25% to 45 wt%). Nine grams (9 g) $AlH_6O_{12}P_3$ (50% w/w) were mixed with different amounts of ethanol (99%). The total content of ethanol in the overall solution was kept at 10, 20, 30, 40 and 50 wt% to determine when the precipitation would occur and compare the weight of precipitates of each sample. The ratio of the moles of water/ethanol was also calculated and shown in the table.

Table 3–3: Precipitates of the $AlH_6O_{12}P_3$ binder (higher concentration) in different content of ethanol

Sample	1	2	3	4	5
$AlH_6O_{12}P_3$ binder 50% w/w (g)	9				
Ethanol (g)	1	2.25	3.86	6	9
Binder Content (wt%)	45%	40%	34.99%	30%	25%
Ethanol Content (wt%)	10%	20%	30%	40%	50%
Precipitates (g)	0	0	0.9080	3.6745	4.7090
Moles water/ethanol	8	3.5556	2.0725	1.3333	0.8889

Table 3-4 presents the precipitates of each sample in which the binder content was lower (11.1% to 20 wt%). Ethanol content was still kept at 10, 20, 30, 40 and 50 wt%.

Table 3–4: Precipitates of the $AlH_6O_{12}P_3$ binder (lower concentration) in different content of ethanol

Sample	1	2	3	4	5
$AlH_6O_{12}P_3$ binder 50% w/w (g)	4				
Deionized water (g)	5				
Ethanol (g)	1	2.25	3.86	6	9
Ethanol Content (wt%)	10%	20%	30%	40%	50%
Binder Content (wt%)	20%	17.78%	15.55%	13.33%	11.11%
Precipitates (g)	0	0	0.1887	1.1378	1.9875
Moles water/ethanol	12.4444	5.5309	3.2229	2.0740	1.3827

The curves of the precipitate measured for all samples are displayed in Fig 3-1. In 10% and 20 wt% ethanol, the $AlH_6O_{12}P_3$ binder was completely soluble and no precipitate was observed for samples at higher and lower concentration. With the increase of ethanol content, the binder started to precipitate and a white solid was seen at bottom of the centrifuge tube.

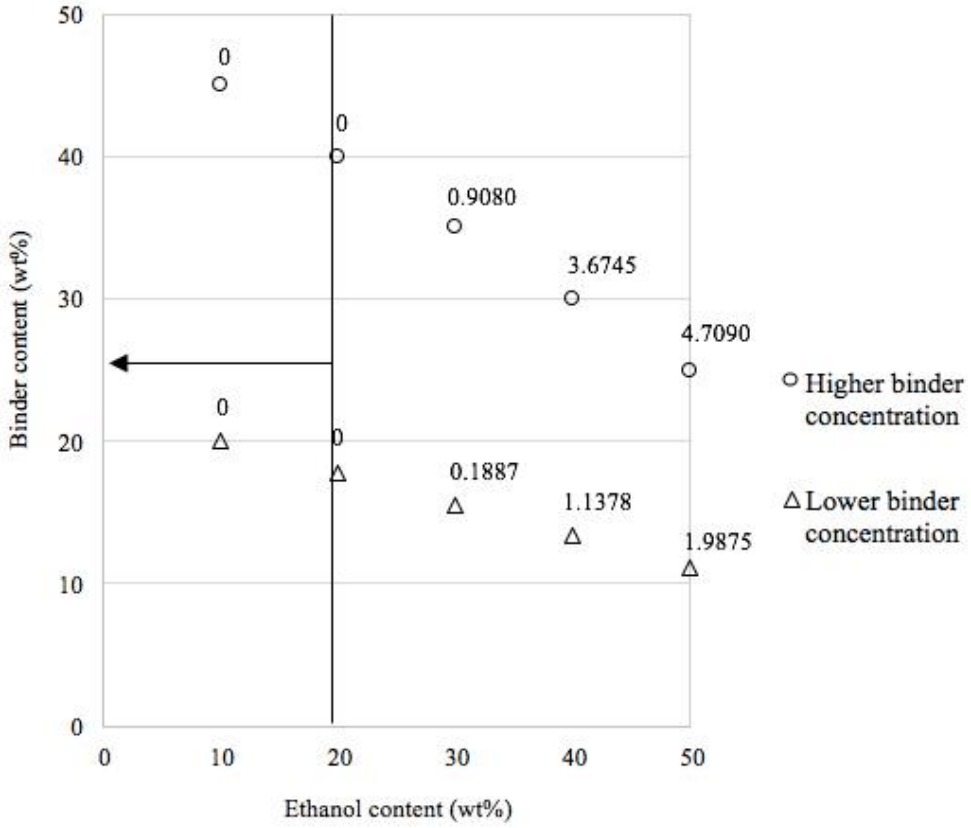

Figure 3–1: Precipitates of $AlH_6O_{12}P_3$ in ethanol at higher and lower concentration. Labels on data points are the weight of precipitates.

Though it can be clearly seen from Fig 3-1 that no precipitates appear when the ethanol content is lower than 20%, the critical point where the precipitation phenomenon starts still remains to be explored. Thus, the relation between moles of water/ ethanol and the precipitates for the solutions in Tables 3-3 and 3-4 is displayed in Fig 3-2.

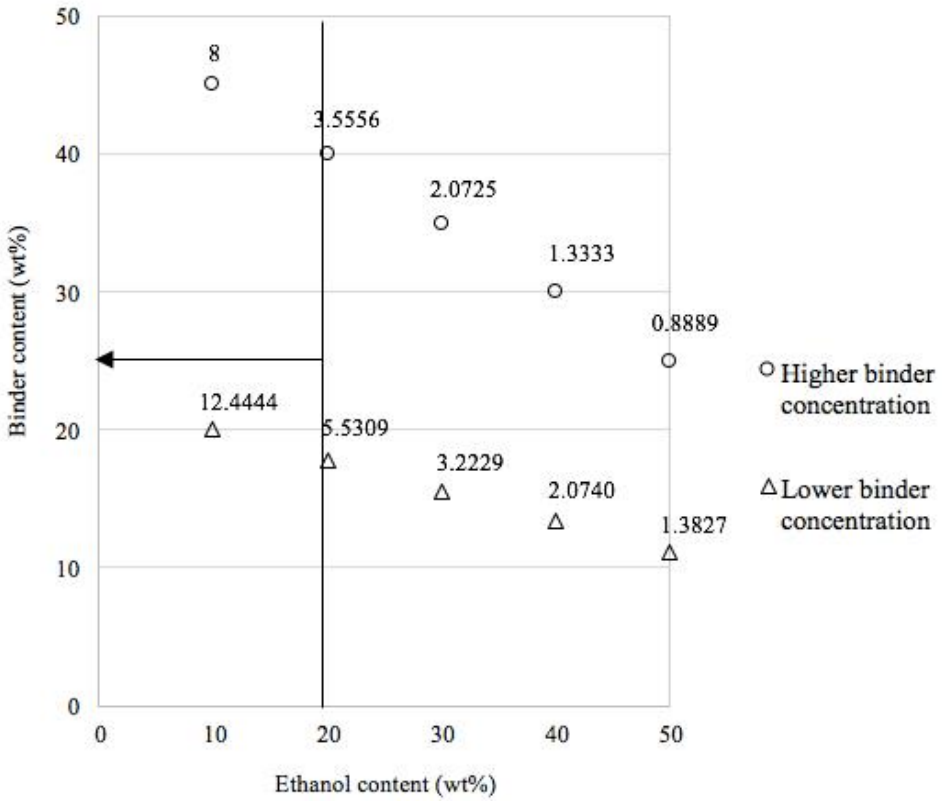

Figure 3–2: Precipitates of $AlH_6O_{12}P_3$ at different mole of water/ethanol. Labels on data points are the ratio of the (mole of water)/(mole of ethanol) in the mixture.

For both samples that were made with higher and lower binder concentration, the precipitation starts at an almost similar mole ratio of water/ethanol. When this ratio is higher than about 3.5, the $AlH_6O_{12}P_3$ binder can be completely dissolved in the solution, however, a certain amount of the binder will precipitate when the ratio is lower than 3.5. To achieve binding while keeping an open porous TAN network, it is critical that the binder be totally dissolved in the solution. As ethanol can decrease the solvent power of the mixture, a high ratio of water/ ethanol can be used to avoid such phenomenon.

3.2 Preliminary studies: Binding of TAN without ethanol

Initial experiments were performed using the binder solutions diluted with water. No ethanol was used in these preparations, as the objective was to find the optimal binder content based on SEM micrographs.

3.2.1 Use of SiO_2 as a binder

To determine the best amount of SiO_2 binder that does not cause too much accumulation in the TAN support, several trials were carried out with different content of binder. The contents of all samples are listed in Table 3-5. All concentrations caused the hardening of the particles as determined by the simple compaction of the particles with a spatula.

Table 3–5: The contents of binder solution

Sample	1	2	3	4	5	6	7
Binder SiO_2 sol (g)	12.5	25	37.5	50	75	100	125
Deionized water (g)	187.5	175	162.5	150	125	100	75
Total weight (g)	200						
Binder Content (wt%)	2.5%	5%	7.5%	10%	15%	20%	25%

SEM images (Fig 3-3) were taken for reinforced supports prepared by the method described above using the conditions listed in Table 3-5. It can be seen that a SiO_2 content that is higher than 20% results in the filling of the entire structure and loss of porosity. While 2.5% to 15% SiO_2 retain the original twinned 3D morphology. However, small spherical aggregates appear in all images between 2.5 and 15% binder content. Although the structure of the TAN was maintained, these aggregates would cause pore blocking. When water alone was used in the

dispersing liquid, all concentrations of SiO_2 caused the accumulation of particulates that could cause pore blocking.

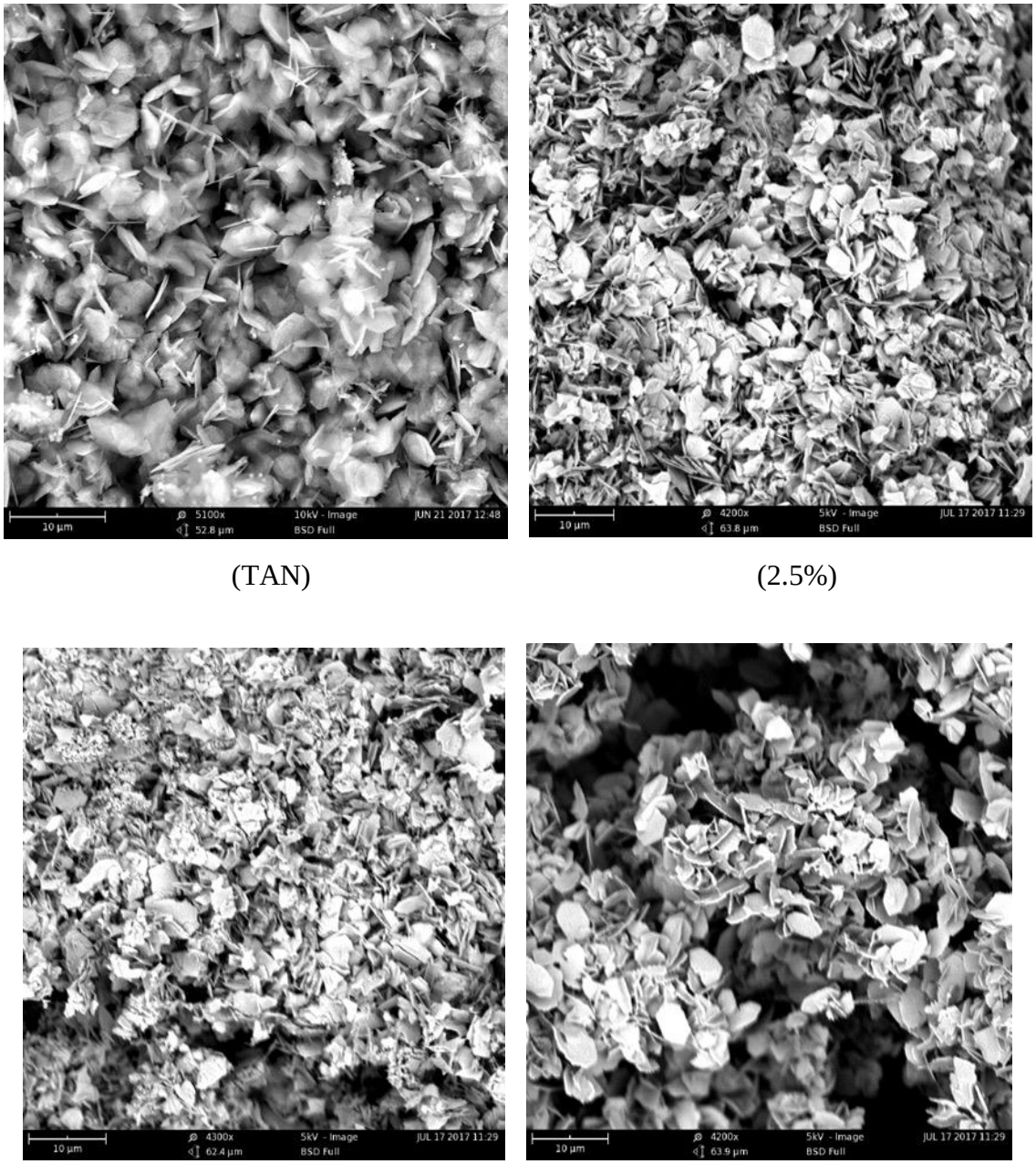

(TAN) (2.5%)

(5%) (7.5%)

Figure 3–3: SEM images showing particle structure at 10 µm of TAN binding with 0, 2.5, 5, 7.5, 10,15, 20 and 25 wt% SiO_2.

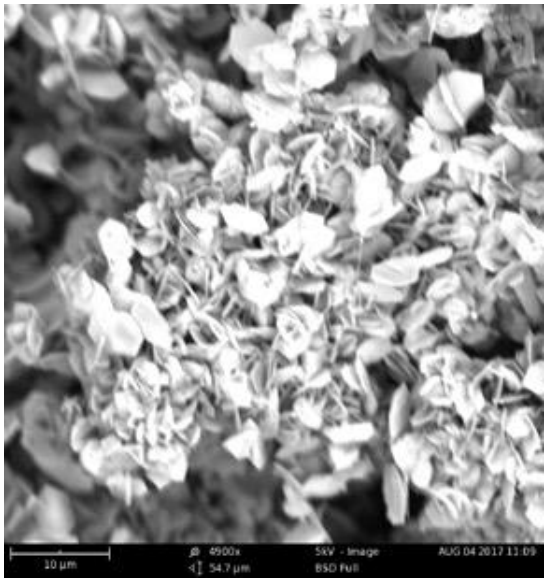

(10%)

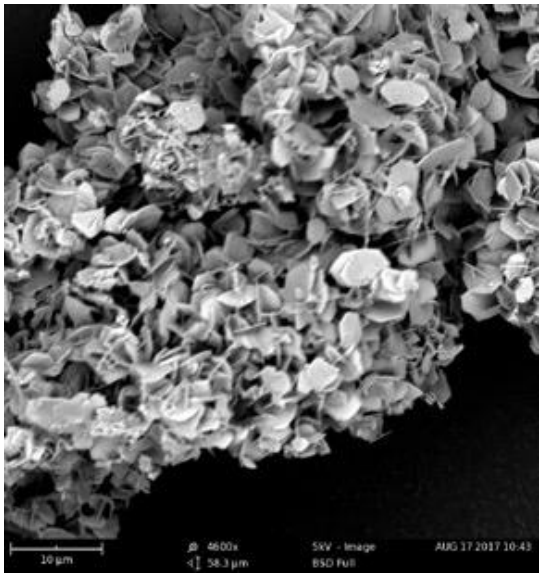

(15%)

(20%)

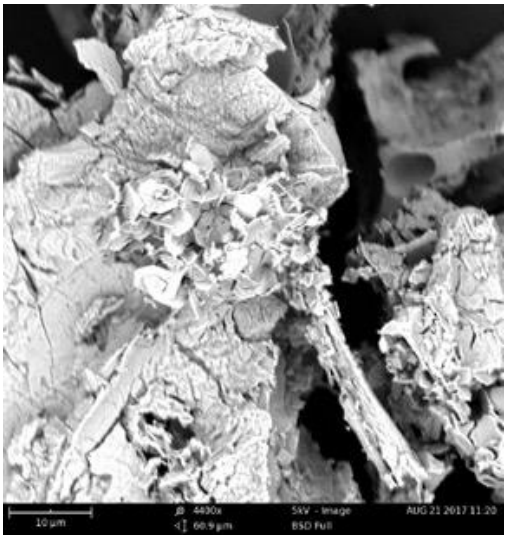

(25%)

Figure 3–3 (continued): SEM images showing particle structure at 10 μm of TAN binding with 0, 2.5, 5, 7.5, 10,15, 20 and 25 wt% SiO_2.

3.2.2 Use of $AlH_6O_{12}P_3$ as a binder

To figure out the amount of binder at which it has the best binding performance on TAN, several trials were carried out with different content of binder. Details are in Table 3-6.

Table 3–6: The contents of binder solution

Sample	1	2	3	4	5	6	7	8
Binder $AlH_6O_{12}P_3$ (g)	10	20	30	40	80	120	160	200
Deionized water (g)	190	180	170	160	120	80	40	0
Total weight (g)	200							
Binder Content (wt%)	2.5%	5%	7.5	10%	20%	30%	40%	50%

Solutions containing 2.5 to 50 wt% binder were made without ethanol and contacted with TAN. Samples prepared with different contents of binder were analyzed and the SEM images are as shown in Fig 3-4.

(TAN)

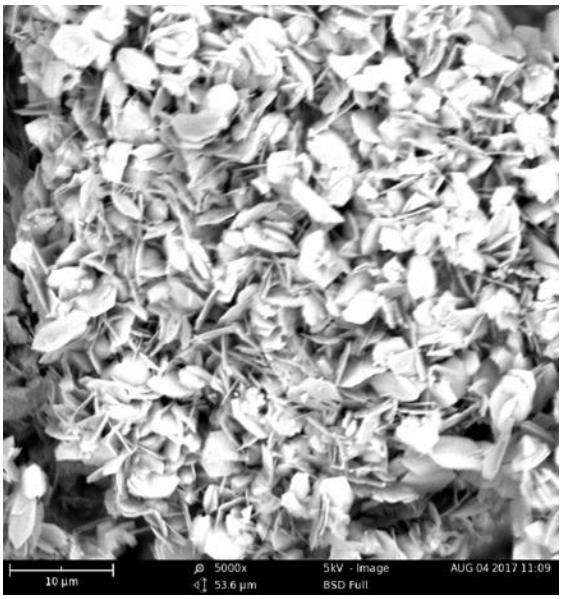

(2.5%)

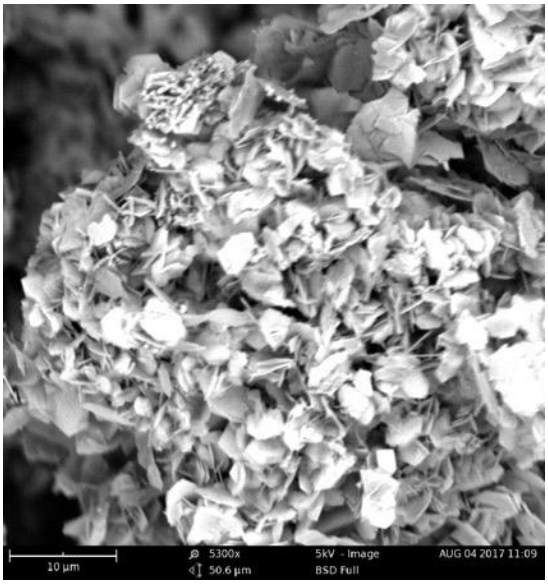

(5%)

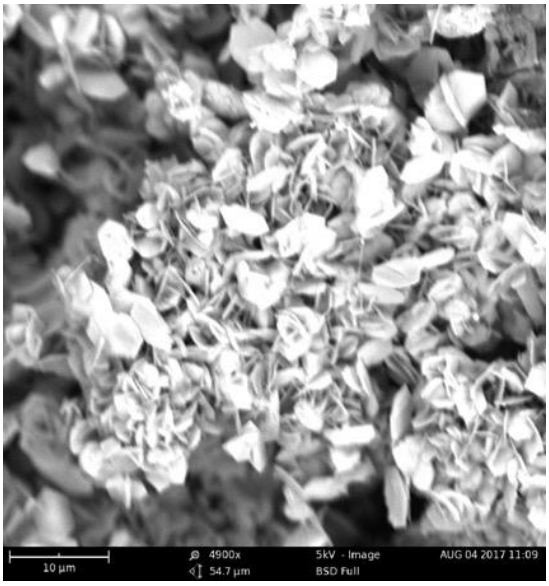

(7.5%)

Figure 3–4: SEM images showing particle structure at 10 µm of TAN binding with 0, 2.5, 5, 7.5, 10, 15, 20, 30 40 and 50 wt% $AlH_6O_{12}P_3$.

(10%)

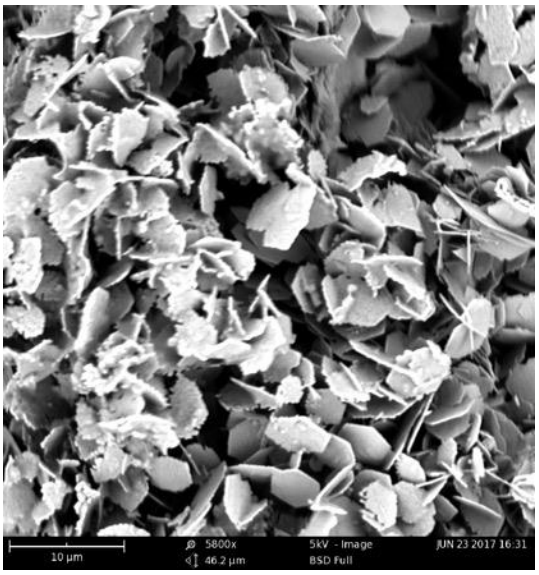

(15%)

(20%)

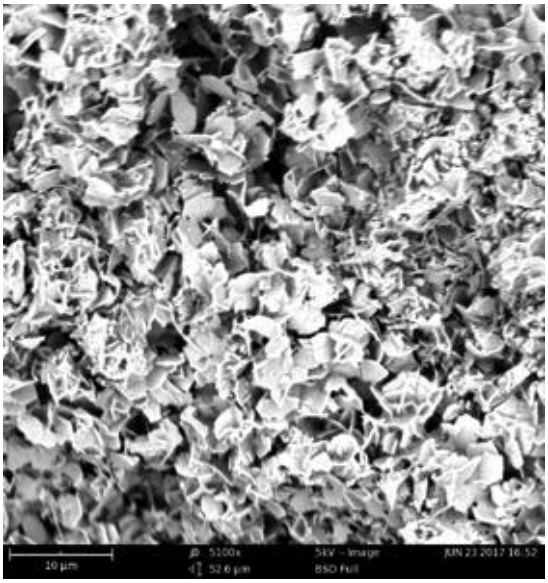

(30%)

Figure 3–4 (continued): SEM images showing particle structure at 10 μm of TAN binding with 0, 2.5, 5, 7.5, 10, 15, 20, 30 40 and 50 wt% $AlH_6O_{12}P_3$.

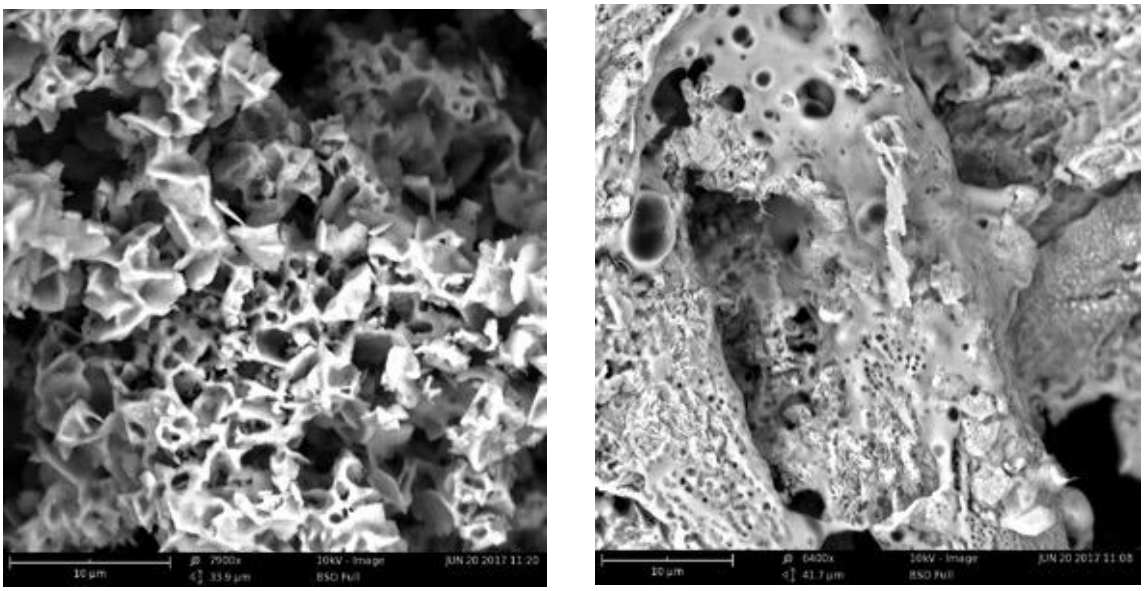

(40%) (50%)

Figure 3–4 (continued): SEM images showing particle structure at 10 μm of TAN binding with 0, 2.5, 5, 7.5, 10, 15, 20, 30 40 and 50 wt% $AlH_6O_{12}P_3$.

When the binder is at relatively low content, the porous and twinned structure of particles is still maintained. Particles with 2.5%, 5% and 7.5 wt% binder show nearly the same characteristics compared to TAN without any binding agents, as the binder content is low. With 10%, 15% and 20 wt% binder, the surfaces of the plate-like particles start getting coated and the edges where particles are attached to each other are slightly melted, indicating the binding effect of $AlH_6O_{12}P_3$. Meanwhile, the 3D structure can still be noticed. At higher binder content, the particles began to react with the $AlH_6O_{12}P_3$, as can be seen from the images of 30%, 40% and 50 wt%, the original structure of TAN is filled in and the particles completely lose their platelet shape when the binder is at 50%. With higher binder content, the pores tend to block due to the reaction between TAN and the $AlH_6O_{12}P_3$ binder. The lack of porosity can be observed in the image of 50% binder.

The bonding mechanism is that of alumina reacting with $AlH_6O_{12}P_3$ to form another compound, which is called reaction bonding, as a chemical reaction is the driving force. Studies have shown that reactions tend towards $AlPO_4$ formation, but there is some controversy about the state of $AlPO_4$ and claiming $Al(PO_3)_3$ phase is an effective bonding phase [79]. Nevertheless, the compound that formed in the reaction is what makes twinned plates attach to each other. Thus, the amount of the binder is important as the objective is to only wet the joints of TAN and make them link to another by the edge. Too much binder will lead to undesired formation of compound resulted from the reaction between alumina and the binder like in the images of 40% and 50 wt%, which should be avoided.

3.3 Binding with TAN with solutions of ethanol

As seen in the previous section, a considerable amount of material was left in the porous network of the TAN particles when water solutions were used in the binding process. Studies on the use of ethanol to decrease the surface tension of the binder solution and permit the removal of excess liquid from the pores of the TAN during the binder deposition process were carried out.

3.3.1 Binding with SiO_2 with solutions of ethanol

A total of 9 samples were produced with SiO_2 binder in solutions containing ethanol. The ability of ethanol to produce TAN supports without surface tension effects encountered in their formation was determined. The contents of 9 samples are listed in Table 3-7. SEM images are shown in Fig 3-5.

Table 3–7: The contents of SiO_2 solution containing different amount of ethanol

Sample	1	2	3	4	5	6	7	8	9
SiO_2 binder (g)	25	50	75	25	50	75	25	50	75
Deionized water (g)	135	110	85	155	130	105	175	150	125
Ethanol (g)	40			20			0		
Total weight (g)	200								
Ethanol Content (wt%)	20%			10%			0%		
Binder Content (wt%)	5%	10%	15%	5%	10%	15%	5%	10%	15%

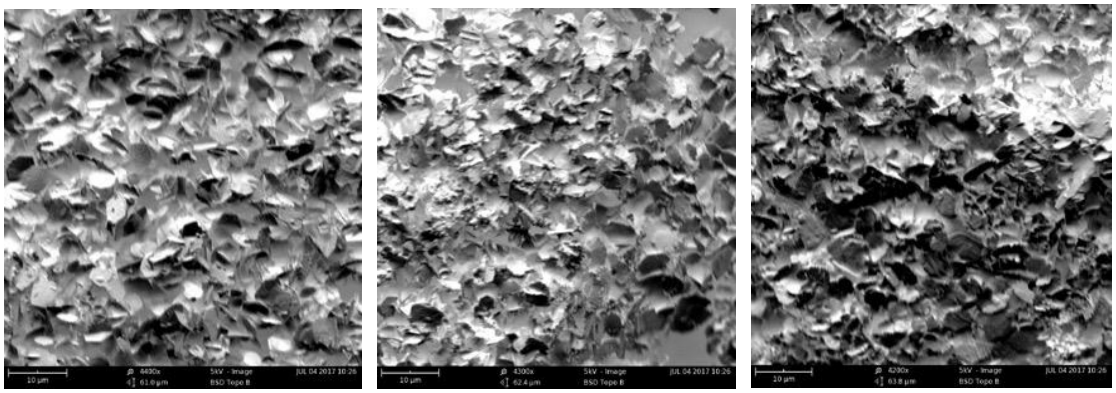

(5% SiO_2, 20% ethanol) (10% SiO_2, 20% ethanol) (15% SiO_2, 20% ethanol)

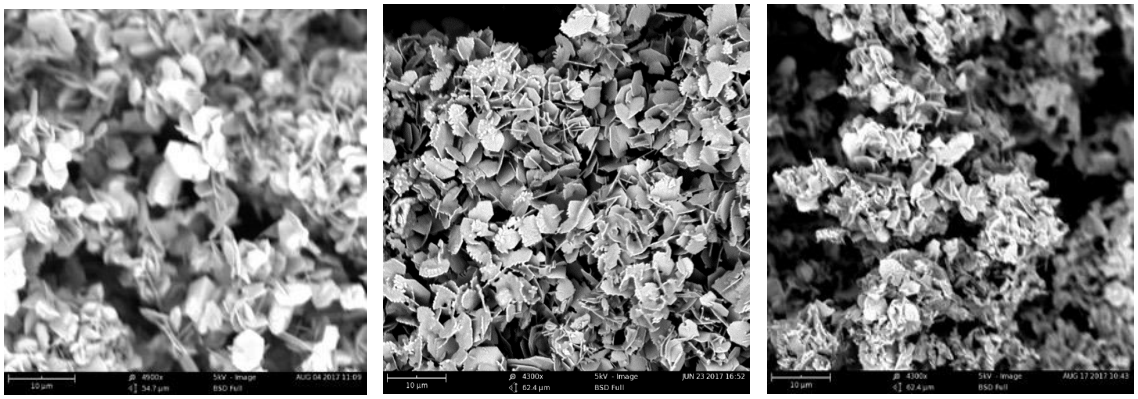

(5% SiO_2, 10% ethanol) (10% SiO_2, 10% ethanol (15% SiO_2, 10% ethanol)

(5% SiO_2, 0% ethanol) (10% SiO_2, 0% ethanol) (15% SiO_2, 0% ethanol)

Figure 3–5: SEM images showing particle structure at 10 μm of TAN binding with 5, 10 and 15 wt% SiO_2 at the presence of 0, 10 and 20 wt% ethanol.

Samples made with 20% ethanol show excess precipitation of SiO_2 while those made with no ethanol have an uneven distribution as some of the SEM images show particle accumulation. Samples made with 10% ethanol were considered preferable based on SEM images.

3.3.2 Binding with $AlH_6O_{12}P_3$

A total of 9 samples were produced with $AlH_6O_{12}P_3$ binder in solutions containing ethanol. The ability of ethanol to remove precipitates from the porous TAN support was determined. The contents of 9 samples are listed in Table 3-8. SEM images are shown in Fig 3-6.

Table 3–8: The contents of $AlH_6O_{12}P_3$ solution containing different amount of ethanol

Sample	1	2	3	4	5	6	7	8	9
$AlH_6O_{12}P_3$ binder (g)	60	80	100	60	80	100	60	80	100
Deionized water (g)	100	80	60	120	100	80	140	120	100
Ethanol (g)	40			20			0		
Total weight (g)	200								
Ethanol Content (wt%)	20%			10%			0%		
Binder Content (wt%)	15%	20%	25%	15%	20%	25%	15%	20%	25%

Among all 9 samples, 1~3 were prepared with a binder solution that has 20% ethanol; 4~6 were with 10% ethanol; 7~9 were with 0% ethanol. The total weight of solution for each sample was 200g. The content of $AlH_6O_{12}P_3$ binder was kept at 15%, 20% and 25 wt%, as the unique 3D structure of TAN collapsed at higher binder content. SEM images of 9 samples are shown in Fig 3-6.

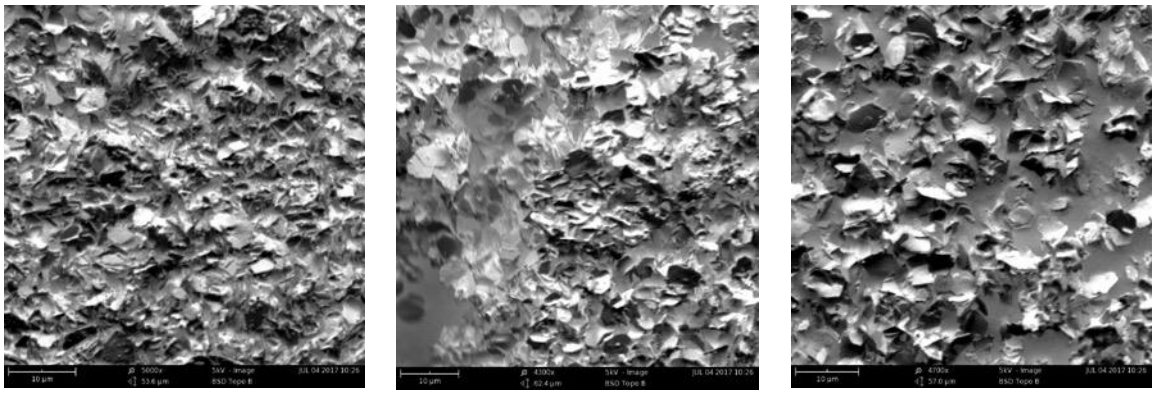

(15% $AlH_6O_{12}P_3$, 20% ethanol) (20% $AlH_6O_{12}P_3$, 20% ethanol) (25% $AlH_6O_{12}P_3$, 20% ethanol)

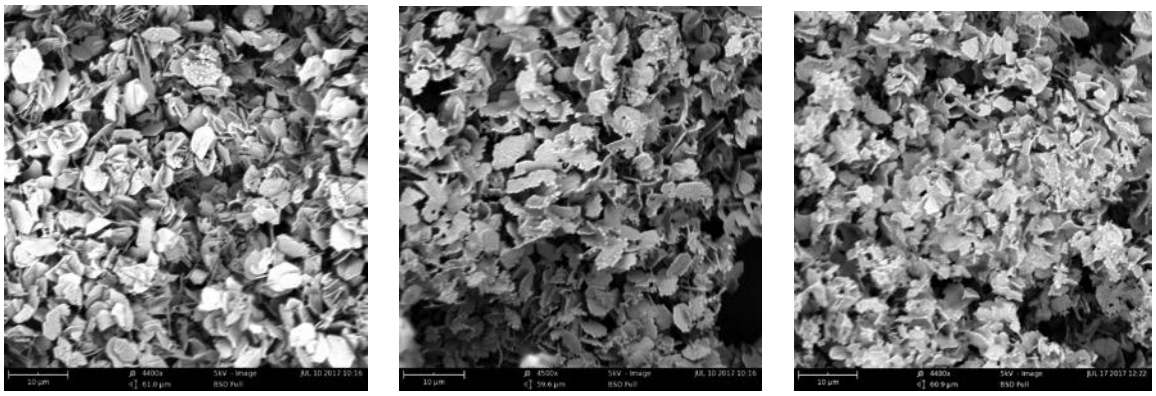

(15% $AlH_6O_{12}P_3$, 10% ethanol) (20% $AlH_6O_{12}P_3$, 10% ethanol) (25% $AlH_6O_{12}P_3$, 10% ethanol)

(15% $AlH_6O_{12}P_3$, 0% ethanol) (20% $AlH_6O_{12}P_3$, 0% ethanol) (25% $AlH_6O_{12}P_3$, 0% ethanol)

Figure 3–6: SEM images showing particle structure at 10 μm of TAN binding with 15, 20 and 25 wt% $AlH_6O_{12}P_3$ at the presence of 0, 10 and 20 wt% ethanol.

When there is no ethanol in the binder solution, images show undesired accumulation in some spots, as can be seen in Figure 3-6, some particles were completely covered while others still retained their original structure. It is caused by the uneven distribution of the binder, so part of the particles is in contact with more binder and the rest with less binder, which leads to the accumulation in some spots.

With ethanol in the solution, the dispersion of particles was improved and it led to better uniformity and much smoother surface. No particle accumulation was observed when 10% ethanol was added. However, as can be seen from images which have 20% ethanol, the particles cannot be observed clearly and they were filled with solid blocking the pores. The particles produced with 10% ethanol had the best results overall.

3.4 Flow studies: Packed column pressure drop

In order to verify whether the presence of binder enhances the strength of TAN, bed compaction test on particles made with different amount of binder was conducted. TAN reinforced with 5, 10, 15, 20 and 25 wt% $AlH_6O_{12}P_3$, and 2.5, 5, 7.5, 10, 15 and 20 wt% SiO_2, in 10 wt% ethanol, were packed in the columns as previously described and tested using the system described in Fig 2-1. These results are shown in Fig 3-7 and Fig 3-8. Columns made with SiO_2 show a near linearly increase in pressure drop with an increase in flow rate. The more SiO_2 added to the particles, the higher pressure drop it presents, meaning the packing shows a satisfactory strength to the flow. For columns containing $AlH_6O_{12}P_3$ binder, the pressure drop moves up linearly with the increase in flow rate initially. But when flow rate keeps increasing, the pressure drop presents a sudden rise. This can be observed in Fig 3-8, the curves of the columns made with $AlH_6O_{12}P_3$

binder all start to bend after remaining linear for a while, indicating the collapse of the packing. The network of these particles is mechanically weak and cannot maintain its integrity under flow. It can be concluded that SiO_2 brought greater enhancement in particle structure than $AlH_6O_{12}P_3$. Higher amount of binder also results in higher pore blockage, as TAN with 20% and 15 wt% SiO_2 shows the highest pressure drops, which rise to a high value at a very low flow rate. The $AlH_6O_{12}P_3$ binder does not enhance the structure of TAN as remarkably as SiO_2 does, higher $AlH_6O_{12}P_3$ content still shows relatively higher pressure drop than particles made with low $AlH_6O_{12}P_3$ concentration, which does not present much compaction and resistance against the flow.

Therefore, SiO_2 binder has a stronger binding performance and exhibits higher strength comparing to $AlH_6O_{12}P_3$ binder. With a relatively low amount, SiO_2 can achieve a prominent enhancement in the structure of TAN. High amounts of binder lead to an incredibly high pressure drop, because excess binder fills the 3D porous structure of the TAN. From Figure 3-7 a concentration above 2.5 wt% will produce an open pore structure that will resist packing up to pressures of 160 psi (11 bar).

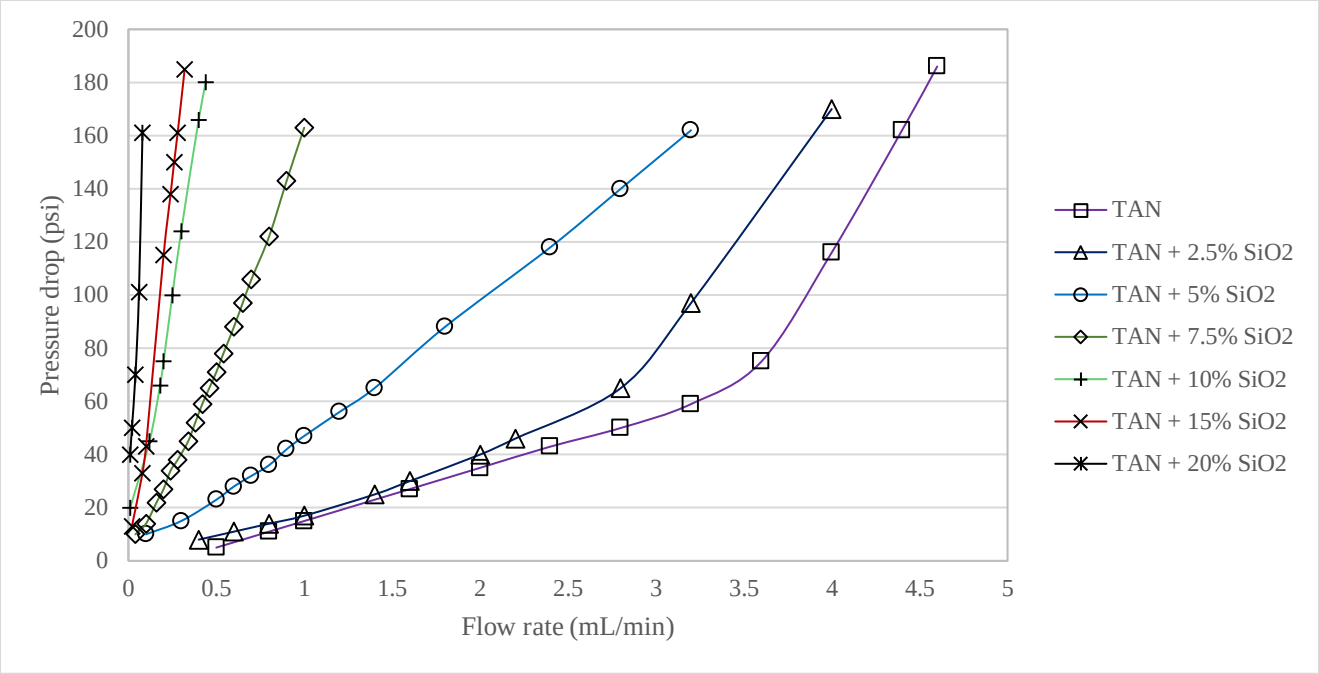

Figure 3–7: Pressure drop in the columns of TAN reinforced by different amount of SiO_2

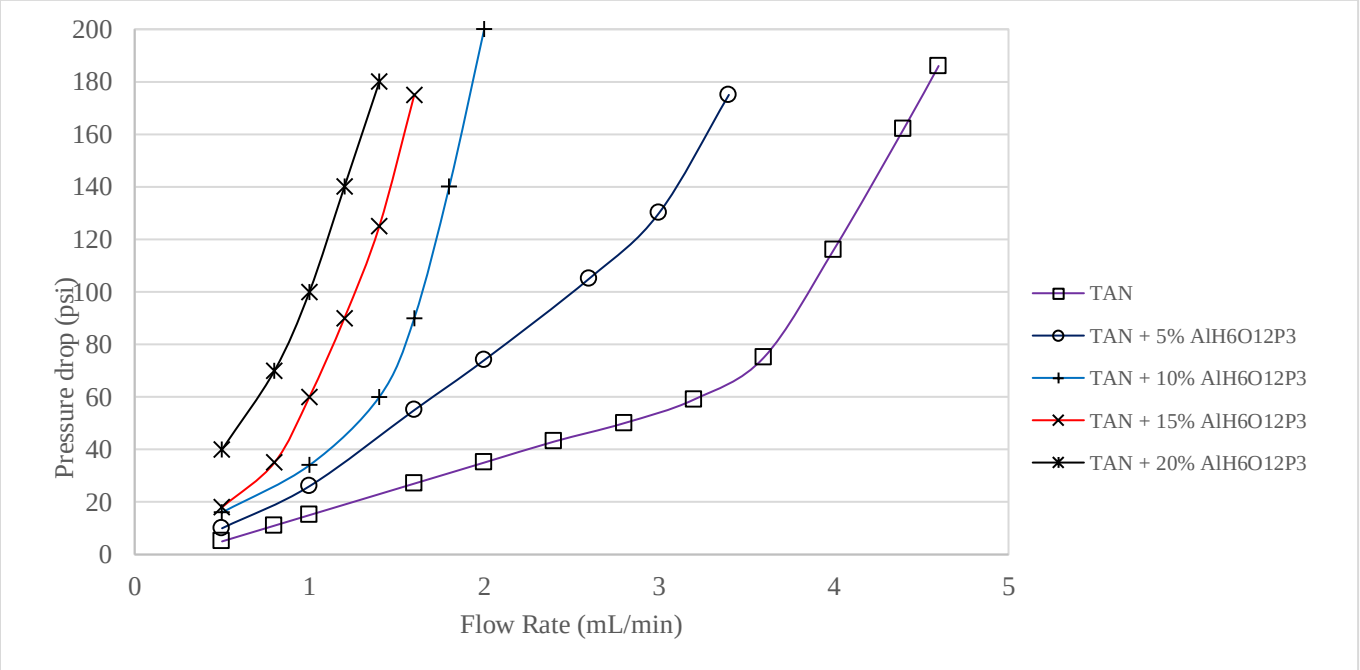

Figure 3–8: Pressure drop in the columns of TAN reinforced by different amount of $AlH_6O_{12}P_3$

The permeability k in Darcy's law was also calculated. Fig 3-9 shows the hydraulic permeability of TAN reinforced by SiO_2 binders and Fig 3-10 shows TAN reinforced by $AlH_6O_{12}P_3$.

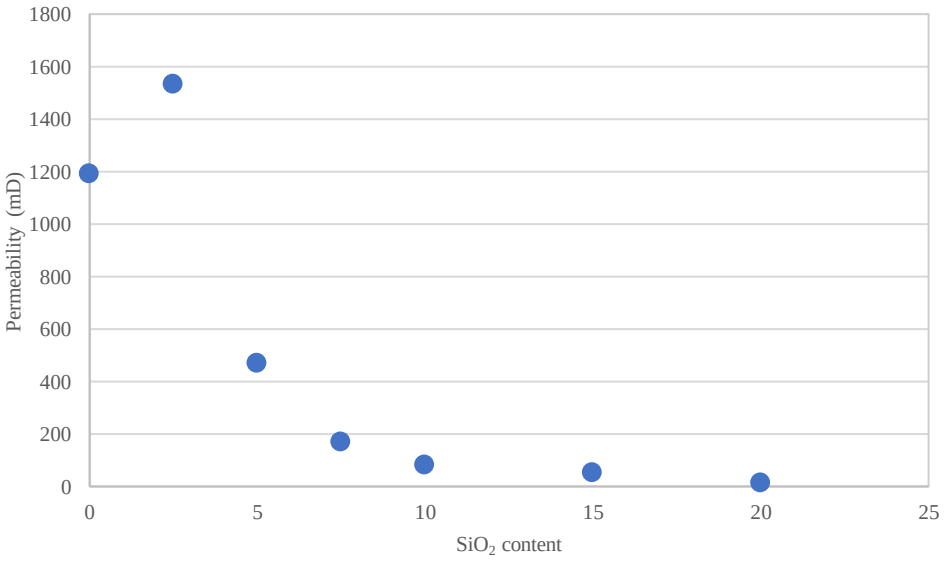

Figure 3–9: Hydraulic permeability of TAN reinforced by SiO_2

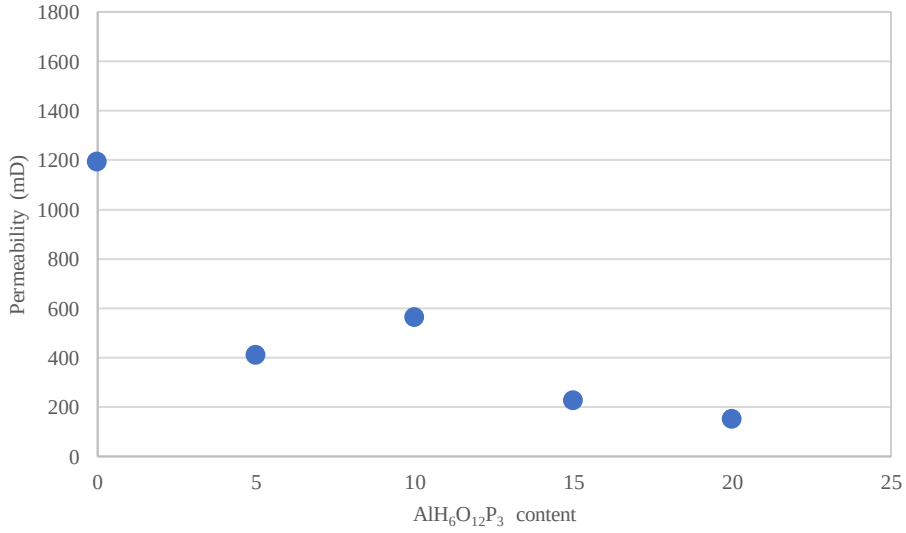

Figure 3–10: Hydraulic permeability of TAN reinforced by $AlH_6O_{12}P_3$

Generally, the permeability decreases with the increase in binder content for both SiO_2 and $AlH_6O_{12}P_3$. TAN without SiO_2 is easily compacted as discussed later in section 4. At very low concentrations of SiO_2 the permeability is expected to increase on increasing SiO_2 concentration then decrease. This is seen in Figure 3-9 where 2.5% SiO_2 shows higher permeability than TAN with 0% SiO_2. The addition in SiO_2 tends to result in lower permeability compared to $AlH_6O_{12}P_3$, indicating SiO_2 plays a more effective role in binding the particles, whereas, particles bound with $AlH_6O_{12}P_3$ are not evenly dispersed and more susceptible to channeling.

4. Results – Residence Time Distribution

The RTD function (E curve) was determined for all 11 columns (TAN reinforced by 5, 10, 15, 20 and 25 wt% $AlH_6O_{12}P_3$, 2.5, 5, 7.5, 10, 15 and 20 wt% SiO_2). The RTD function was studied as detailed in the following sections.

4.1 Correlation of concentration and voltage

As the absorbance measurement generated by the spectrometer is in microvolts, it is desired to establish a correlation between this output and concentration so that the output values for each column can be converted to concentration for further calculation and interpretation. Sulforhodamine B solutions were prepared in several concentrations, injected directly in the spectrometer cell and their corresponding output values recorded. The experiments were conducted in triplicate for several concentrations. The correlation of concentration and voltage was established as:

$$Concentration = exp\left(\frac{\ln \frac{Voltage}{236714}}{0.6267}\right), \tag{13}$$

where concentration is in mg/L and voltage is in microvolts. The correlation factor for this equation is $R^2 = 0.98899$. With this equation, the output curve in microvolts generated by the spectrometer can be converted to the concentration curve.

4.2 Transforming the output curve to an RTD function

All columns were tested at a flow rate of 0.2 mL/min, to avoid compaction in all columns would they not be mechanically strong enough to resist the flow. This would decrease the length of the packing and damage the structure of the packing materials.

The data generated when no column was connected to the system, and the data of an empty column was investigated. They were abbreviated as “no column” and “empty column” for comparison with other columns in Fig 4-1. The RTD function E(t) was calculated by using Eq 1 to 10. A sample calculation can be found in the Appendix.

4.2.1 Columns with SiO_2 binder

Fig 4-1 shows the RTD function of columns packed with lower SiO_2 bound TAN. The 3 columns with 2.5, 5 and 7.5 wt% SiO_2 have very similar RTD function. Their function starts at about 200 second and falls down at almost the same time. The function of the no column starts earliest among all, as it is the shortest so it takes less time for the tracing dye to exit. Empty column being the second, there are no packing materials for the fluid to pass through, thus there is less resistance to the flow. The column of TAN exhibits nearly the same function as empty column, because the non-strengthened TAN is fragile and unable to resist even a flow with a very small velocity.

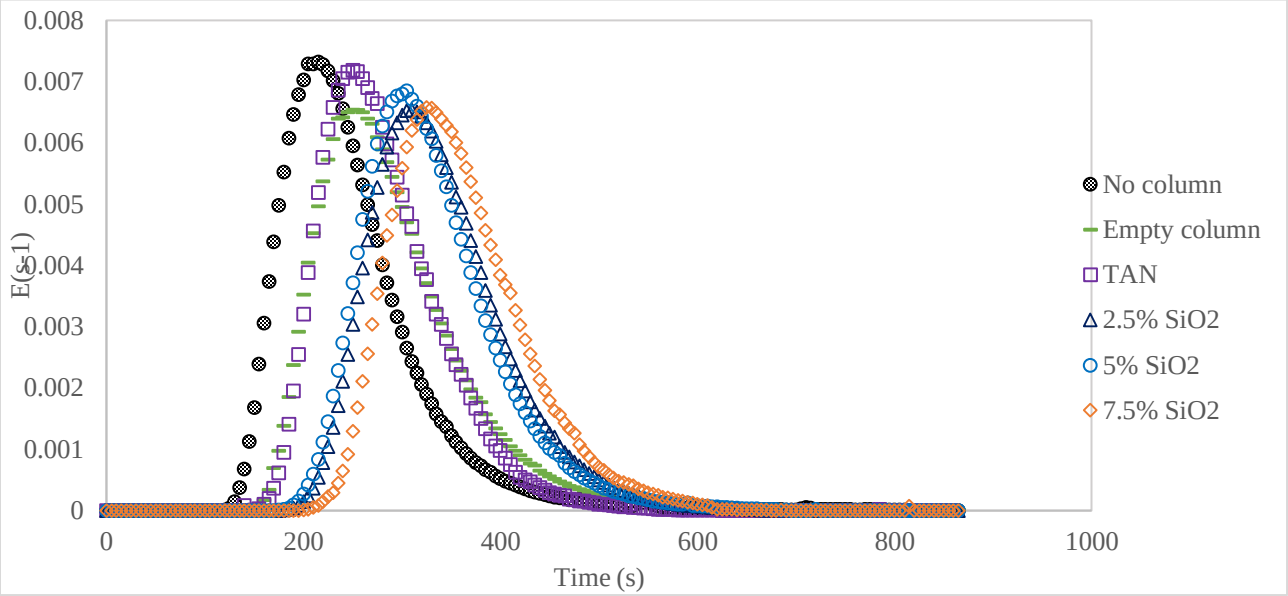

Figure 4–1:Experimental RTD data of columns with lower SiO_2 content.

The reinforced TAN particles were immediately compacted when they were in contact with the flow and the original length of packing was greatly shortened, as shown in Fig 4-2. A large void volume was observed in the TAN column. This void volume acted as an empty column. The length of packing in the columns of 2.5, 5 and 7.5 wt% SiO_2 still remained the same, as the particles were reinforced and were able to resist the flow at the current velocity.

(a) Before test (b) After test

Figure 4–2: The length of packing before and after the test

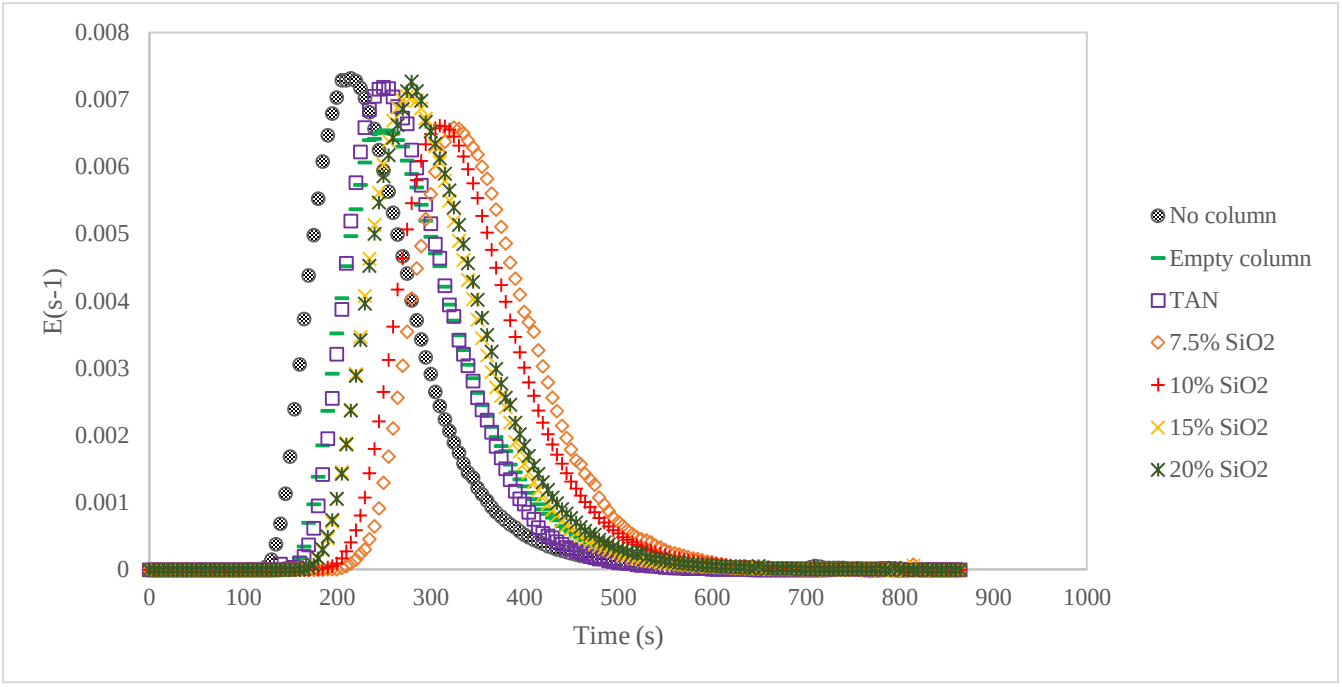

Figure 4–3: Experimental RTD data of columns with higher SiO_2 content

In Fig 4-3 the RTD function of columns packed with TAN bound with higher SiO_2 content is shown, it can be noticed that columns with 7.5% and 10 % SiO_2 are similar; 10% and 15% SiO_2

are also similar to each other. The function of the two columns with 10% and 15% SiO_2 starts earlier than those with 7.5% and 10 % SiO_2, as the higher binder content filled the twinned 3D isoporous structure and caused the individual particles to bind together and form into aggregates. The fluid tended to pass across the void area among the aggregates in the column instead of through the particles. This can be better understood with the illustration of two different flow patterns in Fig 4-4. Fig 4-4 (a) has an ideal packing of twinned nano-plates, its isoporous property enables the fluid to flow through in many possible directions; while Fig. 4.4 (b) has no isoporous structure and the particles are clumped in aggregates, so the fluid tends to follow the path of the voids in the column. Thus, columns with 10% and 15% SiO_2 show higher tendency towards the behavior of an empty column because the flow inside the column is more likely characterized by (b). The columns of 7.5% and 10 % SiO_2 show behaviors like Fig. 4-4 (a).

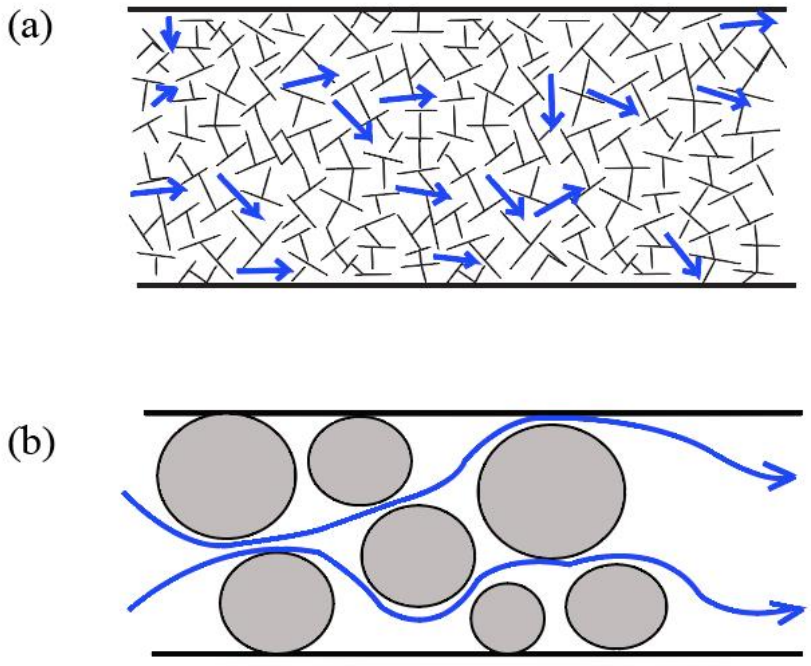

Figure 4–4:Two flow patterns in a packed column. (a): flow in the column with packing materials of isoporous structure; (b): flow in a column with aggregates of particles.

Flow represented by Fig. 4-4 (b) happens when the binder content is too high which blocks the pores and creates accumulation of particles. This should be avoided. The results in Fig 4-3 indicates a SiO_2 content higher than 15% is not desired.

In summary, the column of TAN behaves like an empty column, because the particles are too loose and fragile and can be easily compressed by the flowing fluid. Columns of 15% and 20% SiO_2 were subjected to too much binder material. The flow in these 2 columns tends to pass through the void space between the aggregates in the column. The columns of 2.5, 5, 7.5 and 10% SiO_2 had the best performance.

4.2.2 Columns with $AlH_6O_{12}P_3$

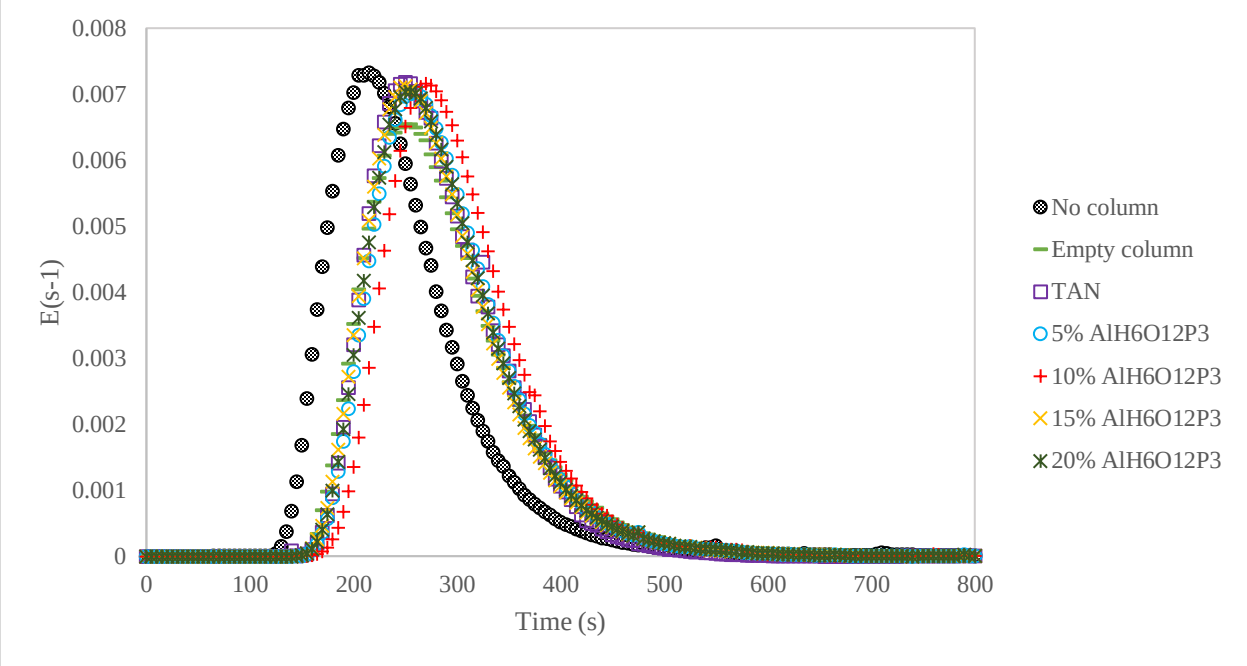

Figure 4–5: Experimental RTD data of columns with $AlH_6O_{12}P_3$

Columns packed with TAN reinforced with different amounts of $AlH_6O_{12}P_3$ are shown in Fig 4-5. The no column case starts the E(t) function earliest among all. The 4 columns with $AlH_6O_{12}P_3$ binder all have a similar RTDs to that of TAN and the empty column and not much difference can be seen from the curves. Like TAN, the length of the 4 columns became shorter and an empty area appeared in the columns after the test. Even a binder content of 20% still fails to bring effective improvement in the strength of the structure.

Compared to the results shown by $AlH_6O_{12}P_3$ binder, SiO_2 presents more effective performance in binding the structure of TAN and it also draws forth the consideration of optimized binder content, as columns with lower and higher SiO_2 contents show different flow patterns, while such situation was not observed in the columns with $AlH_6O_{12}P_3$.

4.3 Applying the dispersion model to the E-curves

In this section, an axial dispersion model was used to fit the experimental RTD data. Axial dispersion models are useful for describing the flow pattern in tubes and are also the most commonly used models to describe packed beds. The model is a two parameter model. The first parameter is the Peclet number. The second parameter is the mean residence time, t_m. The Peclet number reflects the ratio of advection to diffusion. In an ideal plug flow reactor where dispersion is negligible, Pe tends to infinity [96].

The following axial dispersion model described by Gouvêa et al. (1990) was used to model the packed beds:

$$E_\theta(\theta) = \sqrt{\frac{Pe+1}{4\cdot\pi\cdot\theta^3}}\exp\left(\frac{-(Pe+1)\cdot(1-\theta)^2}{4\cdot\theta}\right) \tag{14}$$

Another important data processing step is to remove interferences from the injection and detection system. The RTD data obtained from the tracer injection contains a distorted signal. The injection and detection system may not produce an ideal instantaneous injection pulse. Therefore, it is necessary to take into account the interference caused by the detection system in fitting the axial dispersion model to the experimental data.

Fig 4-6 shows the steps to apply an adjusted model that takes into account of the interference of the testing system and fit the RTD data. The RTD data of the process (packed bed) was generated first (Step 1). Afterwards, the RTD data of the system when no packed column is connected to it was determined in Step 2. The dispersion model and the RTD data of the system (Step 2) were convoluted to predict a response for the combined system and packed bed (Step 3). The convolution is a mathematical operation between two signals to produce a third signal that can be viewed as a cross-correlation product. The model parameters are adjusted until the predicted signal obtained by convolution is the same as that of the experimental signal measured in Step 1.

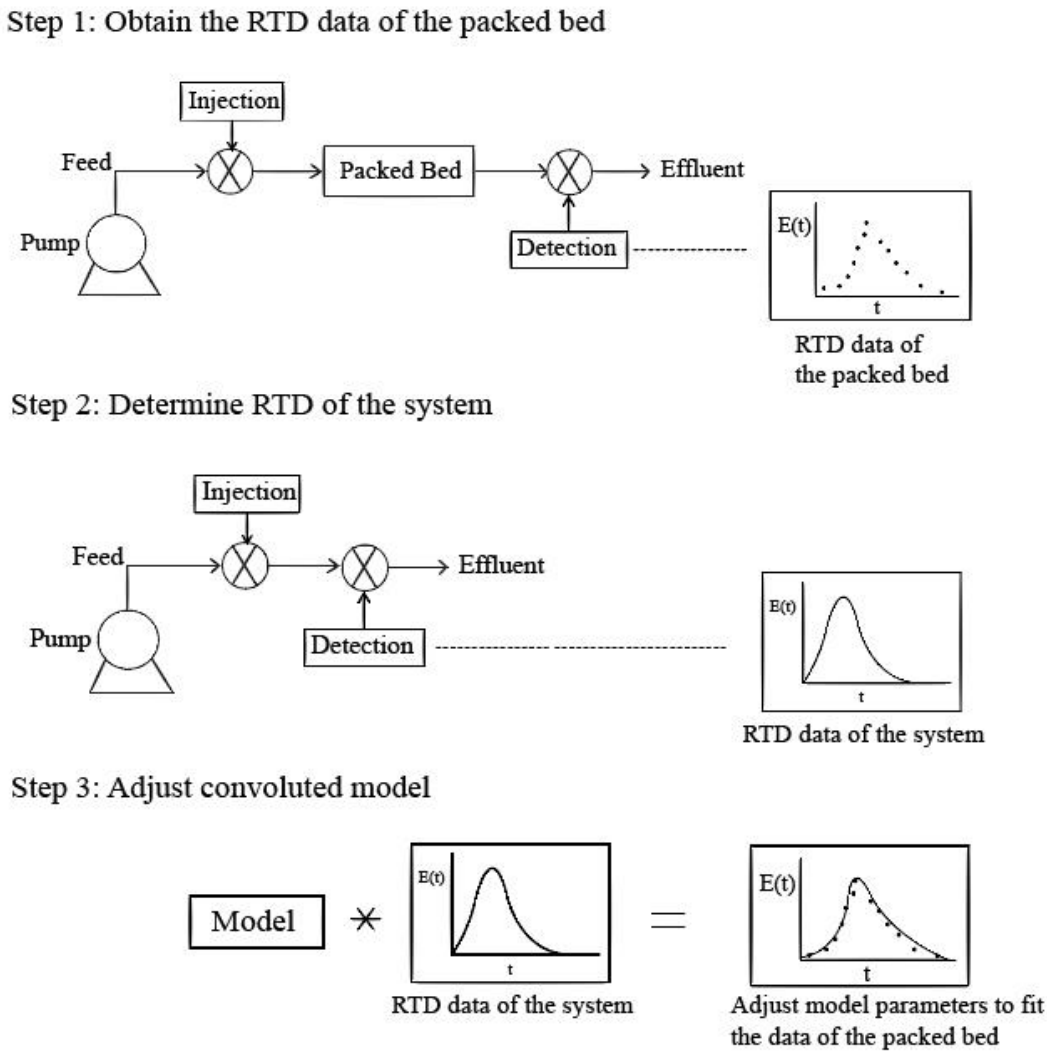

Figure 4–6: Steps to fit the model to RTD data and considering the signal distortion of the system

Details of this method are included in Gutierrez et al (2010) [96]. The input signal (C_{in}, Fig 4-6 Step 2) is modified into an output signal (C_{out}, Step 3). The E function represents the dispersion model. The convolution integral is evaluated as follows:

$$C_{out}(t) = \int_0^t C_{in}(t - t') \cdot E(t')dt' \tag{15}$$

When the input and output signals are known, the E function can be calculated. The convolution integral can be discretized in the time domain as follows (Levenspiel, O., 1999),

$$C_{out}(t_i) = \Delta t \cdot \sum_{j=1}^{i=1} C_{in}(t_{i-j}) \cdot E(t_j) \tag{16}$$

where t_i and t_j are discrete time instants and Δt is the length of time step.

The convolution can be achieved by the procedure provided in Table 4-1.

Table 4–1: Numeric determination of the output signal using discrete convolution.

C_{out}	j=1	j=2	j=3	j=4	j=5
$C_{out}(t_1)/\Delta t$	0				
$C_{out}(t_2)/\Delta t$	$C_{in}(t_1) \cdot E(t_1)$ +	0			
$C_{out}(t_3)/\Delta t$	$C_{in}(t_2) \cdot E(t_1)$ +	$C_{in}(t_1) \cdot E(t_2)$ +	0		
$C_{out}(t_4)/\Delta t$	$C_{in}(t_3) \cdot E(t_1)$ +	$C_{in}(t_2) \cdot E(t_2)$ +	$C_{in}(t_1) \cdot E(t_3)$ +	0	
$C_{out}(t_5)/\Delta t$	$C_{in}(t_4) \cdot E(t_1)$ +	$C_{in}(t_3) \cdot E(t_2)$ +	$C_{in}(t_2) \cdot E(t_3)$ +	$C_{in}(t_1) \cdot E(t_4)$ +	0
$C_{out}(t_6)/\Delta t$	$C_{in}(t_5) \cdot E(t_1)$ +	$C_{in}(t_4) \cdot E(t_2)$ +	$C_{in}(t_3) \cdot E(t_3)$ +	…	…
$C_{out}(t_7)/\Delta t$	$C_{in}(t_6) \cdot E(t_1)$ +	$C_{in}(t_5) \cdot E(t_2)$ +	…	…	…
$C_{out}(t_8)/\Delta t$	$C_{in}(t_7) \cdot E(t_1)$ +	…	…	…	…
…	…	…	…	…	…

The axial dispersion model used is shown in Eq 14. The convolution in Table 4-1 was constructed using Microsoft Excel and the Solver of Excel was used to find the solution by varying the parameter Pe in the axial dispersion model and the mean residence time t_m of the process. In order to find the best fit, the sum of squared errors (SSE) in Eq 17 was used. By minimizing SSE between the experimental RTD data in Step 1 and predicted convoluted RTD

data in Step 3, solver in excel was used to find the solution that fits the model best to give the parameters Pe and t_m in the axial dispersion model.

$$SSE = \sum_{i}^{m} (E_{\exp}(t_i) - E_{conv}(t_i))^2 \quad (17)$$

This technique was used to determine the E curve, Pe and t_m of all of the columns as discussed in the next sections.

4.3.1 Columns with SiO_2

The dimensionless E(θ) function applied with the axial dispersion model was used to compare the flow performance of all columns. E(θ) is a normalized RTD function and the quantity θ represents the number of reactor volumes of fluid based on entrance conditions that have flowed through the reactor in time t. The purpose of establishing this normalized function is that the flow behavior inside reactors of different sizes can be compared directly.

Fig 4-7 illustrates E(θ) function at different level of dispersion. The ideal plug flow will tend to be very close to a pulse at θ=1 and Pe tends to be ∞, as there is no dispersion. E(θ) will also tend to approach the ideal plug flow behavior if the dispersion is small. If there is a large dispersion in the column, the flow behavior will deviate from plug flow and move to the left with a long and skewed tail. When Pe tends to 0, the dispersion is maximal. Thus, the axial dispersion model can simulate different types of behaviors between PBR (no back mixing) and CSTR (complete back mixing) [96].

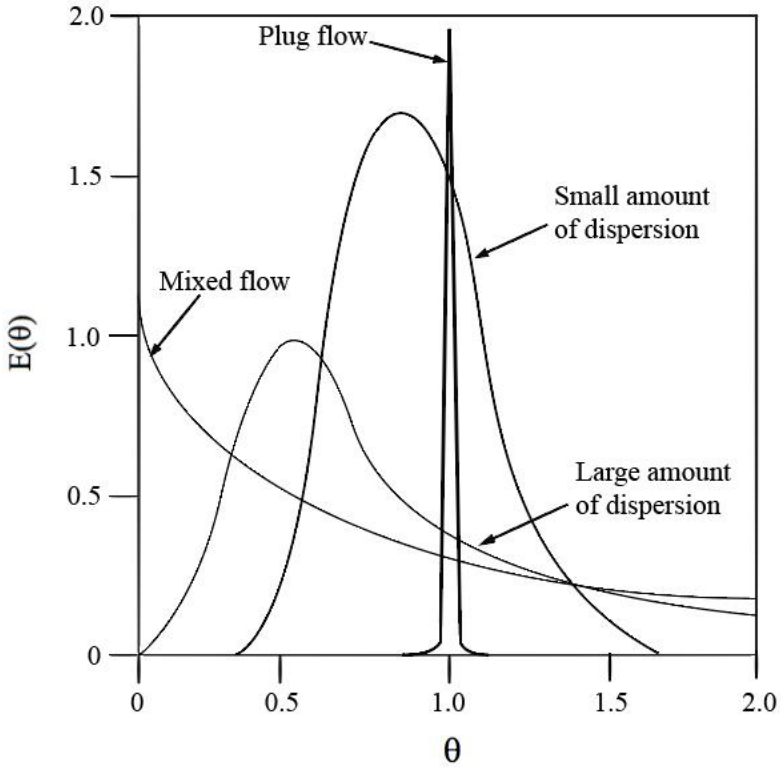

Figure 4–7: Results of E(θ) at different level of dispersion

The E(θ) function of columns with a lower SiO_2 content are presented in Fig 4-8.

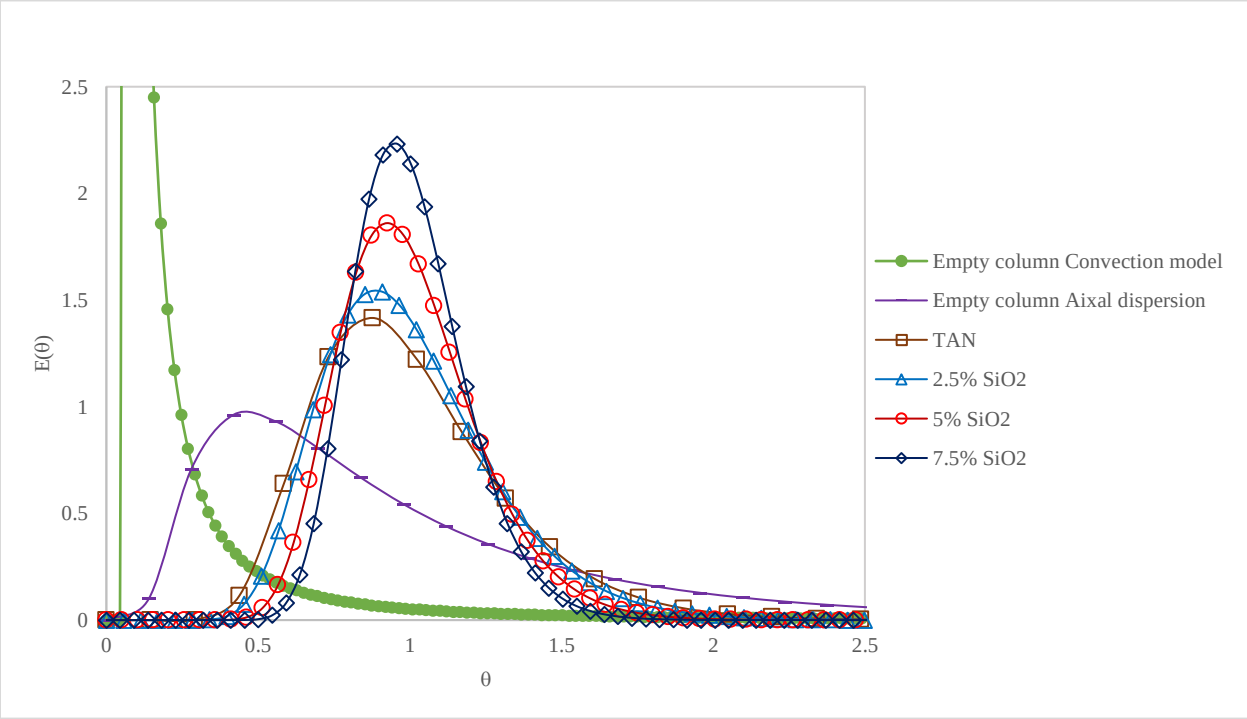

Figure 4–8: E(θ) function of columns reinforced by a lower amount of SiO_2. .Using the "no column" data in the convolution model.

Among all columns, the empty column deviates the most from the ideal plug flow behavior. The column of TAN performs better than the empty column as it moves towards the ideal plug flow behavior prominently. With the increase in SiO_2 content, it is very clear that E(θ) function moves to the right gradually and approaches the ideal plug flow. Among all tested columns, the column with 7.5% SiO_2 shows the most tendency to plug flow.

The empty column was also modeled using the axial dispersion model in the above comparison. A generalized convection model in Eq 18 was also used to characterize the empty column. The plot of the empty column in two different models and the column of 7.5% SiO_2 is presented in Fig 4-9.

$$E_\theta(\theta) = \frac{1}{1-\theta_0}\frac{1}{\theta}\left(\frac{\theta_0}{\theta}\right)^{\frac{1}{1-\theta_0}} \tag{18}$$

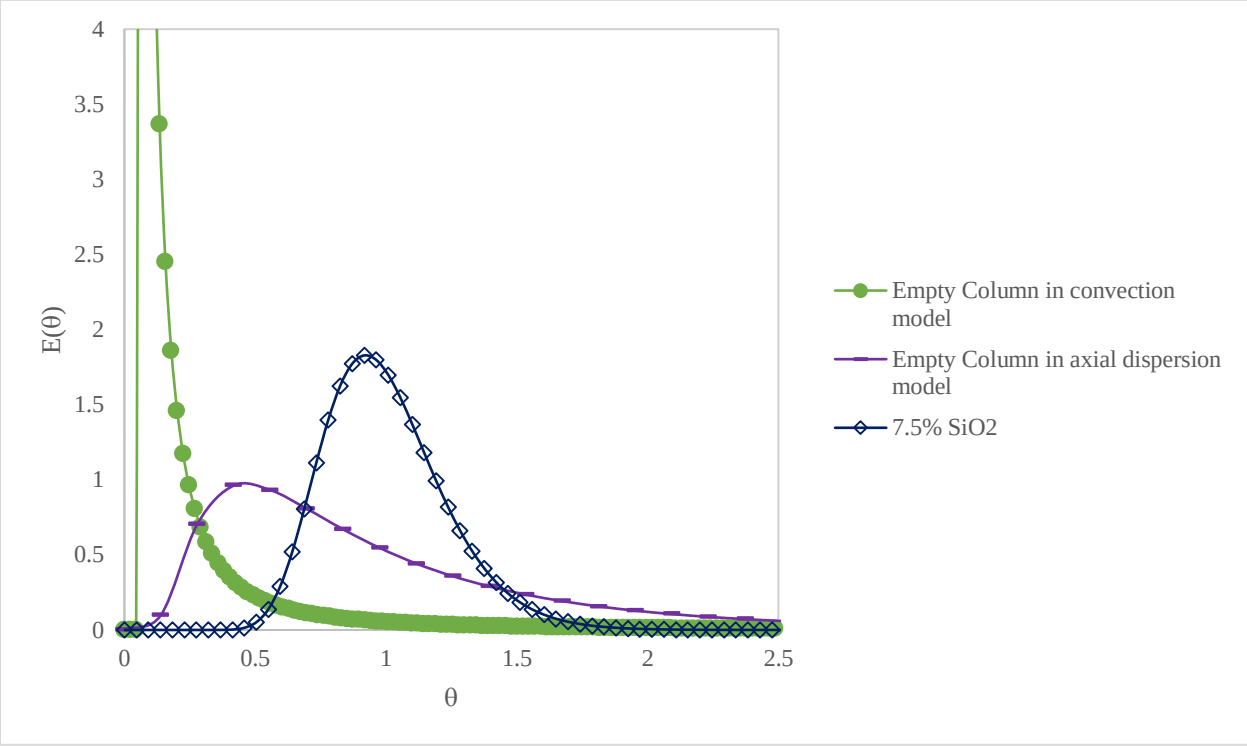

Figure 4–9: Empty Column in convection model and axial dispersion model. Using the "no column" data in the convolution model.

As can be seen from Fig 4-9, the empty column modeled with the axial dispersion model makes the comparison with the curve of other columns easier, therefore, the following comparisons that involve the empty column all use the axial dispersion model.

Fig 4-10 shows the E(θ) function of columns reinforced by a higher amount of SiO_2. The empty column is still the one with the greatest dispersion. Column with 7.5% SiO_2 again shows the lowest amount of dispersion at this higher binder content comparison. When the binder content increases from 7.5% to 10%, 15% and 20%, the curves move back to the left and become closer to that of an empty column. The dispersion in the column increases and it deviates more from plug flow.

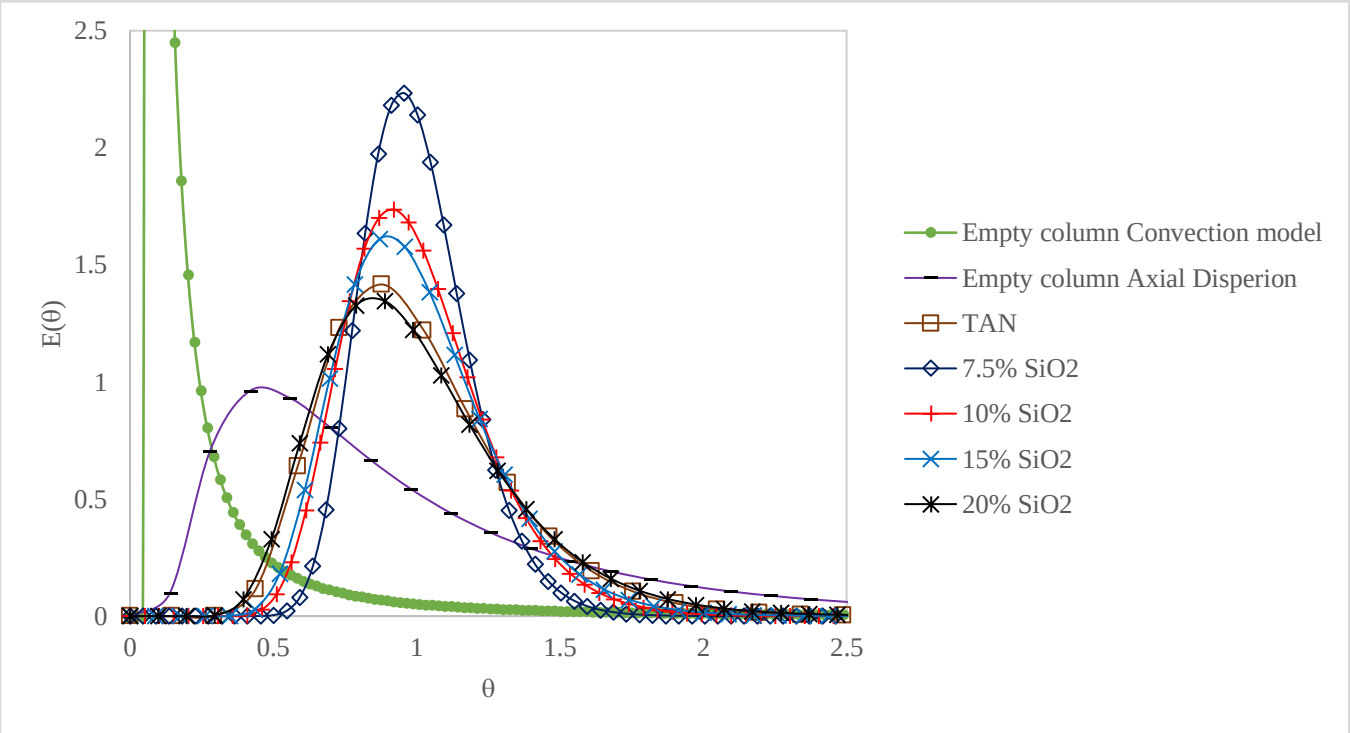

Figure 4–10: E(θ) function of columns reinforced by a higher amount of SiO_2. Using the "no column" data in the convolution model.

To determine the optimized SiO_2 content for the packing materials in the column, an overview of all E(θ) results is presented in Fig 4-11. As the binder content becomes higher, the flow pattern shifts closer to plug flow and the dispersion decreases. It reaches the smallest amount of dispersion at 7.5% SiO_2 with the most tendency to plug flow. Then the distribution function moves back to the left and deviates more from plug flow with the increase of binder. The amount of axial dispersion becomes larger when the binder increases from 7.5% to 20%. Overall, column packed with particles reinforced by 7.5% SiO_2 shows the smallest dispersion and the most tendency to plug flow. Therefore, it is concluded that a SiO_2 content of 7.5% is optimal.

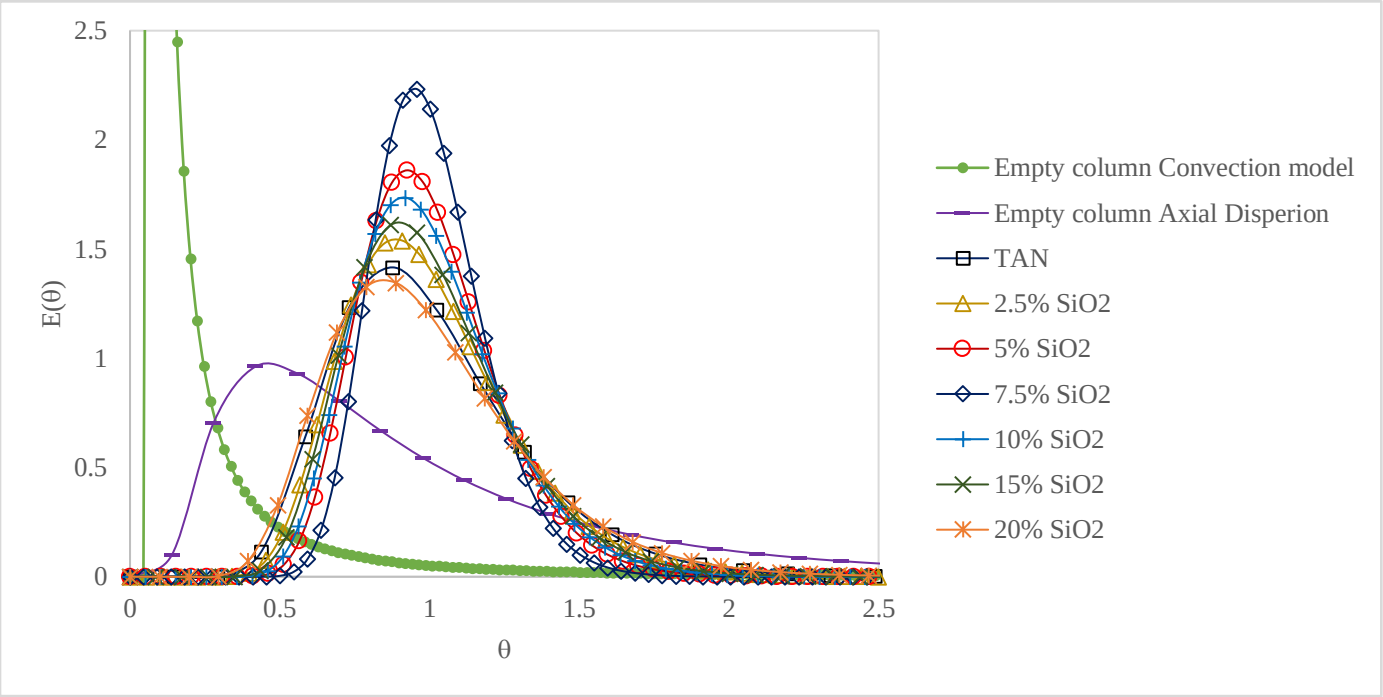

Figure 4–11: E(θ) function of all columns reinforced by SiO_2. Using the "no column" data in the convolution model.

4.3.2 Columns with $AlH_6O_{12}P_3$

Columns packed with 5% to 20% $AlH_6O_{12}P_3$ were processed and the distribution function was obtained in Fig 4-12. No regularity can be observed from the results. With the increase in binder, the function shifts to the left when $AlH_6O_{12}P_3$ content moves up from 0 to 5%; then moves to the right when $AlH_6O_{12}P_3$ is increased to 10%; and again shifts to the left when binder content rises to 15% and 20%.

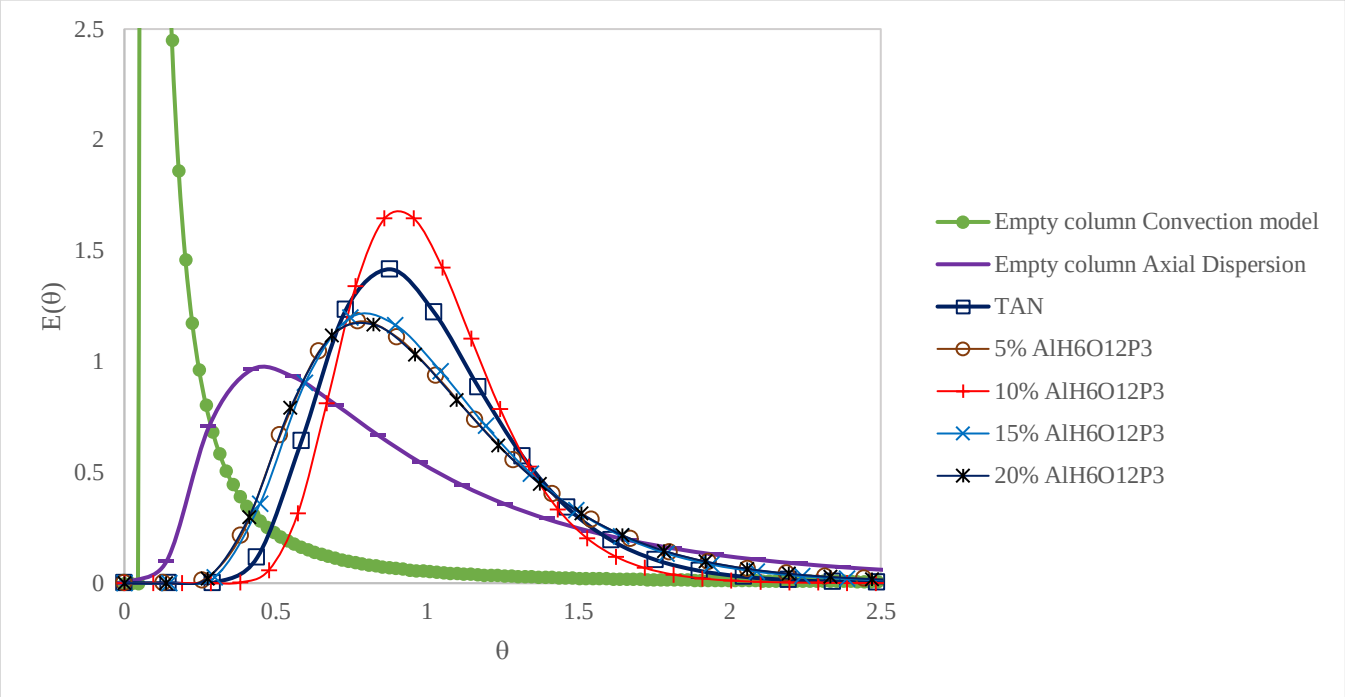

Figure 4–12: E(θ) function of all columns reinforced by $AlH_6O_{12}P_3$. Using the "no column" data in the convolution model.

The change in the binder $AlH_6O_{12}P_3$ does not bring obvious change in the distribution function and the amount of axial dispersion, because $AlH_6O_{12}P_3$ is not very effective in binding and strengthening the structure of TAN. The system is still fragile and has difficulty resisting the flow even applied with 15% or 20% binder, thus the flow pattern in these columns do not deviate too much from the one in the column of unreinforced TAN, and no improvement can be obtained with the addition of this binder.

In summary, the binder SiO_2 is more effective in binding TAN compared to $AlH_6O_{12}P_3$. The axial dispersion in the packed column is minimized when applied with 7.5% SiO_2 to TAN. The flow behavior with $AlH_6O_{12}P_3$ is still very similar to the column with TAN for all concentrations. No obvious advantage was observed when $AlH_6O_{12}P_3$ was used as a binding material.

4.4 Peclet number

All columns were run 3 times under the same experimental condition and Pe and t_m were calculated for each run using the axial dispersion model Eq 14. Pe gives information on the diffusion in the packed column and t_m indicates how much time the dye spends in the column. The flow pattern can be characterized by these 2 parameters. The values of Pe and t_m and their relation to the binder content are presented in the next sections.

4.4.1 Columns with SiO_2

Pe and t_m of the columns packed with TAN reinforced by SiO_2 were determined from the axial dispersion equation and plotted in Fig. 4-13.

The Pe follow the same pattern with increasing binder content and reaches a peak of Pe at 7.5%, then decreases when content increases. A larger value of Pe means the amount of advection is greater and the diffusion is smaller, which indicates a smaller axial dispersion. This corresponds to the results of the distribution function, as E(θ) of columns with 0 to 7.5% SiO_2 moves closer to plug flow when SiO_2 content rises and deviates away from plug flow when SiO_2 increases from 7.5% to 20%. E(θ) function shows particles with 7.5% SiO_2 have the smallest amount of axial dispersion. The Pe also proves that 7.5% SiO_2 has the largest advection. Generally, the relation of Pe and binder content conforms to the results of the distribution function E(θ).

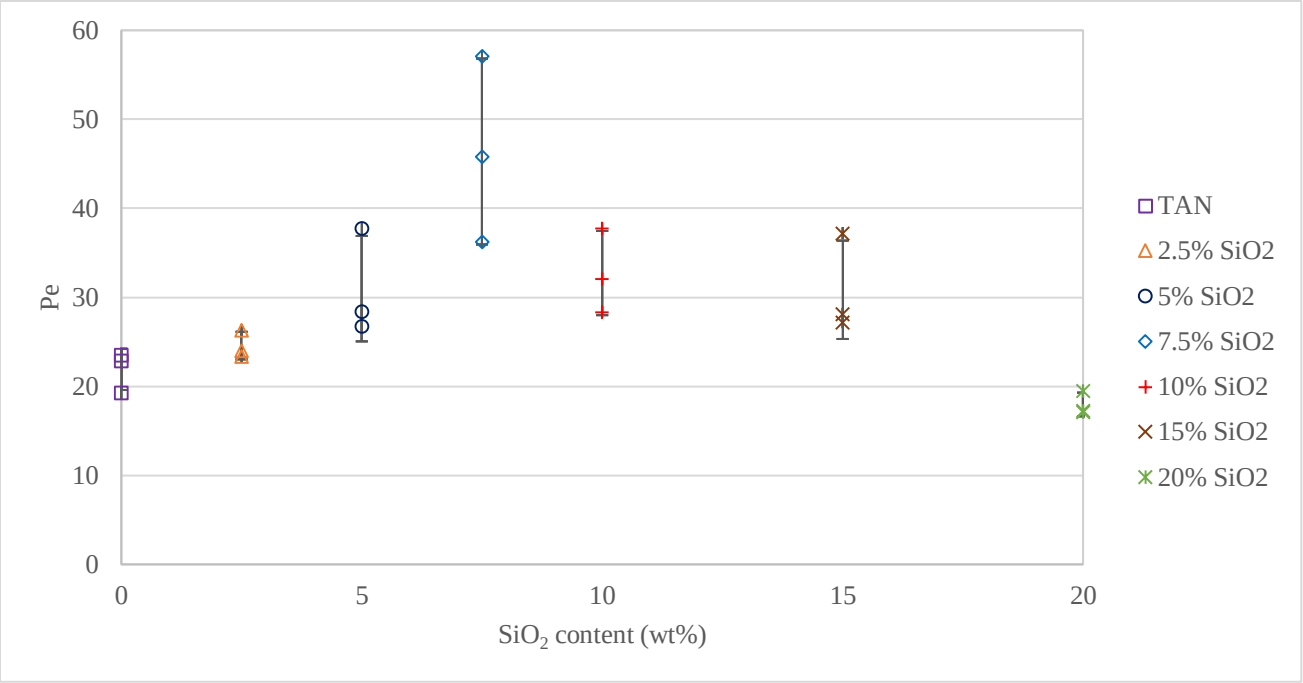

Figure 4–13: The relation of SiO_2 content and Pe. Using the "no column" data in the convolution model.

The relation of mean residence time t_m and SiO_2 content also conforms to the results of the experimental RTD and the normalized $E(\theta)$ applied with the axial dispersion model. In Fig 4-14 it can be observed that generally the values of t_m also follow the pattern of increasing until the content of SiO_2 rises to 7.5% and then decreasing. From 0 to 7.5%, the addition of binder strengthens the particles and stabilize the micro-sized paths among them, enabling the fluid to spend more time through these numerous paths. When it gets to the critical point (7.5%) where the binder is just enough for the particles, adding more binder causes the particles to aggregate and destroys the macro-sized pores inside the aggregates which decreases the time for the fluid to spend in the packing materials because the fluid tends to travel through the void volume between the particle aggregates. Thus, the mean residence time t_m decreases when SiO_2 increases from 7.5% to 20%.

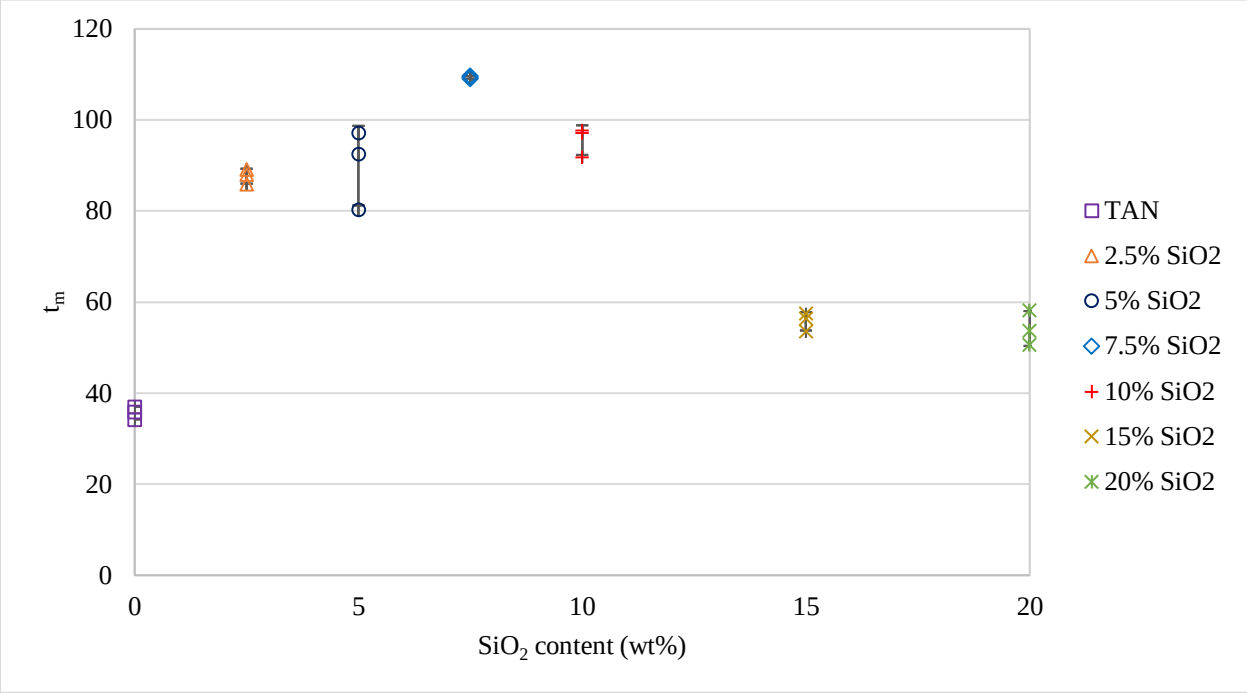

Figure 4–14: The relation of SiO_2 content and t_m. Using the "no column" data in the convolution model.

4.4.2 Columns with $AlH_6O_{12}P_3$

The plot of Pe and $AlH_6O_{12}P_3$ contents is in Fig 4-15. The results do not show a pattern, as Pe fluctuates with the increase in $AlH_6O_{12}P_3$ content. It is difficult to draw a conclusion indicating which one of them shows the best result. The flow-through properties of the packing materials are not changed too much even though 0 to 20% binder is applied on the structure. Therefore, it is concluded that the binder $AlH_6O_{12}P_3$ did not effectively bind the TAN nanosheets.

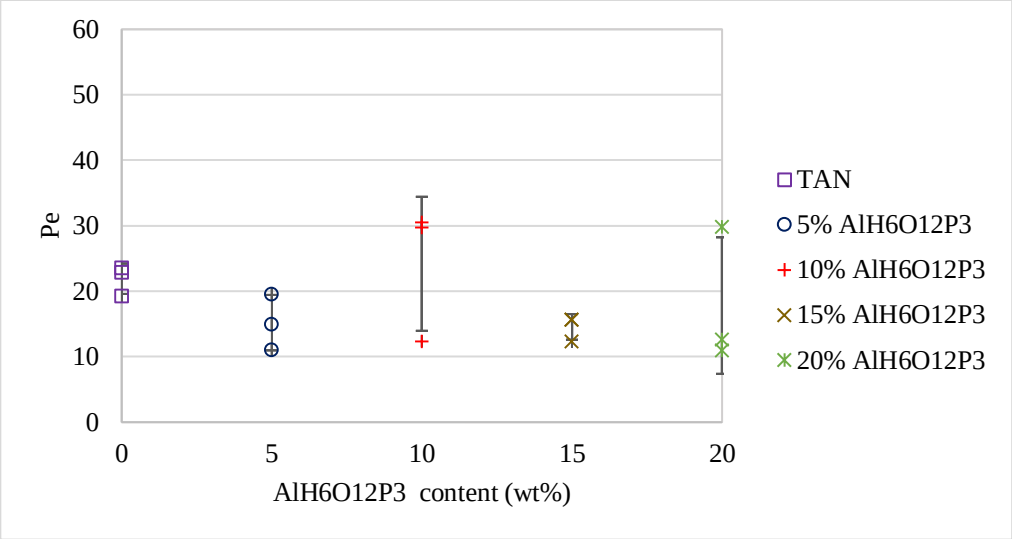

Figure 4–15: The relation of $AlH_6O_{12}P_3$ content and Pe. Using the "no column" data in the convolution model.

Fig 4-16 shows the relation of $AlH_6O_{12}P_3$ content and t_m. Like the values of Pe, t_m still does not show any pattern. It is assumed that the structure and the morphology of these packing materials with different binder contents are basically the same.

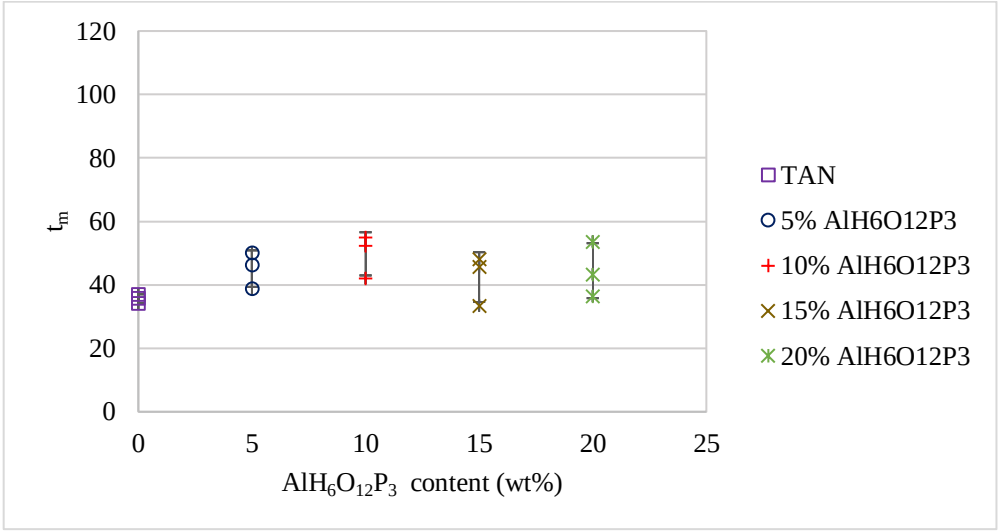

Figure 4–16: The relation of $AlH_6O_{12}P_3$ content and t_m. Using the "no column" data in the convolution model.

In summary, the binder SiO_2 shows better binding performance than $AlH_6O_{12}P_3$. The flow in the packing materials reinforced by SiO_2 also presents higher Pe than those with $AlH_6O_{12}P_3$, which indicates columns packed with SiO_2-reinforced TAN have less back mixing or axial dispersion and more tendency to ideal plug flow. A much larger t_m also proves that the flow spends more time in travelling through the very fine paths in the packing materials reinforced by SiO_2 and the numerous macro-sized paths lead to a good mixing of the components in the flow at the micro-level, thus improving the mixing performance in the packed column and decreasing the back mixing in axial direction at the micro-level.

4.5 Porosity test

The porosity of the packings was determined and shown in Figure 4-17. The porosity of the particles drop for both SiO_2 and $AlH_6O_{12}P_3$ with increasing binder content. The excess binder fills the pores of the particles resulting in the loss of the original structure. As SiO_2 has a more prominent binding effect, particles reinforced by SiO_2 generally show less porosity loss compared to $AlH_6O_{12}P_3$.

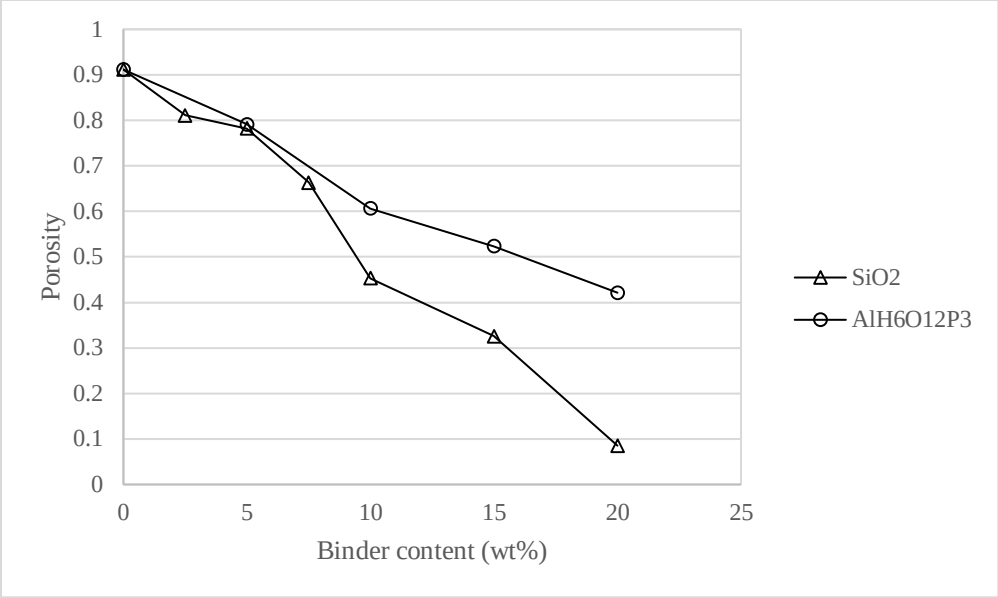

Figure 4–17: The porosity of TAN reinforced by different amount of binder

4.6 SEM characterization of post-experiment particles

SEM images of particles were taken to determine if the 2D/3D structure had resisted the flow test. If the particles were not well reinforced by the binder and still shows weak resistance to forces, they may collapse due to the flow of the fluid compared to those that have been strengthened.

4.6.1 Columns with SiO_2

Fig 4-18 shows SEM images of particles reinforced by SiO_2 after the flow tests. It is clearly that non reinforced TAN structure collapsed due to the flow experiment. The particles of TAN are smaller compared to other particles, as they were cracked due to their low strength. TAN shows

accumulation of particles in the form of aggregates, because they were pressed and aggregated together.

In the images of 2.5, 5, 7.5 and 10%, binder retained the twinned structure, as observed before the flow experiments. No obvious particle cracking or accumulation can be observed. They generally have the same characteristics as those before the flow tests. It indicates that the presence of SiO_2 makes the structure stronger and particles have resistance to flow.
SEM images of 15% and 20% SiO_2 again prove that the binder is excessive as the particles fill in the 2D/3D structure of the TAN.

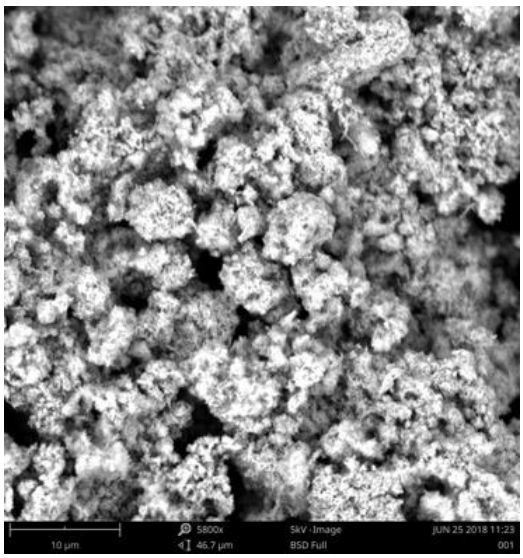

TAN

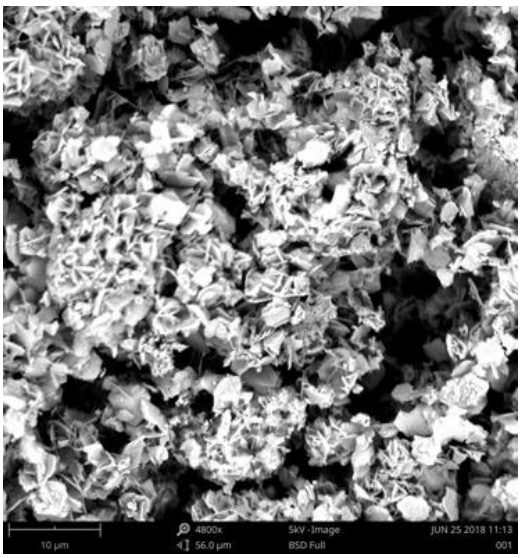

2.5% SiO_2

5% SiO_2

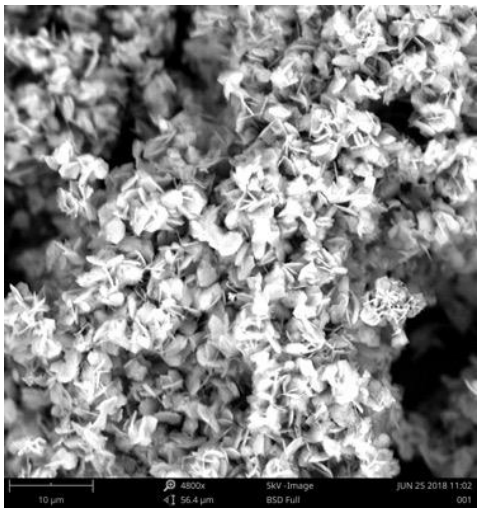

7.5% SiO_2

Figure 4–18: SEM images of particles reinforced by SiO_2 after flow tests

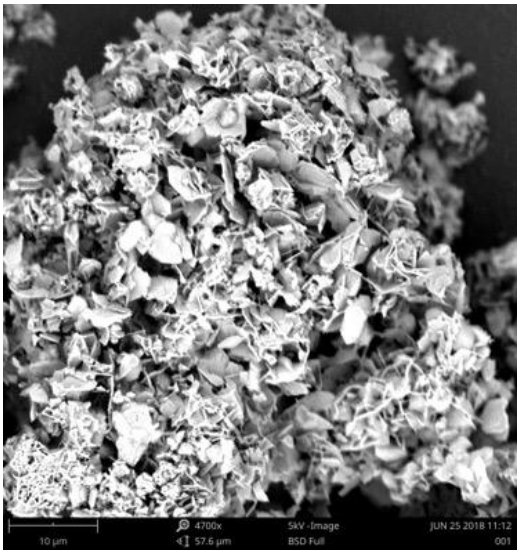

10% SiO_2

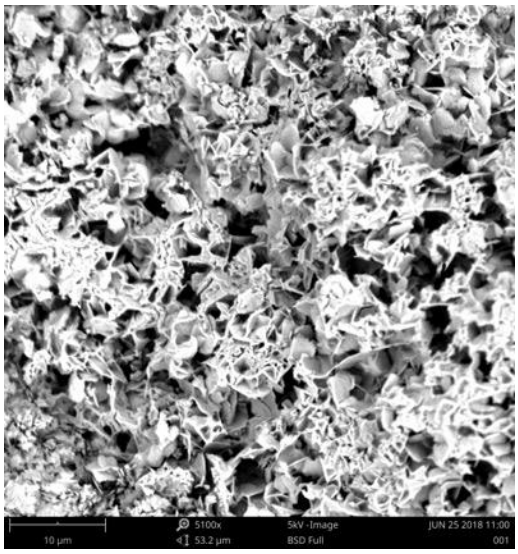

15% SiO_2

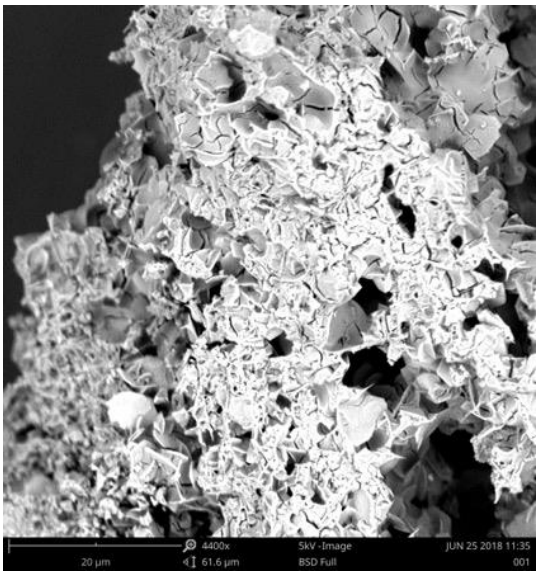

20% SiO_2

Figure 4–18 (continued): SEM images of particles reinforced by SiO_2 after flow tests

4.6.2 Columns with $AlH_6O_{12}P_3$

Fig 4-19 shows the SEM images of particles reinforced by $AlH_6O_{12}P_3$ after the flow tests. The packings all look alike and are highly aggregated with the loss of the 2D/3D structure. This indicates that $AlH_6O_{12}P_3$ did not bind the TAN material leaving it to collapse as TAN without binder would. Also that the $AlH_6O_{12}P_3$ was finer than the TAN nananoplatelets and accumulated as a filter cake in the packing under the flow conditions. The aggregate size of all the samples is nearly the same at 10 μm, which proves that $AlH_6O_{12}P_3$ did not sufficiently reinforce TAN.

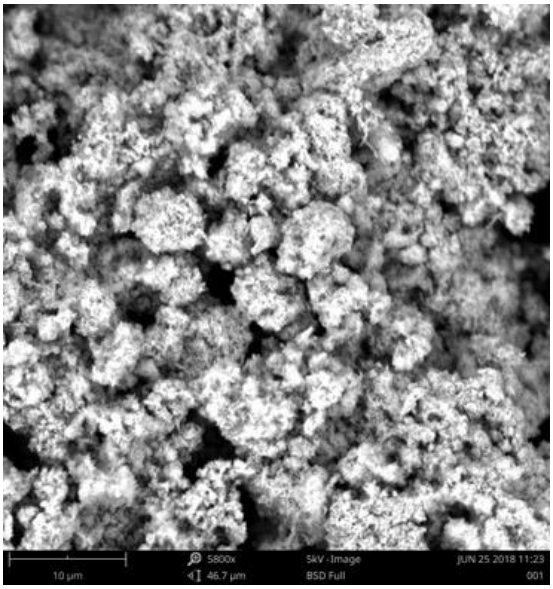

TAN

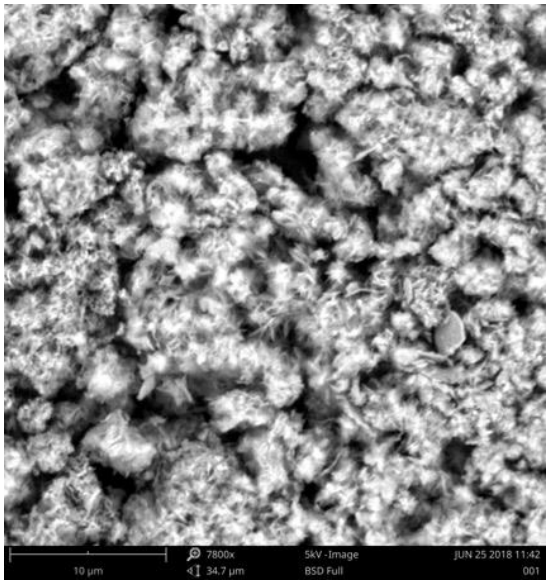

2.5% $AlH_6O_{12}P_3$

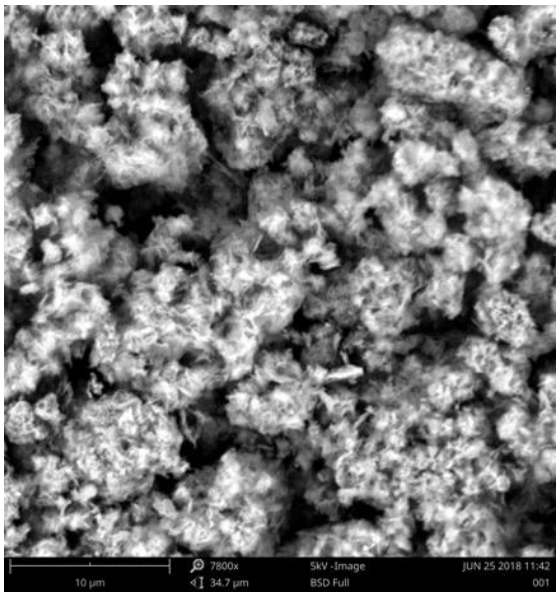

5% $AlH_6O_{12}P_3$

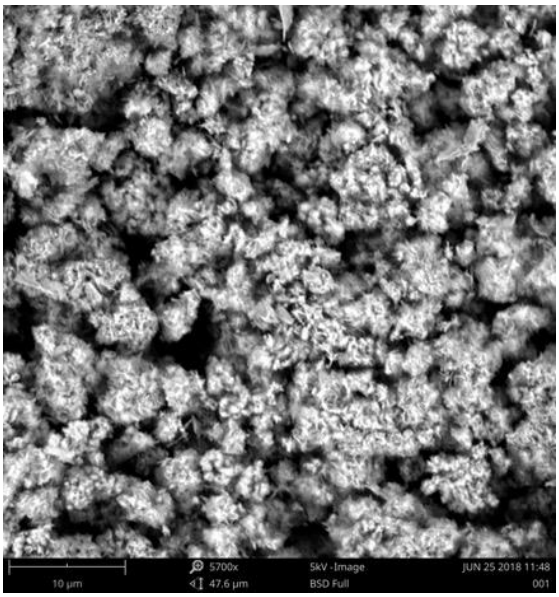

7.5% $AlH_6O_{12}P_3$

Figure 4–19: SEM images of particles reinforced by $AlH_6O_{12}P_3$ after flow tests

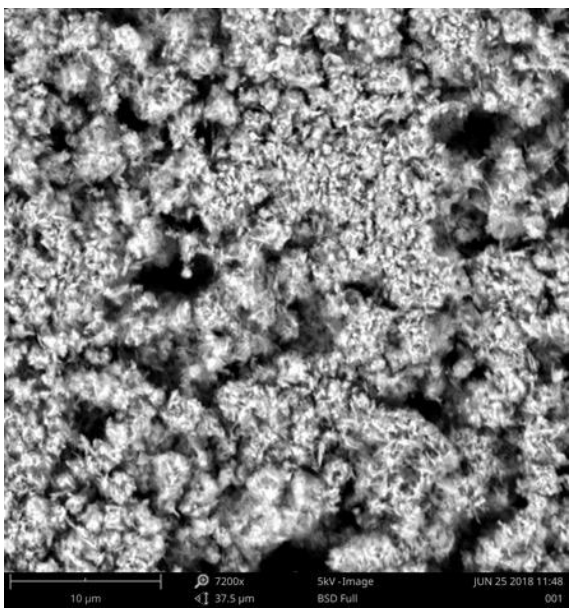

10% $AlH_6O_{12}P_3$

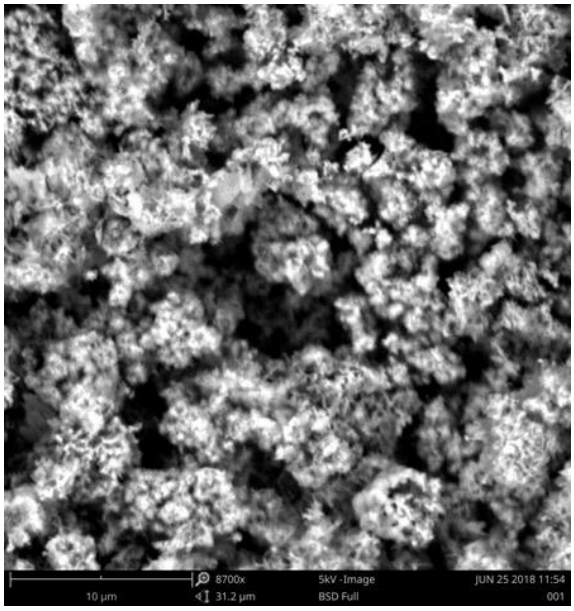

15% $AlH_6O_{12}P_3$

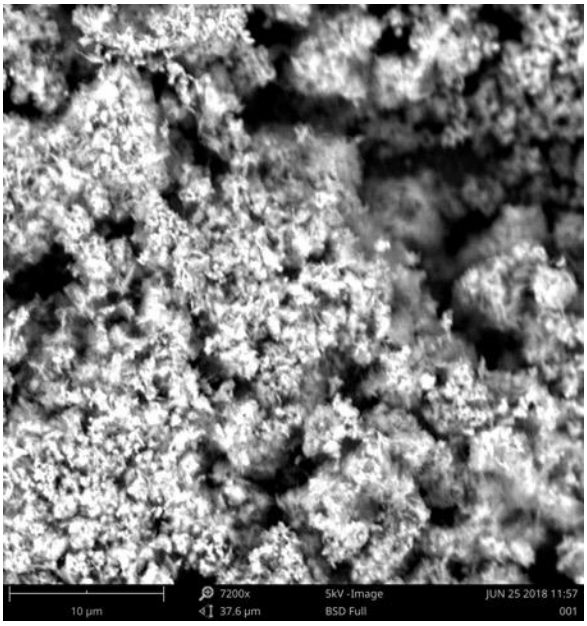

20% $AlH_6O_{12}P_3$

Figure 4–19 (continued): SEM images of particles reinforced by $AlH_6O_{12}P_3$ after flow tests

4.7 Effect of column compaction

The above analysis was based on the absence of a column connecting the injection and detection system. Each column measured 4 cm and was filled with 10 mg of packing. This left a certain length of open tubing in the column. Data for an empty tube measuring 4 cm ("empty column") was also generated in this work. The convolution integral was reinterpreted using the empty column results to represent the RTD data of the system in Figure 4-6. These results for tm and Pe are shown in Table 4-2. The parameters calculated using the no column data was also presented in the same table for comparison.

Table 4–2: Pe and t_m calculated by convolution based on no column and empty column

Column	Packing Length (cm)	dp (μm)	Based on no column			Based on empty column		
			t_m	Pe	Mean Deviation	t_m	Pe	Mean Deviation
TAN	1.9	30	34	19	0.0003	4	39	0.0009
			37	23	0.0004	4	38	0.0007
			36	34	0.0004	4	31	0.0007
TAN+2.5% SiO_2	1.9	30	89	23	0.0001	50	36	0.0002
			86	26	0.0001	47	89	0.0002
			88	24	0.0001	49	44	0.0002
TAN+5% SiO_2	1.9	50	80	28	0.0001	41	648	0.0003
			92	27	0.0001	53	57	0.0002
			97	37	0.0002	59	247	0.0002
TAN+7.5% SiO_2	2.2	60	109	36	0.0002	70	81	0.0002
			110	57	0.0003	71	2329	0.0003
			109	46	0.0002	71	217	0.0003
TAN+10% SiO_2	2.6	80	92	28	0.0001	53	66	0.0002
			102	38	0.0001	63	146	0.0002
			98	32	0.0001	59	79	0.0002
TAN+15% SiO_2	2.6	100	57	27	0.0001	18	4	0.0005
			53	37	0.0001	14	4	0.0005
			56	28	0.0001	17	3	0.0005
TAN+20% SiO_2	2.6	100	58	19	0.0001	20	48	0.0005
			51	17	0.0001	12	5	0.0003
			54	17	0.0001	15	4	0.0004

Table 4-2 (continued): Pe and t_m calculated by convolution based on no column and empty column

Column	Packing Length (cm)	dp (μm)	Based on no column			Based on empty column		
			t_m	Pe	Mean Deviation	t_m	Pe	Mean Deviation
TAN+5% $AlH_6O_{12}P_3$	1.6	30	39	11	0.0001	6	125	0.0004
			50	20	0.0001	12	5	0.0003
			46	15	0.0001	8	5	0.0003
TAN+10% $AlH_6O_{12}P_3$	2.2	50	52	30	0.0001	14	4	0.0005
			55	30	0.0001	16	3	0.0005
			42	12	0.0001	4	28	0.0003
TAN+15% $AlH_6O_{12}P_3$	2.6	80	33	12	0.0001	4	40	0.0008
			48	16	0.0001	10	4	0.0003
			46	16	0.0001	7	5	0.0003
TAN+20% $AlH_6O_{12}P_3$	1.9	80	36	11	0.0001	4	37	0.0005
			43	13	0.0001	4	19	0.0002
			54	30	0.0001	15	4	0.0005

The Pe of most columns reinforced by SiO_2 based on the empty column input to the convolution integral are larger than those calculated based on the no column input, meaning columns modeled in this way show more plug-flow like behavior after removing the effects caused by the void space which acted as an empty tube. The concentration of 7.5wt% SiO_2 gave the highest Pe number in both the empty and no column cases. Some columns made with 15% and 20% SiO_2 and others with $AlH_6O_{12}P_3$ show lower Pe. This is due to fluid bypass, as the concentrations of 15% and 20% SiO_2 generated aggregates of particles which favors channeling. For columns made with $AlH_6O_{12}P_3$, the values still do not present any pattern. However, they basically have a lower Pe, because these packings have larger aggregate particles which led to channeling.

The above table presents values in two different models. The Pe and t_m that can best describe the flow behavior in the column packings is expected to be in between the values of these two cases. A method that would offer a better estimate of the Pe of the packed column would be to fit a convection model, containing tube length as a parameter, to the data obtained for the empty column. The convection model could then be coupled with a dispersion model representing the RTD of the packed length of tubing. The values of tm and Pe could then be determined for the packing material. Unfortunately, this would increase the number of parameters used in modeling the overall RTD output from the system.

5. Conclusions and recommendations

5.1 Conclusions

TAN was successfully synthesized and their unique twinned 2D/3D nanoplatelet structure was observed. The isoporous nature of TAN is very promising for use as a material in packed beds, columns or catalysts supports. However, the structure of TAN is fragile for use in these applications. It must be reinforced with a suitable binding agent that does not appreciably impede fluid flow and reduce the isoporous nature of the TAN.

Silica sol (SiO_2) and aluminum dihydrogen phosphate ($AlH_6O_{12}P_3$) were selected as the binding agents and the bonding was based on the chemical reaction between the main component in TAN and the binder. To achieve a uniform and homogenous binding, the binder was mixed with ethanol into solution. The optimal ethanol content is found to be 10% for both $AlH_6O_{12}P_3$ and SiO_2.

Particles reinforced using different amounts of SiO_2 or $AlH_6O_{12}P_3$ were packed in columns with the same original packing length (4 cm) for further study and analysis. Eleven columns were packed for testing. The pressure drop in these 11 columns was measured to determine the stability of the TAN packing under flow conditions. Results show that the pressure vs flow curves were all linear for SiO_2 content above 5 wt% and not linear for the $AlH_6O_{12}P_3$ binder. Thus, the SiO_2 binder had a positive effect in strengthening the TAN nanoplatelets.

Tracer injection was then carried out to precisely determine the optimal binder and binder content. Columns reinforced by SiO_2 had a better performance compared to $AlH_6O_{12}P_3$. Increasing the SiO_2 content increased the Pe number; when the SiO_2 content increased to 7.5%, the amount of axial dispersion was minimal and the tendency to plug flow was the largest. However, when SiO_2 content continued to increase from 7.5% to 20%, a totally inverse result occurred where the amount of axial dispersion increased and the tendency towards plug flow decreased. This was due to the influence of the SiO_2 on the TAN. At first, the network of particles increased in strength with the addition of SiO_2 and numerous paths among the twinned particles provide more sites for the components in the fluid to contact and mix, enabling better mixing at the micro-level and thus the back mixing (axial dispersion) observed becomes smaller at the micro-level. The flow pattern tends towards plug flow. The performance reaches the peak when there is just enough SiO_2 (7.5%) in the system. When the SiO_2 content continues to increase, the binder is in excess which changes the unique twinned structure and destroys the macro-sized paths. The TAN then loses the ability to mix at the micro-level and the flow pattern deviates from plug flow. The Peclet number and the mean residence time t_m both validate the above explanation. The binder $AlH_6O_{12}P_3$ does not bring any substantial binding effect and fails in showing a flow behavior that is closer to plug flow compared to SiO_2.

SiO_2 is a better binder to strengthen 2D/3D TAN nanoplatelets. A level of 7.5% SiO_2 is optimal for the best results. Flow in the column packed with 7.5% SiO_2-reinforced TAN shows plug flow like behavior and is a promising material for packed beds, catalysis supports and columns.

The 2D/3D nanoplatelets produced in this work can bring many benefits in applications, such as to enhance the separation efficiency of chromatography columns, reduce band broadening, enable better mixing in packed bed reactors and when used as catalyst supports achieve a higher reactor productivity.

5.2 Recommendations

Based on the results of this work, the following recommendations are proposed for future work.

- The synthesis of TAN should be further investigated to improve its productivity. Currently, only 0.5g TAN can be produced in each batch. This would expand the possible uses of the nanomaterial.
- Two inorganic binders (SiO_2 and $AlH_6O_{12}P_3$) were selected to strengthen the structure of TAN in this work. The potential of other binding agents can also be studied for their performance in binding.
- Other packing methods could be studied to see if they further improve the distribution of particles in the packed column.
- The supports could be functionalized and used as catalysts. Packed columns of reinforced TAN should be investigated in performing chemical reactions.
- Separation of analytes should be tested in the columns and compared to existing HPLC and gel permeation chromatography (GPC) packings.

6. References

[1]. Krunal Shah (2016, Dec 8). Types of packing materials. Retrieved from http://www.chemalone.com/types-of-packing-materials/.

[2]. Meisen Li, Yoshiyuki Bando, Takanori Tsuge, Keiji Yasuda, Masaaki Nakamura. Analysis of liquid distribution in non-uniformly packed trickle bed with single phase flow. Chemical Engineering Science 56 (2001) 5969–5976.

[3]. Debjyoti Ray and Ch. Subrahmanyam. CO2 decomposition in a packed DBD plasma reactor: influence of packing materials. The Royal Society of Chemistry, 2016, 6, 39492–39499.

[4]. A. S. Bodke, S. S. Bharadwaj, and L. D. Schmidt (1998). The Effect of Ceramic Supports on Partial Oxidation of Hydrocarbons over Noble Metal Coated Monoliths. JOURNAL OF CATALYSIS 179, 138–149.

[5]. Matteo Maestri, Alessandra Beretta, Gianpiero Groppi, Enrico Tronconi, Pio Forzatti (2005). Comparison among structured and packed-bed reactors for the catalytic partial oxidation of CH_4 at short contact times. Catalysis Today 105 (2005) 709–717.

[6]. Ronald M. Heck, Suresh Gulati, Robert J. Farrauto (2001). The application of monoliths for gas phase catalytic reactions. Chemical Engineering Journal 82 (2001) 149–15.

[7]. Samira Bagheri, Nurhidayatullaili Muhd Julkapli, and Sharifah Bee Abd Hamid (2014). Titanium Dioxide as a Catalyst Support in Heterogeneous Catalysis. The Scientific World Journal, Volume 2014.

[8]. Yecheng Li, Lei Zhang, Zhuofeng Hu and Jimmy C. Yu (2015). Synthesis of 3D structured graphene as a high performance catalyst support for methanol electro-oxidation. Nanoscale, 2015, 7, 10896–10902.

[9]. Saeid Baroutian, Mohamed K. Aroua, Abdul Aziz A. Raman, Nik M.N. Sulaiman (2011). A packed bed membrane reactor for production of biodiesel using activated carbon supported catalyst. Bioresource Technology 102 (2011) 1095–1102.

[10]. Kang Cheng, Mirella Virginie, Vitaly V. Ordomsky, Catherine Cordier, Petr A. Chernavskii, Mikhail I. Ivantsov, Sébastien Paul, Ye Wang, Andrei Y. Khodakov (2015). Pore size effects in high-temperature Fischer–Tropsch synthesis over supported iron catalysts. Journal of Catalysis 328 (2015) 139–150.

[11]. Jing Xu, Abdul-Rauf Ibrahim, Xiaohui Hu, Yanzhen Hong, Yuzhong Su, Hongtao Wang, Jun Li (2016). Preparation of large pore volume g-alumina and its performance as catalyst support in phenol hydroxylation. Microporous and Mesoporous Materials 231 (2016) 1-8.

[12]. Justo Lobato, HectorZamora, Jorge Plaza, and Manuel A. Rodrigo (2016). Composite Titanium Silicon Carbide as a Promising Catalyst Support for High-Temperature Proton-Exchange Membrane Fuel Cell Electrodes. ChemCatChem 2016, 8, 848-854.

[13]. Abhishek Mishra, Ajay K. Sharma, Sumit Sharma, Rashmi Bagai, Anshu S. Mathur, Ravi P. Gupta, Deepak K. Tuli (2016). Lignocellulosic ethanol production employing immobilized Saccharomyces cerevisiae in packed bed reactor. Renewable Energy, 57-63.

[14]. A. S. Piskun, J. E. de Haan, E. Wilbers, H. H. van de Bovenkamp, Z. Tang, and H. J. Heeres (2016). Hydrogenation of Levulinic Acid to γ-Valerolactone in Water Using Millimeter Sized Supported Ru Catalysts in a Packed Bed Reactor, 2939−2950.

[15]. T. Butterworth, R. Elder, R. Allen (2016). Effects of particle size on CO2 reduction and discharge characteristics in a packed bed plasma reactor. Chemical Engineering Journal 293 (2016) 55–67.

[16]. Jenson Ngoh, Eldin Wee Chuan Lim. Effects of particle size and bubbling behavior on heat transfer in gas fluidized beds. Applied Thermal Engineering 105 (2016) 225–242.

[17]. Noor Al-Rifai, Federico Galvanin, Moataz Morad, Enhong Cao, Stefano Cattaneo, Meenakshisundaram Sankar, Vivek Dua, Graham Hutchings, Asterios Gavriilidi. Hydrodynamic effects on three phase micro-packed bed reactor performance – Gold–palladium catalysed benzyl alcohol oxidation. Chemical Engineering Science 149 (2016) 129–142.

[18]. Ali Faridkhou, Faïcal Larachi. Two-phase flow hydrodynamic study in micro-packed beds – Effect of bed geometry and particle size. Chemical Engineering and Processing 78 (2014) 27–36.

[19]. Ashutosh Mishra, Brahma Dutt Tripathi, Ashwani Kumar Rai (2016). Packed-bed column biosorption of chromium(VI) and nickel(II) onto Fenton modified Hydrilla verticillata dried biomass. Ecotoxicology and Environmental Safety. 420 – 428.

[20]. Eric Lesellier, Caroline West (2015). The many faces of packed column supercritical fluid chromatography – A critical review. Journal of Chromatography A, 2 – 46.

[21]. Nobuo Tanaka, David V. McCalley. Core−Shell, Ultrasmall Particles, Monoliths, and Other Support Materials in High-Performance Liquid Chromatography. American Chemical Society, 2016, 88, 279−298.

[22]. LCGC Editors (2012, Oct 1). Developments in HPLC/UHPLC Column Technology. Retrieved from http://www.chromatographyonline.com.

[23]. J.H. Sun, F.Y. Guan, X.F. Zhu, Z.W. Ning, T.J. Ma, J.H. Liu, T. Deng (2016). Micro-fabricated packed gas chromatography column based on laser etching technology. Journal of Chromatography A, 311 – 316.

[24]. James W. Treadway, Kevin D. Wyndham, James W. Jorgenson (2015). Highly Efficient Capillary Columns Packed with Superficially Porous Particles via Sequential Column Packing. Journal of Chromatography A.

[25]. Martina Catani, Omar H. Ismail, Alberto Cavazzini, Alessia Ciogli, Claudio Villani, Luisa Pasti, Caterina Bergantin, Deirdre Cabooter, Gert Desmet, Francesco Gasparrini, David S. Bell (2016). Rationale behind the optimum efficiency of columns packed with new 1.9 m fully porous particles of narrow particle size distribution. Journal of Chromatography A, 1454 (2016) 78–85.

[26]. Víctor González-Ruiz, Ana I. Olives, M. Antonia Martín. Core-shell particles lead the way to renewing high-performance liquid chromatography. Trends in Analytical Chemistry 64 (2015) 17–28.

[27]. D. Cabooter, A. Fanigliulo, G. Bellazzi, B. Allieri, A. Rottigni, G. Desmet. Relationship between the particle size distribution of commercial fully porous and superficially porous high-performance liquid chromatography column packings and their chromatographic performance. Journal of Chromatography A, 1217 (2010) 7074–7081.

[28]. Alexandre Grand-Guillaume Perrenoud, Jean-Luc Veuthey, Davy Guillarme. Comparison of ultra-high performance supercritical fluid chromatography and ultra-high performance liquid chromatography for the analysis of pharmaceutical compounds. Journal of Chromatography A, 1266 (2012) 158–167.

[29]. Pankaj Aggarwal, H. Dennis Tolley, Milton L. Lee. Monolithic bed structure for capillary liquid chromatography. Journal of Chromatography A, 1219 (2012) 1–14.

[30]. Earl A. Ebach and Robert R. White, 1958. Mixing of Fluids Flowing Through Beds of Packed Solids. A.1.Ch.E. Journal, Vol. 4, No. 2, Page 161.

[31]. J. J. Carberry and R. H. Bretton, 1958. Axial Dispersion of Mass in Flow Through Fixed Beds. A.1.Ch.E. Journal, Vol. 4, No. 3, Page 367.

[32]. J. R. F. Guedes de Carvalho and J. M. P. Q. Delgado, 2003. Effect of Fluid Properties on Dispersion in Flow through Packed Beds. AIChE Journal, Vol. 49, No. 8.

[33]. J. M. P. Q. Delgado, 2006. A critical review of dispersion in packed beds. Heat Mass Transfer, 42: 279–310.

[34]. Han NW, Bhakta J, Carbonell RG (1985) Longitudinal and lateral dispersion in packed beds: effect of column length and particle size distribution. AIChE J 31:277–288.

[35]. J. A. Moulijn and W. P. M. Van Swaaij (1976). The correlation of axial dispersion data for beds of small particles. Chemical Engineering Science, 1976, Vol 31, Page 845-847.

[36]. Grand View Research. (2016). High Purity Alumina Market Analysis By Product And Segment Forecasts To 2024.

[37]. Yongfeng Li, J. S. (2017). Preparation and characterization of super-microporous alumina with crystalline structure. Microporous and Mesoporous Materials, 9-15.

[38]. Chun-Hong Chen, S. I. (2005). Homogenous alumina tube with controlled pore morphology. Materials Science and Engineering, 167 – 173.

[39]. Yunfei Changa, J. W. (2017). Molten salt synthesis of morphology controlled α-alumina platelets. Ceramics International, 12684 – 12688.

[40]. Mickael Lillo, D. L. (2009). Pore opening detection for controlled dissolution of barrier oxide layer and fabrication of nanoporous alumina with through-hole morphology. Journal of Membrane Science, 11 – 17.

[41]. Garces, W. L. (2010). Hydrothermal synthesis of novel alpha alumina nano-materials with controlled morphologies and high thermal stabilities. CrystEngComm, 2996 – 3002.

[42]. Wen Qian Jiao, M. B.-Y. (2012). Synthesis of morphology-controlled mesoporous transition aluminas derived from the decomposition of alumina hydrates. Microporous and Mesoporous Materials, 167 – 177.

[43]. E. Ruckenstein and M. L. Malhotra (1976). Splitting of Platinum Crystallites Supported on Thin, Nonporous Alumina Films. JOUENAL OF CATALYSIS 41, 303-311.

[44]. A. A. Yukhimchuk, A. S. Khapov, I. P. Maksimkin, V. V. Baluev, I. E. Boitsov, A. V. Vertey, S. K. Grishechkin, V. G. Kiselev, I. L. Malkov, R. K. Musyaev, V. V. Popov & D. T.

Sitdikov (2015). Application of Nonporous Alumina Based Ceramics as Structural Material for Devices Handling Tritium at Elevated Temperatures. FUSION SCIENCE AND TECHNOLOGY, VOL. 67.

[45]. Ashraf M. Amin, Eric Croiset, Crystle Constantinou, William Epling (2012). Methane cracking using Ni supported on porous and non-porous alumina catalysts. international journal of hydrogen energy 37 (2012) 9038-9048.

[46]. Jeanne L. Swecker, Abhaya K. Datye (1990). Alcohol Dehydration over Model Nonporous Alumina Powder. JOURNAL OF CATALYSIS 121, 196—201.

[47]. Hideki Masuda and Fumio Hasegwa (1997). Self-Ordering of Cell Arrangement of Anodic Porous Alumina Formed in Sulfuric Acid Solution. The Electrochemical Society, Vol. 144, No. 5.

[48]. Adelaida Perea-Cachero, Pablo Calvo, Enrique Romero, Carlos Téllez and Joaquín Coronas (2017). Enhancement of Growth of MOF MIL-68(Al) Thin Films on Porous Alumina Tubes Using Different Linking Agents. Eur. J. Inorg. Chem. 2017, 2532–2540.

[49]. So-Jin Ahn, Atsushi Takagaki, Takashi Sugawara, Ryuji Kikuchi, S. Ted Oyama (2017). Permeation properties of silica-zirconia composite membranes supported on porous alumina substrates. Journal of Membrane Science, 526 (2017) 409–416.

[50]. Erdem (2017). Sol-gel applications for ceramic membrane preparation. American Institute of Physics.

[51]. Amin, S. K. (2016). An Overview of Production and Development of Ceramic Membranes . International Journal of Applied Engineering Research, 7708-7721.

[52]. Hideki Masuda and Fumio Hasegwa (1996). Fabrication of Gold Nanodot Array Using Anodic Porous Alumina as an Evaporation Mask. Jpn. J. Appl. Phys. Vol. 35, Page 126-129.

[53]. Adelaida Perea-Cachero, Pablo Calvo, Enrique Romero, Carlos Téllez and Joaquín Coronas (2017). Enhancement of Growth of MOF MIL-68(Al) Thin Films on Porous Alumina Tubes Using Different Linking Agents. Eur. J. Inorg. Chem. 2017, 2532–2540.

[54]. Abbas Sadeghzadeh Attar and Zahra Hassani (2015). Fabrication and Growth Mechanism of Single-crystalline Rutile TiO2 Nanowires by Liquid-phase Deposition Process in a Porous Alumina Template. Journal of Materials Science & Technology 31 (2015) 828-833.

[55]. A. Banerjee, R. Bala Chandran, J.H. Davidson (2015). Experimental investigation of a reticulated porous alumina heat exchanger for high temperature gas heat recovery. Applied Thermal Engineering 75 (2015) 889-895.

[56]. Chang-Jiu Li, Jiao Zou, Hui-Bin Huo, Jian-Tao Yao, and Guan-Jun Yang (2015). Microstructure and Properties of Porous Abradable Alumina Coatings Flame-Sprayed with Semi-molten Particles. Journal of Thermal Spray Technology, Volume 25(1-2).

[57]. Linbo Qin, Jun Han, Weiyi Chen, Xi Yao, Shimizu Tadaaki, Heejoon Kim (2016). Enhanced combustion efficiency and reduced pollutant emission in a fluidized bed combustor by using porous alumina bed materials. Applied Thermal Engineering 94 (2016) 813–818.

[58]. Chiara Toccafondi, Sanjay Thorat, Rosanna La Rocca, Alice Scarpellini, Marco Salerno, Silvia Dante, Gobind Das (2014). Multifunctional substrates of thin porous alumina for cell biosensors. J Mater Sci: Mater Med (2014) 25:2411–2420.

[59]. Katrina Roebuck, A.Y. Tremblay (2016), The self-assembly of twinned boehmite nanosheets into porous 3D structures in ethanol–water mixtures. Colloids and Surfaces A: Physicochemical and Engineering Aspects, 238-247.

[60]. Katrina Roebuck, André Y. Tremblay. Optimal aggregate size distribution for the formation of highly efficient nanosheet dynamic membranes. Journal of Membrane Science 514(2016)143–154.

[61]. Fei Wang, J. L.-H.-H. (2017). Surface modification of alumina membranes via a sol-gel process for antifouling properties. Materials Letter, 200 – 202.

[62]. A. I. Ivanets, V. E. (2017). Ceramic Microfiltration Membranes Based on Natural Silica. Petroleum Chemistry, 117 – 126.

[63]. Haitao Geng, X. J. (2016). Fabricationandcompressivepropertiesofclosed-cellalumina ceramicsbybindinghollowaluminaspheres withhigh-temperature binder. CeramicsInternational, 16071 – 16076.

[64]. Syed Zaighum Abbas Bukhari, J.-H. H.-H. (2017). Fabrication and optimization of a clay-bonded SiC flat tubular membrane support for microfiltration applications. Ceramics International, 7736 – 7742.

[65]. S. V. Zaitsev, V. A. (2017). STUDY OF ARTIFICIAL CERAMIC BINDER PROPERTIES IN THE SYSTEM Al2O3 – SiO2 – SiC. Refractories and Industrial Ceramics, 32 – 36.

[66]. Lei Yuana, B. M. (2017). Preparation and properties of mullite-bonded porous fibrous mullite ceramics by an epoxy resin gel-casting process. Ceramics International, 5478 – 5483.

[67]. Sujoy Bose, C. D. (2014). Role of Binder and Preparation Pressure in Tubular Ceramic Membrane Processing: Design and Optimization Study Using Response Surface Methodology (RSM). Ind. Eng. Chem. Res, 12319−12329.

[68]. Nandini Das, H. S. (1998). Formatation of pore structure in tape-cast alumina membranes ± effects of binder content and ®ring temperature. Journal of Membrane Science, 205 ± 212.

[69]. Christine K. Lambert, R. D. (1999). Effect of binder addition on the properties of unsupported g-Al O membranes. Materials Letters, 145 – 149.

[70]. Mihaela Vlasea, Y. S. (2013). A combined additive manufacturing and micro-syringe deposition technique for realization of bio-ceramic structures with micro-scale channels. Adv Manuf Technol, 2261 – 2269.

[71]. Akihiro SHIMAMURA, ,. M.-i. (2017). Fabrication and characterization of porous alumina with a surface layer composed of alumina platelet by direct-foaming method. The Ceramic Society of Japan, 375-377.

[72]. Sarkar, S. (2014). Process for Preparation of Low Cost Clay-Alumina Multichannel Ceramic Membrane for Liquid Filtration Application. Trans. Ind. Ceram. Soc, 239-244.

[73]. Sandeep Sarkar, S. B. (2012). New clay – alumina porous capillary supports for filtration application. Journal of Membrane Science, 130-136.

[74]. Dilek Duman, H. G. (2012). Synthesis, microstructure, and mechanical properties of WC – TiC – Co ceramic composites. Journal of the European Ceramic Society, 1427 – 1433.

[75]. Ding Chen, H. G. (2017). Enhancement of bonding network for silica sol bonded SiC castables by reactive micropowder. Ceramics International.

[76]. J. A. FERNANDO, D. D. (2001). Improving an alumina fiber filter membrane for hot gas filtration using an acid phosphate binder. JOURNAL OF MATERIALS SCIENCE, 5079 – 5085.

[77]. JENG-MAW CHIOU, D. D. (1993). Improvement of the temperature resistance of aluminium-matrix composites using an acid phosphate binder . JOURNAL OF MATERIALS SCIENCE , 1447-1470 .

[78]. J. D. BIRCHALL, N. M. (1987). Effect of chemical bonding at low temperature on the mechanical properties of an unsintered SiC compact . JOURNAL OF MATERIALS SCIENCE LETTERS , 1456-1458.

[79]. Cetin Toy, O. J. (1989). Phosphate Bonding with Several Calcined Aluminas . Ceramics hlternational, 167-171 .

[80]. A. I. Ivanets, V. E. (2017). Ceramic Microfiltration Membranes Based on Natural Silica. Petroleum Chemistry, 117 – 126.

[81]. Manali Ray, P. B. (2015). Preparation and characterization of macroporous pure alumina capillary membrane using boehmite as binder for filtration application. Porous Mater, 1043 – 1052.

[82]. CHEMICAL PROCESSES IN KAOLIN SINTERED WITH NaH2PO4. (2003). Journal of Thermal Analysis and Calorimetry, 667 – 672.

[83]. Babak Koohestani, Tikou Belem, Ahmed Koubaa, Bruno Bussière (2016). Experimental investigation into the compressive strength development of cemented paste backfill containing Nano-silica. Cement and Concrete Composites, 180-189.

[84]. Guozhu Liu, J. G. (2014). Effects of Colloidal Silica Binder on Catalytic Activity and Adhesion of HZSM-5 Coatings for Structured Reactors. Chinese Journal of Chemical Engineering, 875 – 881.

[85]. Xiaoxia Hu, L. Y. (2016). Freeze casting of composite system with stable fiber network and movable particles. Journal of the European Ceramic Society, 4147 – 4153.

[86]. R. Yu, P. Spiesz, H.J.H. Brouwers (2014). Effect of nano-silica on the hydration and microstructure development of Ultra-High Performance Concrete (UHPC) with a low binder amount. Construction and Building Materials, 140–150.

[87]. Jingjing Sun, Zijun Hu, Junning Li, Hongbo Zhang, ChenCheng Sun (2014). Thermal and mechanical properties of fibrous zirconia ceramics with ultra-high porosity. Ceramics International, 11787–11793.

[88]. Yijie Gao, Fernando J. Muzzio, Marianthi G. Ierapetritou (2012). A review of the Residence Time Distribution (RTD) applications in solid unit operations. Powder Technology, 416 – 423.

[89]. Danckwerts, P.V., 1953. Continuous flow systems: distribution of residence times. Chem. Eng. Sci.1 – 13.

[90]. R. B. MacMullin and M. Weber (1935), Jr.,Trans. Am. Inst. Chem. Eng.,31, 409.

[91]. Fogler_ECRE_CDROM.book (2008). 867-945.

[92]. G. Michael Shook, Shannon L. Ansley, Allan Wylie (2004). Tracers and Tracer Testing: Design, Implementation, and Interpretation Methods.

[93]. Ricky Bonnera, Lara Aylward, Uwe Kappelmeyer, Craig Sheridana (2017). A comparison of three different residence time distribution modellingmethodologies for horizontal subsurface flow constructed wetlands. Ecological Engineering, 99 – 113.

[94]. Francisco J. Valdes-Parada, J. Alberto Ochoa-Tapia, Jose Alvarez-Ramirez. Validity of the permeability Carman–Kozeny equation: A volume averaging approach. Physica A 388 (2009) 789–798.

[95]. Torez Kasnavia, De Vu, David A Sabatini (1998). Fluorescent Dye and Media Properties Affecting Sorption and Tracer Selection. Ground Water, Vol.37, No.3.

[96]. Carola G.C.C. Gutierrez, Eduardo F.T.S. Dias, Jorge A.W. Gut (2010), Residence time distribution in holding tubes using generalized convection model and numerical convolution for non-ideal tracer detection. Journal of Food Engineering, 248–256.

7. Appendix

7.1 Transforming the raw data to obtain the RTD function

The calculation and the processing steps of RTD function for the column with 2.5% SiO_2 are presented as an example. All other columns were processed using the same method.

Fig 7-1 was the plot of the original data (voltage) versus time which was recorded by the spectrometer when the column was connected in the test system.

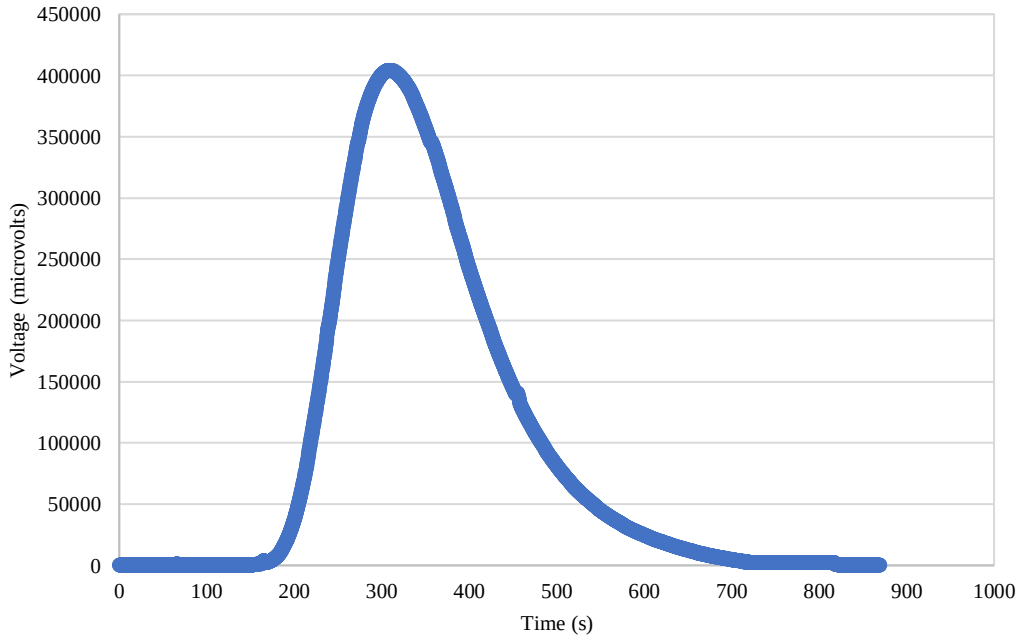

Figure 7–1: The original data (microvolts) versus time

By using Eq 13, $Concentration = exp\left(\frac{\ln\frac{Voltage}{236714}}{0.6267}\right)$, which is the correlation of voltage and concentration, the plot of voltage versus time can be interpreted into concentration versus time.

In this equation, x is concentration and y is voltage. The concentration curve (C curve) was calculated and shown in Fig 7-2.

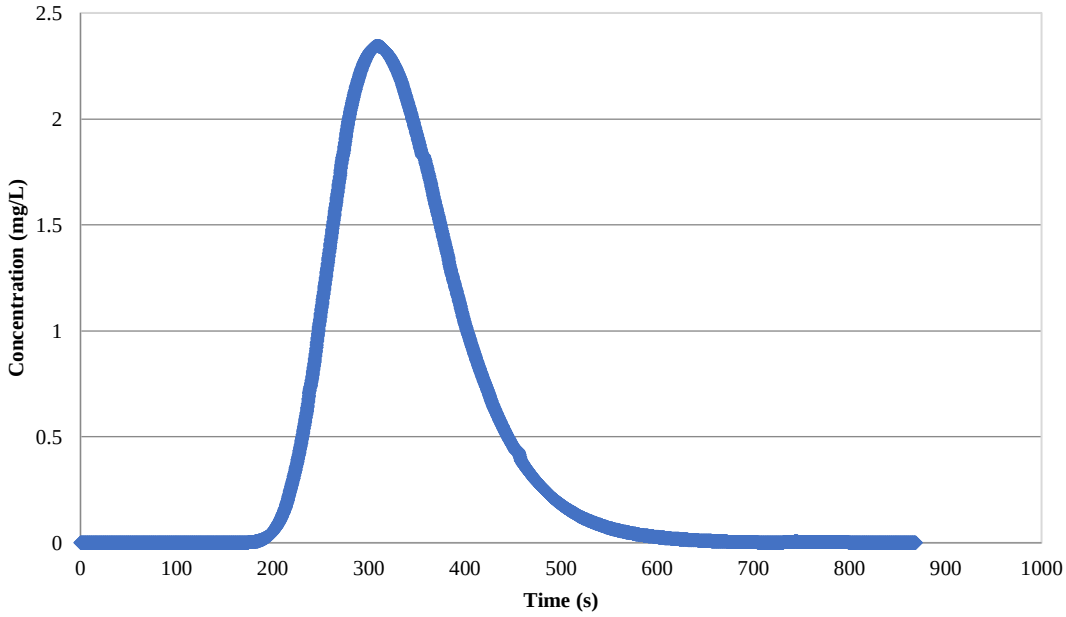

Figure 7–2: The concentration curve (C curve) of the raw data

With the concentration curve, the RTD function E(t) can be established simply by using Eq 3:

$$E(t) = \frac{C(t)}{\int_0^\infty C(t)dt}$$

The area under the concentration curve needs to be calculated and then all data points of concentration are divided by the area. As the original concentration curve has about 4800 data points that are too many for an illustration example, thus only some data points were selected here to present the calculation. Table 7-1 presents a few data points from the original concentration curve.

Table 7–1: data points of the original concentration curve

t (s)	0	0.2	…	202.8	203	203.2	…	802.2	802.4	…
C (mg/L)	0	0	…	0.069	0.071	0.073	…	0.001	0	…

To calculate the area under the curve, the trapezoidal rule was applied for approximating the definite integral:

$$\int_0^{\infty} C(t)dt = \int_0^{0.2} C(t)dt + \cdots + \int_{202.8}^{203} C(t)dt + \int_{203}^{203.2} C(t)dt + \cdots + \int_{802.2}^{802.4} C(t)dt + \cdots$$

$$= \frac{1}{2}(0+0) \times (0.2-0) + \cdots + \frac{1}{2}(0.069+0.071) \times (203-202.8) + \frac{1}{2}(0.071+0.073)$$

$$\times (203.2-203) + \cdots + \frac{1}{2}(0.001+0) \times (802.4-802.2) + \cdots$$

$$= 352.86 \text{ mg·s/L}$$

The total area under the concentration curve $\int_0^{\infty} C(t)dt$ was 352.86 mg·s/L. 4800 data points were recorded in every 0.2 seconds originally so the trapezoidal rule can be applied to process all data points and lead to an accurate result.

Now the E(t) function can be calculated

$$E(t) = \frac{C(t)}{352.86 \text{ mg} \cdot \text{s/L}}$$

with the following results:

Table 7–2: C(t) and E(t)

t (s)	0	0.2	…	202.8	203	203.2	…	802.2	802.4	…
C(t) (mg/L)	0	0	…	0.069	0.071	0.073	…	0.001	0	…
E (t) (s^{-1})	0	0	…	1.9×10^{-4}	2.0×10^{-4}	2.0×10^{-4}	…	2.8×10^{-6}	0	…

The data of time and E(t) function is plotted in Fig 7-3.

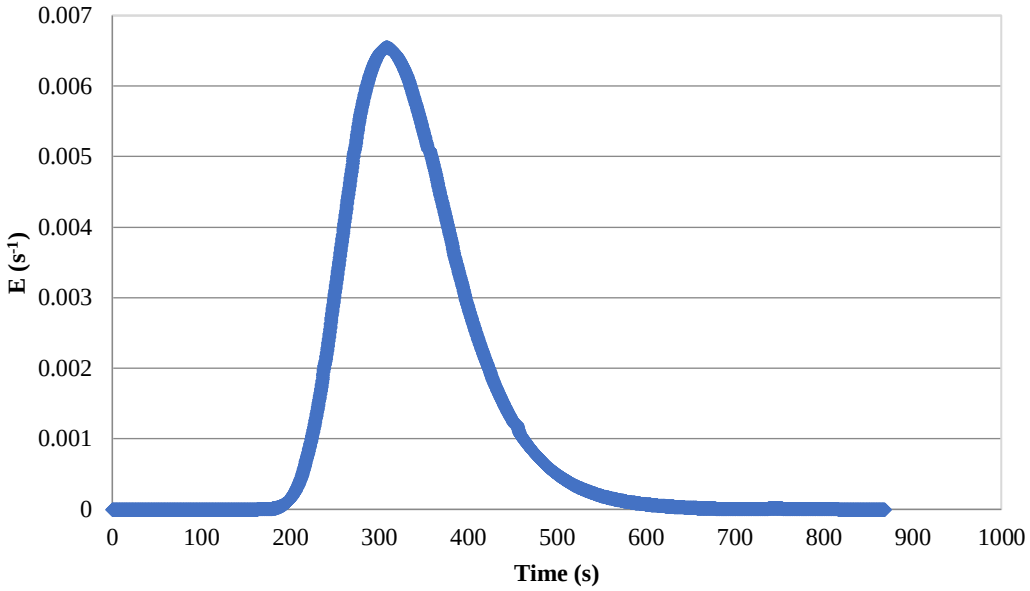

Figure 7–3: E(t) function

The above sample calculation presents the method of transforming the original data to concentration curve and then to the RTD function. All columns tested were processed in the same method based on the raw data points.

E(θ) is also commonly used as it is a dimensionless function that enables reactors with different sizes to be compared with each other. The calculation of E(θ) is shown in Eq 10:

$$E(\theta) = t_m E(t)$$

The only unknown is t_m, the mean residence time. The calculation of t_m is based on Eq 7:

$$t_m = \int_0^\infty tE(t)dt$$

t·E(t) is calculated and shown in Table 7-3.

Table 7–3: Calculating t·E(t)

t (s)	0	0.2	…	202.8	203	203.2	…	802.2	802.4	…
C(t) (mg/L)	0	0	…	0.069	0.071	0.073	…	0.001	0	…
E (t) (s^{-1})	0	0	…	1.9×10^{-4}	2.0×10^{-4}	2.0×10^{-4}	…	2.8×10^{-6}	0	…
t·E(t)	0	0	…	0.039	0.041	0.042	…	0.002	0	…

$\int_0^\infty tE(t)dt$ can be calculated by applying trapezoidal rule in the same way that $\int_0^\infty C(t)dt$ was calculated and thus the plot of E(θ) can be generated.

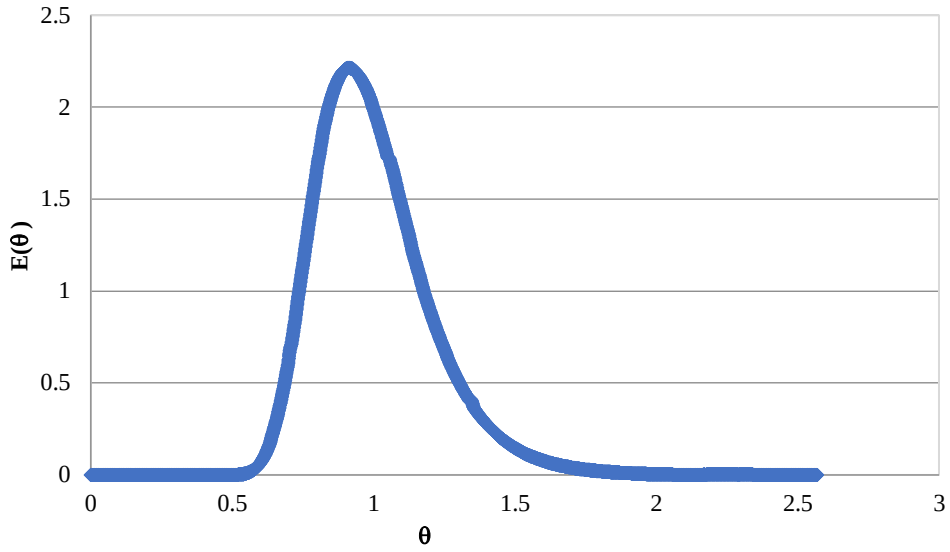

Figure 7–4: E(θ) function.

7.2 Convolution

As the steps described in Fig 4-6, C_{in} and E curve of the column are the two knowns that can lead to C_{out}, which is the convoluted signal of the column that has been removed of the interference caused by the testing system. To obtain the input signal C_{in}, the tracer injection was done without any column connected to the testing system. Fig 7-5 shows the concentration curve obtained by the detector when no column was connected. In order to make the process of the convolution easier and also maintain an acceptable accuracy, data points at every 5 seconds were used for calculation instead of the original 4800 points at 0.2 second intervals.

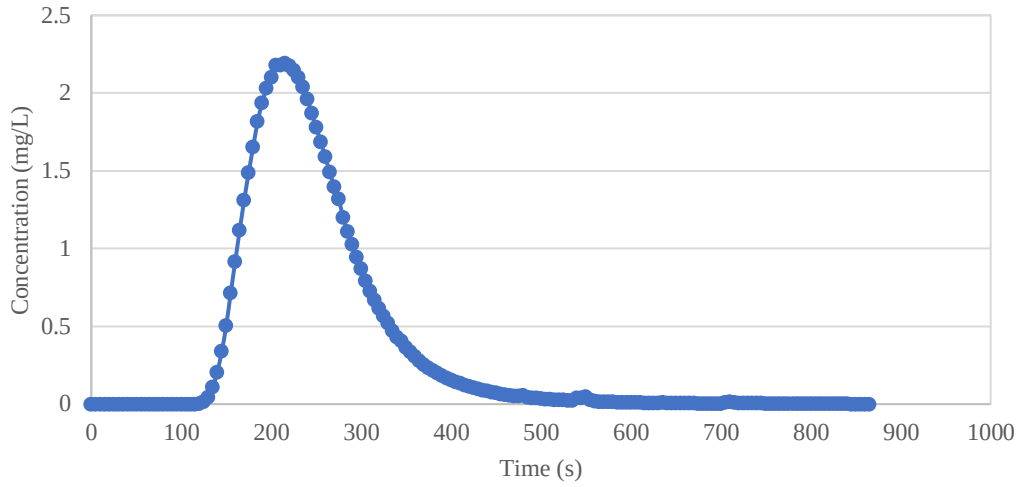

Figure 7–5 : The input signal C_{in} (in every 5 seconds)

With C_{in} in Fig 7-5 and E function of the column in Fig 7-3, the output signal C_{out} was calculated in Excel shown in Fig 7-6. Calculations for every 5 seconds were performed. Data for every 50 seconds are shown in Fig 7-6.

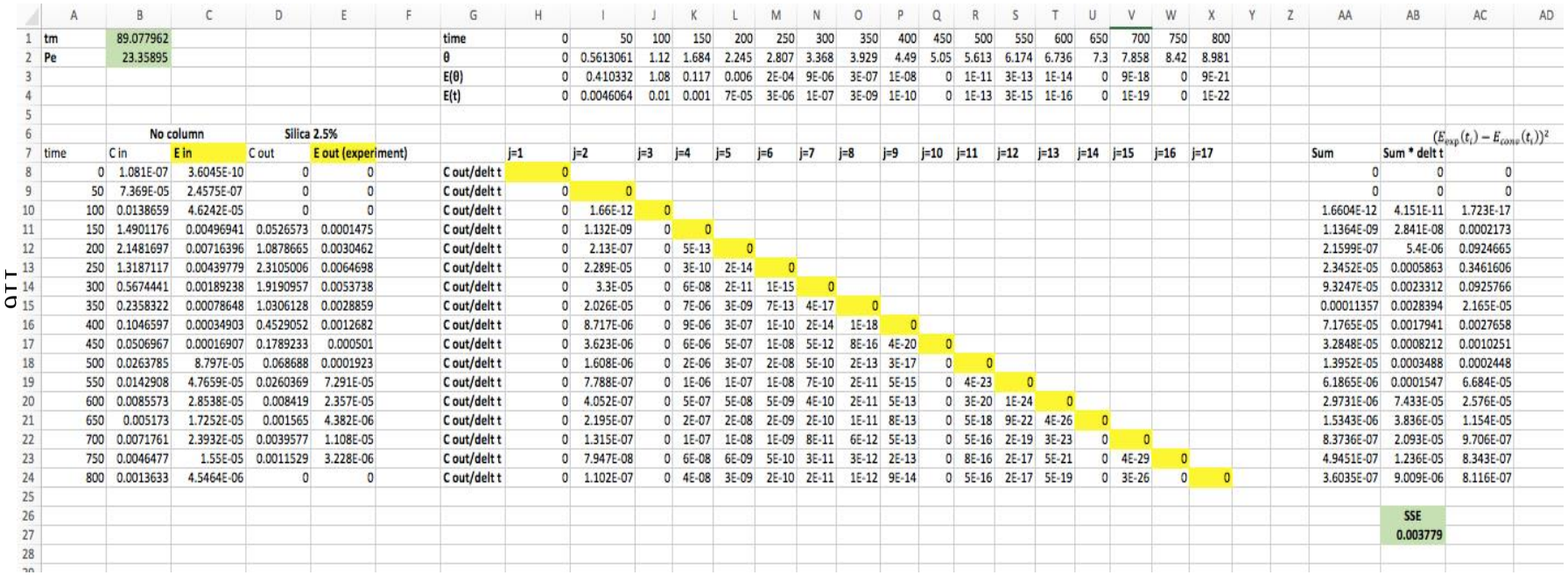

	A	B	C	D	E	F	G	H	I	J	K	L	M	N	O	P	Q	R	S	T	U	V	W	X	Y	Z	AA	AB	AC	AD
1	tm	89.077962					time	0	50	100	150	200	250	300	350	400	450	500	550	600	650	700	750	800						
2	Pe	23.35895					θ	0	0.5613061	1.12	1.684	2.245	2.807	3.368	3.929	4.49	5.05	5.613	6.174	6.736	7.3	7.858	8.42	8.981						
3							E(θ)	0	0.410332	1.08	0.117	0.006	2E-04	9E-06	3E-07	1E-08	0	1E-11	3E-13	1E-14	0	9E-18	0	9E-21						
4							E(t)	0	0.0046064	0.01	0.001	7E-05	3E-06	1E-07	3E-09	1E-10	0	1E-13	3E-15	1E-16	0	1E-19	0	1E-22						
5																														
6		No column		Silica 2.5%																									$(E_{exp}(t_i) - E_{conv}(t_i))^2$	
7	time	C in	E in	C out	E out (experiment)			j=1	j=2	j=3	j=4	j=5	j=6	j=7	j=8	j=9	j=10	j=11	j=12	j=13	j=14	j=15	j=16	j=17			Sum	Sum * delt t		
8	0	1.081E-07	3.6045E-10	0	0		C out/delt t	0																			0	0	0	
9	50	7.369E-05	2.4575E-07	0	0		C out/delt t	0	0																		0	0	0	
10	100	0.0138659	4.6242E-05	0	0		C out/delt t	0	1.66E-12	0																	1.6604E-12	4.151E-11	1.723E-17	
11	150	1.4901176	0.00496941	0.0526573	0.0001475		C out/delt t	0	1.132E-09	0	0																1.1364E-09	2.841E-08	0.0002173	
12	200	2.1481697	0.00716396	1.0878665	0.0030462		C out/delt t	0	2.13E-07	0	5E-13	0															2.1599E-07	5.4E-06	0.0924665	
13	250	1.3187117	0.00439779	2.3105006	0.0064698		C out/delt t	0	2.289E-05	0	3E-10	2E-14	0														2.3452E-05	0.0005863	0.3461606	
14	300	0.5674441	0.00189238	1.9190957	0.0053738		C out/delt t	0	3.3E-05	0	6E-08	2E-11	1E-15	0													9.3247E-05	0.0023312	0.0925766	
15	350	0.2358322	0.00078648	1.0306128	0.0028859		C out/delt t	0	2.026E-05	0	7E-06	3E-09	7E-13	4E-17	0												0.00011357	0.0028394	2.165E-05	
16	400	0.1046597	0.00034903	0.4529052	0.0012682		C out/delt t	0	8.717E-06	0	9E-06	3E-07	1E-10	2E-14	1E-18	0											7.1765E-05	0.0017941	0.0027658	
17	450	0.0506967	0.00016907	0.1789233	0.000501		C out/delt t	0	3.623E-06	0	6E-06	5E-07	1E-08	5E-12	8E-16	4E-20	0										3.2848E-05	0.0008212	0.0010251	
18	500	0.0263785	8.797E-05	0.068688	0.0001923		C out/delt t	0	1.608E-06	0	2E-06	3E-07	2E-08	5E-10	2E-13	3E-17	0	0									1.3952E-05	0.0003488	0.0002448	
19	550	0.0142908	4.7659E-05	0.0260369	7.291E-05		C out/delt t	0	7.788E-07	0	1E-06	1E-07	1E-08	7E-10	2E-11	5E-15	0	4E-23	0								6.1865E-06	0.0001547	6.684E-05	
20	600	0.0085573	2.8538E-05	0.008419	2.357E-05		C out/delt t	0	4.052E-07	0	5E-07	5E-08	5E-09	4E-10	2E-11	5E-13	0	3E-20	1E-24	0							2.9731E-06	7.433E-05	2.576E-05	
21	650	0.005173	1.7252E-05	0.001565	4.382E-06		C out/delt t	0	2.195E-07	0	2E-07	2E-08	2E-09	2E-10	1E-11	8E-13	0	5E-18	9E-22	4E-26	0						1.5343E-06	3.836E-05	1.154E-05	
22	700	0.0071761	2.3932E-05	0.0039577	1.108E-05		C out/delt t	0	1.315E-07	0	1E-07	1E-08	1E-09	8E-11	6E-12	5E-13	0	5E-16	2E-19	3E-23	0	0					8.3736E-07	2.093E-05	9.706E-07	
23	750	0.0046477	1.55E-05	0.0011529	3.228E-06		C out/delt t	0	7.947E-08	0	6E-08	6E-09	5E-10	3E-11	3E-12	2E-13	0	8E-16	2E-17	5E-21	0	4E-29	0				4.9451E-07	1.236E-05	8.343E-07	
24	800	0.0013633	4.5464E-06	0	0		C out/delt t	0	1.102E-07	0	4E-08	3E-09	2E-10	2E-11	1E-12	9E-14	0	5E-16	2E-17	5E-19	0	3E-26	0	0			3.6035E-07	9.009E-06	8.116E-07	
25																														
26																												SSE		
27																												0.003779		
28																														

Figure 7–6: Sample calculation in Excel using the "no column" data in the convolution model.

By minimizing SSE, Excel Solver returns the two values of Pe and t_m, and C_{out} can be obtained in the column AB. E(t) and E(θ) of the axial dispersion model are presented in row No.3 and No.4.

The E(θ) function applied with the model and the convolution method for the column with 2.5% SiO_2 is shown in Fig 7-7.

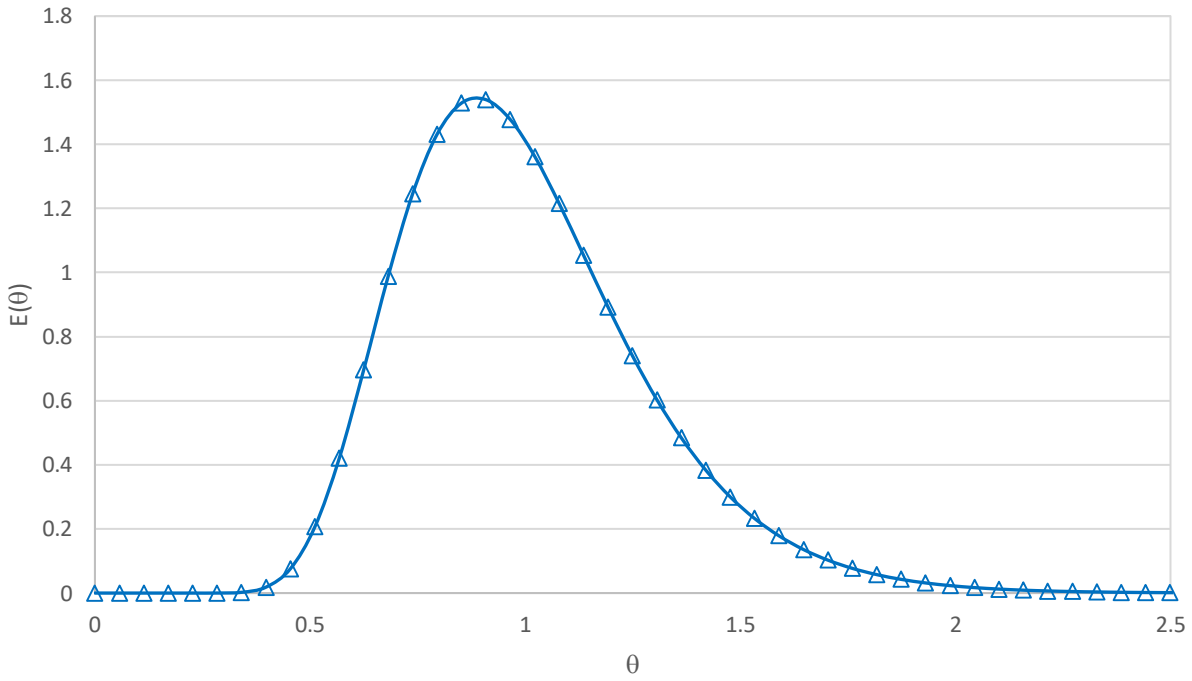

Figure 7–7 : E(θ) of the column with 2.5 wt% SiO_2 using the "no column" data in the convolution model.

All other columns were processed in the same method.